Search for new physics with one Higgs boson in the bb$\gamma\gamma$ channel with the ATLAS detector

Maxime Fernoux

To cite this version:

Maxime Fernoux. Search for new physics with one Higgs boson in the bb$\gamma\gamma$ channel with the ATLAS detector. High Energy Physics - Experiment [hep-ex]. Aix Marseille Université, 2024. English. NNT : 2024AIXM0258 . tel-04798535

HAL Id: tel-04798535
https://theses.hal.science/tel-04798535v1

Submitted on 22 Nov 2024

Aix*Marseille université
Socialement engagée

NNT/NL : 2024AIXM0258/020ED352

THÈSE DE DOCTORAT

Soutenue à Aix-Marseille Université
le 30 septembre 2024 par

Maxime FERNOUX

Search for new physics with one Higgs boson in the $b\bar{b}\gamma\gamma$ channel with the ATLAS detector

Discipline
Physique et Sciences de la Matière

Spécialité
Physique des Particules et Astroparticules

École doctorale
ED 352 Physique et Sciences de la Matière

Laboratoire/Partenaires de recherche
Centre de Physique des Particules de Marseille (CPPM),
Aix-Marseille Université - CNRS/IN2P3

Composition du jury

Anne-Catherine LE BIHAN IPHC, Strasbourg, France	Rapporteure
Tristan DU PREE Nikhef / Université de Twente, Pays-Bas	Rapporteur
Stephane JEZEQUEL LAPP, Annecy, France	Examinateur
Cristinel DIACONU CPPM, Marseille, France	Président du jury
Arnaud DUPERRIN CPPM, Marseille, France	Directeur de thèse
Elisabeth PETIT CPPM, Marseille, France	Co-directrice de thèse

CENTRE DE PHYSIQUE DES PARTICULES DE MARSEILLE
CPPM

Affidavit

I, undersigned, Maxime Fernoux, hereby declare that the work presented in this manuscript is my own work, carried out under the scientific direction of Arnaud Duperrin and Elisabeth Petit, in accordance with the principles of honesty, integrity and responsibility inherent to the research mission. The research work and the writing of this manuscript have been carried out in compliance with both the french national charter for Research Integrity and the Aix-Marseille University charter on the fight against plagiarism.

This work has not been submitted previously either in this country or in another country in the same or in a similar version to any other examination body.

Marseille, July 5, 2024

Liste de publications et participation aux conférences

Liste des publications réalisées dans le cadre du projet de thèse:

1. ATLAS Collaboration, "Search for a resonance decaying into a scalar particle and a Higgs boson in the final state with two bottom quarks and two photons in proton-proton collisions at a center of mass energy of 13 TeV with the ATLAS detector", arXiv: 2404.12915 [hep-ex], submitted 19 April 2024, accepted by JHEP.
2. ATLAS Collaboration, "Neural Network Jet Flavour Tagging with the Upgraded ATLAS Inner Tracker Detector at the High-Luminosity LHC", ATL-PHYS-PUB-2022-047 (2022).

As an ATLAS Collaboration author, the full list of publications that I signed can be found here.

Participation aux conférences et écoles d'été au cours de la période de thèse:

1. IN2P3 School of Statistics 2022, Carry-le-Rouet, May 2022.
2. Journées de Rencontre Jeunes Chercheurs 2023, Saint-Jean-de-Monts, October 2023. "Search for a heavy scalar X decaying to a scalar S and the Higgs boson in the $X \to SH \to b\bar{b}\gamma\gamma$ channel with ATLAS Run 2 data".
   The corresponding proceedings can be found in: JRJC 2023 - Journées de Rencontres Jeunes Chercheurs. Book of Proceedings. URL : hal-04609124v2 (2024).
3. Conférence Higgs Hunting 2024, Orsay and Paris, September 2024. "Search for a resonance decaying into a scalar particle and a Higgs boson in the final state with two bottom quarks and two photons in proton-proton at 13 TeV with the ATLAS detector".

"Tout le malheur des hommes vient d'une seule chose, qui est de ne savoir pas demeurer en repos dans une chambre"
Blaise Pascal, *Pensées*

"Il paraît que les grands peintres ont observé les grands maîtres"
Médine, *Kyll* (ft. Booba)

Abstract

The Standard Model (SM) is the current theory that describes the elementary particles and their interactions. The Higgs boson discovery in 2012 at the Large Hadron Collider (LHC) at CERN marked a remarkable success of its predictive power even if the SM has shortcomings. Since then, the Higgs boson and the Higgs mechanism have been thoroughly studied in the hope to find a hint for new physics. These researches are made possible by high quality experimental infrastructures like the LHC and the ATLAS detector. Its current Inner Detector will be replaced by the brand new Inner Tracker to maintain a high level of tracking and object reconstruction performance in the harsher environment of High-Luminosity LHC (HL-LHC). This thesis presents the adaptation of a neural network based flavour tagging algorithm in the HL-LHC configuration. The track selection used in the training and the resampling method have notably been optimised. A research for new scalar particles in the Higgs sector X and S in the $X \to SH \to b\bar{b}\gamma\gamma$ channel is also presented. The analysis is performed using 140 fb^{-1} of ATLAS Run 2 data at $\sqrt{s} = 13$ TeV. Parameterised Neural Networks (PNNs) are used to probe a large range of masses m_X and m_S. Results show a local (global) excess of 3.55σ (2.0) with respect to the background only hypothesis. 95% CL upper limits between 0.09 and 39 fb are set on the signal production cross section $X \to SH$ in the $b\bar{b}\gamma\gamma$ final state.

Keywords: LHC, ATLAS, Higgs boson, Beyond Standard Model physics, bbyy, Deep Set Neural Network, *b*-tagging, HL-LHC, ITk.

Résumé

Le Modèle Standard est la théorie actuelle décrivant les particules élémentaires et leurs interactions. Sa validité a été renforcée par la découverte du boson de Higgs au grand collisionneur de hadrons du CERN, le LHC, en 2012 bien que l'on sache qu'il est incomplet. Les propriétés du boson et du mécanisme de Higgs sont étudiées en détail au LHC dans l'espoir d'observer des signes de nouvelle physique. Ces recherches sont permises grâce à des moyens expérimentaux comme le LHC et le détecteur ATLAS. Le trajectographe interne d'ATLAS sera entièrement remplacé par un nouveau détecteur appelé ITk dans l'objectif de maintenir de bonnes performances de reconstruction des traces avec la nouvelle configuration plus exigeante du LHC à haute luminosité (HL-LHC). Cette thèse présente l'adaptation d'un algorithme d'étiquetage des jets issus de quarks b basé sur un réseau de neurones à apprentissage profond dans la configuration d'ITk. La sélection de traces utilisées par le réseau de neurones et la méthode de réechantillonage ont notamment été optimisées. Elle présente également une recherche de nouvelle physique via des particules scalaires X et S dans le canal de désintégration $X \to SH \to b\bar{b}\gamma\gamma$ réalisée avec 140 fb^{-1} de données collectés par ATLAS à $\sqrt{s} = 13$ TeV. L'analyse utilise des réseaux de neurones paramétriques pour sonder une vaste région de masses m_X et m_S. Les résultats révèlent un léger excès local de 3.55σ (2.0 global) par rapport à l'hypothèse bruit de fond uniquement. Des limites supérieures sont posées sur la section efficace de production du signal $X \to SH$ dans cet état final et s'étendent entre 0.09 et 39 fb.

Mots-clés : LHC, ATLAS, boson de Higgs, Physique au delà du Modèle Standard, bbyy, Réseau de neurones à apprentissage profond, b-tagging, HL-LHC, ITk.

Acknowledgments / Remerciements

First and foremost I would like to thank my supervisors Elisabeth Petit and Arnaud Duperrin. Working in a CERN experiment and an impressive international collaboration was certainly a dream for the high school student that I was when I first heard of the Higgs boson and I am very grateful that you gave me this opportunity. A few more words are needed for Elisabeth with whom I shared most of the day-to-day work. Your curiosity and scientific rigour are an inspiration and you managed to constantly remind me why we love doing particle physics. I also would like to thank Thomas Strebler for his huge help and guidance during the flavour tagging qualification project and for the amazing opportunity to go to the JRJC.

Next I would like to thank my jury members who took the time to travel all the way to Marseille for the defense. Extra mention to the 'rapporteurs' Tristan Du Pree and Anne-Catherine Le Bihan who went into the tedious task of reading this entire document even though it clearly lacks any literature interest.

I would like to thank my colleagues in the ATLAS Collaboration, especially members of the FTAG group and the *SH* analysis. Special thanks goes to Laura who did an outstanding work and helped me a lot in this analysis.

En passant en français, je veux poursuivre en remerciant toutes les personnes qui ont contribué à cette thèse au CPPM . Merci à l'administration, à Cristinel Diaconu qui a présidé mon jury ainsi qu'aux membres du groupe ATLAS du laboratoire. Merci aux collègues du foot, particulièrement à Pierre et Eric qui seraient sûrement Ballon d'or s'ils étaient aussi assidus au foot qu'aux pots de thèse. Merci aux doctorants, à toi Hichem, à toutes les personnes incroyables qui contribuent à faire du CPPM un endroit épatant et je n'oublie pas les anciennes parties trop tôt Laurie et Floriane.

Enfin (les meilleurs pour la fin), merci à cette exceptionnelle team de thésards, les bien nommés 'Avengers'. Merci à Godefroy pour tes références nerd, ton aide et la passion que tu mets dans tellement de choses. Merci à Luc pour ta curiosité, tes propositions d'activités créatives et pour tes passes au foot. Merci à Tyann pour ton dynamisme, pour les aprems jeux de société et pour être le meilleur chanteur du labo. Garde cette énergie en manif et ailleurs s'il te plaît. Merci à Gaya pour ton enthousiasme et ta bonté. Reste dans l'académie, la recherche a besoin de gens comme toi. Merci à Marie d'être l'adorable personne que tu es derrière ta timidité. Merci pour tous les conseils et avis que j'ai sollicité (même si tu sais que je me fiche de l'avis des autres). Merci à Arthur d'être le premier à vouloir venir en after et d'accepter de jouer aux échecs avec moi malgré mon cerveau de petit singe. Et merci à Jean d'avoir endossé le rôle de coach sportif et surtout pour notre amitié incroyable. Je t'aime mon frère.

Il me faut bien sûr remercier toutes les personnes importantes pour moi depuis longtemps et qui ont contribué d'une manière ou d'une autre à la réussite de cette thèse.

J'ai tout d'abord une pensée particulière pour Marie et Remi et je vous remercie d'avoir été les premiers à me guider dans le monde magique et effrayant de la recherche.

Merci infiniment aux Knispons de Chalon de la team Ecole de l'Est (Clément, Noé, Théo, Matt) ou bien de la team Ecole du Centre (Axel, Tim, Raph) sans oublier Hugo. Un mot particulier pour toi Axel qui m'a montré par l'exemple que faire de la physique des particules était possible quand j'en étais à me demander ce que je faisais en école d'ingé. Et merci à ceux qui sont arrivés un peu plus tard dans ma vie (Alexis, Marceau et Jérémi je parle de vous). Votre amitié indéfectible est une bouffée d'air frais et de rigolade depuis presque 20 ans maintenant.

Je tiens aussi à remercier Émilie, Théo et Héloïse. Je ne vous ai pas vu fréquemment pendant ces 3 ans mais nos amitiés comptent beaucoup pour moi et restent plus fortes que jamais.

Pour terminer, je souhaite remercier mes parents et ma famille. Merci à mes parents d'avoir accepté (et financé) ma poursuite d'études à l'issue de l'école d'ingé et d'avoir toujours su insuffler un esprit de curiosité en moi. Une pensée spéciale et affectueuse pour ma mère qui m'aura soutenu continuellement jusqu'à corriger l'anglais de cette thèse.

Résumé en français

La découverte du boson de Higgs dans les expériences CMS et ATLAS en 2012 a couronné le Modèle Standard de la physique des particules (MS) qui décrit les composants élémentaires de la matière et leurs interactions. Le MS est basé sur les principes de symétrie et d'invariance de jauge qui donnent naissance aux interactions qui sont transmises par des particules, les bosons de jauge. Le mécanisme de Higgs décrit la brisure spontanée de symétrie permettant aux bosons de jauge de l'interaction faible et aux fermions d'acquérir une masse. Enfin, le boson de Higgs est une excitation autour de la valeur fondamentale du champ de Higgs et sa découverte a donc permis de lever le voile sur cette composante cruciale du MS.
Au cours de la dernière décennie, cette particule a été étudiée avec précision dans le but de mesurer ses propriétés, comme ses modes de production et de désintégration ou bien sa masse. Jusqu'à présent, toutes les mesures se sont révélées conformes aux prédictions du Modèle Standard. Cependant, beaucoup de questions demeurent. La forme du potentiel de Higgs peut ainsi être étudiée via l'observation d'une paire de bosons de Higgs (un processus appelé di-Higgs). Une avancée dans ce domaine pourrait aller d'une déviation par rapport aux valeurs prédites par le MS jusqu'à l'observation de nouvelles particules dans le secteur de Higgs (les particules liées au mécanisme de brisure spontanée de symétrie) qui pourrait ainsi être "étendu" c'est-à-dire plus complexe que décrit dans le MS. En ce sens, la physique du boson de Higgs constitue un pan très actif de la recherche de physique au-delà du Modèle Standard et le secteur du Higgs est décrit comme un potentiel portail vers cette nouvelle physique.

Ces développements récents ont été rendus possible par le Grand Collisionneur de Hadrons (LHC d'après l'acronyme anglais) du CERN qui a été mis en service en 2008. Le LHC s'inscrit dans le programme des accélérateurs et détecteurs du CERN qui ont permis des découvertes importantes conduisant à l'établissement du MS comme l'observation des courants neutres de l'interaction faible (1973) ou la découverte des bosons W et Z (1983). Le LHC est un accélérateur qui collisionne principalement des protons à une énergie maximale de 13.6 TeV ce qui fait de lui le collisionneur le plus puissant au monde. Les détecteurs ATLAS et CMS sont notamment installés sur le LHC et étudient la physique du boson de Higgs.
L'amélioration des détecteurs est un point très important pour la physique des hautes énergies qui a permis de grandes avancées scientifiques. Une des façons de maximiser la performance d'un accélérateur de particules est d'augmenter la luminosité, une grandeur qui caractérise le nombre de collisions entre protons par seconde et influence ainsi la quantité totale de données collectées. Celle-ci est cruciale d'un point de vue expérimental

car la production de bosons de Higgs est par exemple relativement rare et il faut une quantité importante de données pour que ces évènements deviennent statistiquement significatifs par rapport au bruit de fond.
Dans ce cadre, le trajectographe interne de ATLAS va être remplacé en vue de la mise en place de la phase du LHC à haute luminosité (HL-LHC) qui devrait débuter en 2029. Le nouveau sous-détecteur nommé Inner Tracker (ITk) sera chargé de reconstruire les traces laissées par les particules dans le détecteur dans un environnement plus exigeant du fait de la plus grande luminosité. L'augmentation de la luminosité va de paire avec une augmentation du nombre de collisions entre protons à chaque croisement de faisceau. Cela entraîne davantage de collisions parasites et de traces en résultant par rapport à la collision d'intérêt de plus haute énergie. Ce phénomène appelé empilement menace les performances de reconstruction et d'identification des particules. Leur maintien, voir leur amélioration, est un enjeu crucial pour la qualité des analyses de physique au HL-LHC.

Cette thèse s'articule en quatre parties principales. Le mécanisme de Higgs et le statut actuel de la physique du boson de Higgs sont présentés dans le Chapitre 1. Le détecteur ATLAS ainsi que les outils utilisés par la suite sont décrits dans le Chapitre 2. Enfin, les deux derniers chapitres sont directement liés à mon travail de thèse : le Chapitre 3 décrit l'entraînement d'un algorithme d'étiquetage de saveur des jets pour le HL-LHC et le Chapitre 4 présente une recherche de nouvelle physique dans le secteur de Higgs via des nouvelles particules scalaires X et S dans le canal de désintégration $X \to S(\to b\bar{b})H(\to \gamma\gamma)$.

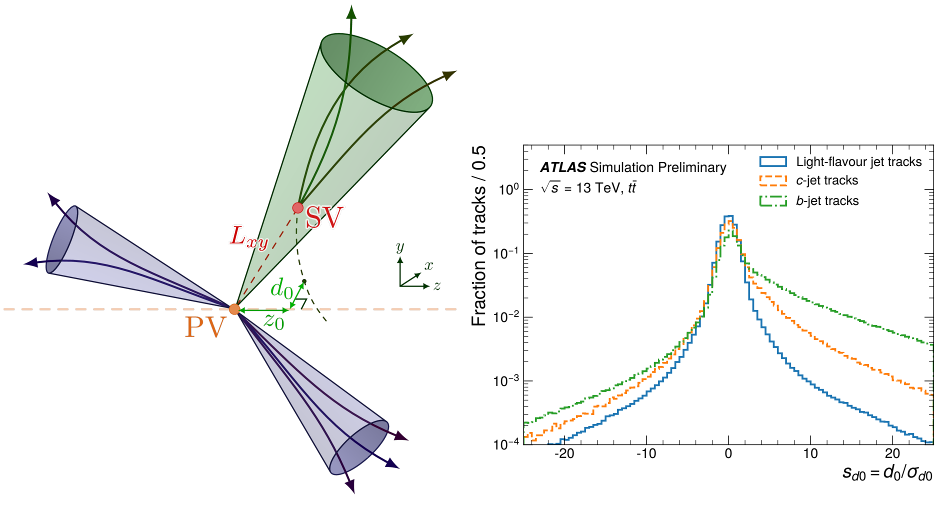

(a) (b)

FIGURE 1 : (a) Schéma représentant deux jets légers (cônes violet) et un jet de b (cône vert) produits à un vertex primaire (PV). Le jet de b se caractérise notamment par son vertex secondaire (SV) et par les paramètres d'impact transverses et longitudinaux d_0 et z_0 des traces en provenant.
(b) Distributions de d_0 par type de saveur de jet (léger, de b ou de c) [1].

Entraînement d'un algorithme de réseau de neurones d'étiquetage des jets de b pour le HL-LHC

Lorsqu'un quark est produit au LHC, il va produire une gerbe de particules collimatées que l'on appelle un *jet*. L'identification de la saveur du quark à l'origine d'un jet, et en particulier des quarks b, est d'importance cruciale pour les analyses de physique avec des quarks de saveur lourde dans l'état final. C'est par exemple le cas avec le boson de Higgs qui se désintègre en une paire de quarks b dans 58% des cas.

Comme illustré en Figure 1, les jets de b présentent des caractéristiques particulières qui permettent leur identification. La durée de vie relativement longue des hadrons composés de quarks b fait que ceux-ci vont se désintégrer à une distance moyenne de quelques mm du point principal d'interaction (le vertex primaire). On peut exploiter ceci de deux façons : en premier lieu, la désintégration du hadron b va entraîner l'existence d'un vertex secondaire vers lequel pointent une partie des traces de l'évènement, permettant ainsi sa reconstruction. En second lieu, les traces issues de cette désintégration vont avoir des paramètres d'impact transverses et longitudinaux par rapport au vertex primaire très grands.

Les algorithmes développés par la collaboration ATLAS pour l'identification (appelé *étiquetage*) des jets de b se regroupent sous la forme d'algorithmes dits de bas-niveau qui exploitent les deux caractéristiques des jets de b décrits précédemment, et des algorithmes de haut-niveau qui regroupent les résultats des premiers algorithmes pour produire un discriminant final qui se base sur toutes les méthodes d'identification disponibles. Ainsi DIPS est un algorithme de bas niveau qui repose sur un réseau de neurones d'apprentissage profond basé sur les informations de paramètre d'impact [1]. Un autre algorithme nommé DL1d combine le discriminant de sortie de DIPS ainsi que d'autres algorithmes de bas-niveau comme SV1 (qui utilise les informations sur les vertex secondaires) pour fournir le discriminant final d'étiquetage des jets.

Le Chapitre 3 présente l'entraînement de DIPS dans le cadre de la configuration HL-LHC du détecteur.

Comme indiqué en introduction, le détecteur interne actuel de ATLAS sera totalement remplacé par l'ITk pour le fonctionnement à haute luminosité du LHC en 2029. ITk est constitué d'une partie interne avec des détecteurs à pixels et d'une partie externe en bandes de silicium. Le détecteur, illustré en Figure 2, fera environ 6 m de longueur et 2 m de diamètre et la disposition verticale des sensors permettra d'augmenter l'espace de reconstruction des trajectoires dans la direction du faisceau jusqu'à une pseudorapidité absolue $|\eta|$ de 4 au lieu de 2.5 actuellement.

L'entraînement de DIPS dans la configuration ITk peut s'effectuer avec différents paramètres. Premièrement, DIPS utilise des collections de traces comme information d'entrée et plusieurs sélections peuvent-être effectuées (en plus des contraintes de reconstruction des traces) pour définir l'ensemble d'entraînement. La configuration dite *Tight* a des critères de sélection plus stricts sur les valeurs d'impulsion transverse et de paramètres d'impact que la configuration *Loose* (cf. Tableau 1).

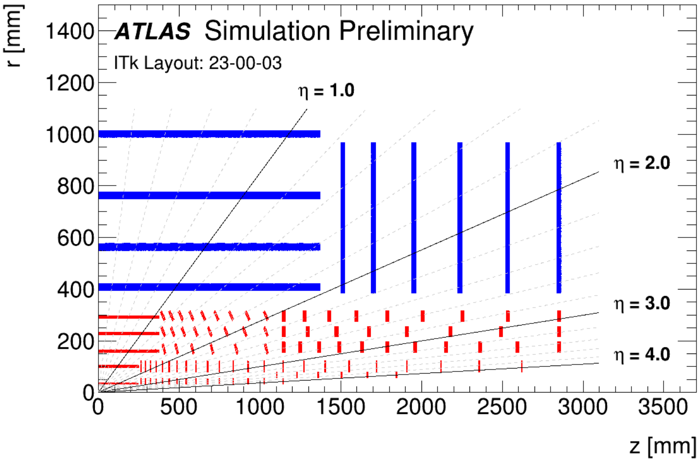

FIGURE 2 : Schéma général de ITk. Seuls les éléments de détection actifs sont illustrés avec les détecteurs à bandes (en bleu) et à pixels (en rouge) [2].

	Tight selection	Loose selection
p_T [MeV]	> 1000	> 500
$\|d_0\|$ [mm]	≤ 1.0	≤ 3.5
$\|z_0 \sin\theta\|$ [mm]	≤ 1.5	≤ 5.0

TABLE 1 : Critères de sélection des traces utilisés pour l'entraînement de DIPS (appliqués en plus des critères de reconstruction des traces).

Deuxièmement, l'entraînement de DIPS s'effectue avec des simulations Monte-Carlo d'évènements $t\bar{t}$ et Z' dans lesquels les jets de b, de c et légers ne sont pas en nombre égal. Comme ceci peut être problématique, une procédure appelé *rééchantillonnage* permet d'égaliser les proportions de jets de différentes saveurs dans l'ensemble d'entraînement. Là encore, plusieurs approches sont possibles comme par exemple en enlevant les jets de saveurs excédentaires (procédure appelée *count*) ou bien en dupliquant les jets de saveurs les moins nombreuses (rééchantillonnage *pdf*).

Toutes ces configurations peuvent être comparées pour déterminer celle donnant les meilleurs résultats. La comparaison entre les différents entraînements s'effectue avec une courbe ROC donnant la réjection des jets légers et de c en fonction de l'efficacité de sélection des jets de b. Comme illustré en Figure 3, l'entraînement effectué avec la sélection de traces *Loose* et la méthode de rééchantillonnage *pdf* obtient les meilleurs résultats.

Comme indiqué plus haut, DIPS n'est pas le discriminant final utilisé pour l'étiquetage des jets. Le discriminant de DIPS sélectionné est utilisé comme paramètre d'entrée d'une version de DL1d spécialement entraînée sur la configuration ITk. DIPS et DL1d peuvent être également comparés à GN1, un algorithme d'étiquetage basé sur des réseaux de neurones à graphe (Figure 4). GN1 présente des meilleures performances que les autres

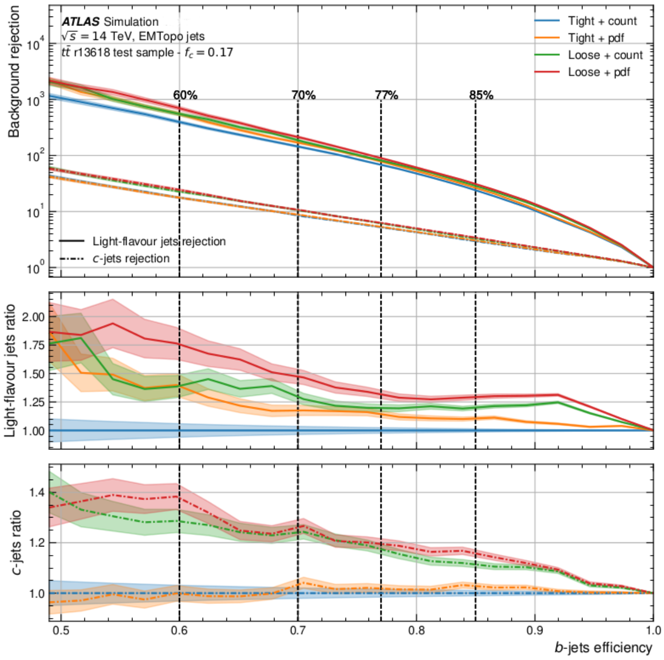

FIGURE 3 : Réjection des jets de c (en bas) et légers (en haut) en fonction de l'efficacité de sélection des jets de b pour les 4 combinaisons d'entraînement testées.

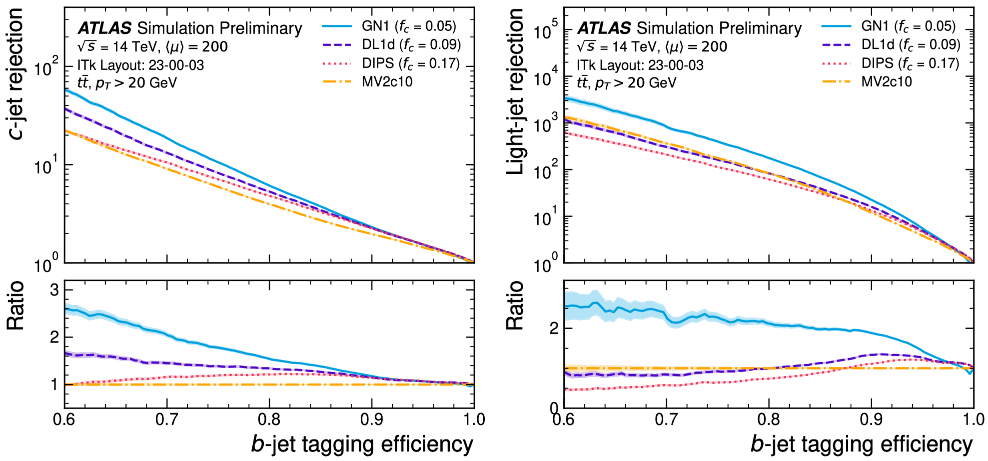

FIGURE 4 : Réjection des jets de c (à gauche) et légers (à droite) en fonction de l'efficacité de sélection des jets de b pour les algorithmes DIPS, DL1d et GN1 dans la configuration de ITk [3].

algorithmes avec une réjection des jets de c et légers environ deux fois plus grande pour une efficacité de sélection des jets de b de 70%. Ces travaux sont présentés en détail dans une note publique de la collaboration ATLAS [3].

Recherche de nouvelles particules scalaires dans le canal $X \rightarrow S(\rightarrow b\bar{b})H(\rightarrow \gamma\gamma)$

Comme indiqué en introduction, il est connu que le Modèle Standard n'est pas la théorie ultime décrivant les particules élémentaires et qu'une "nouvelle physique" existe pour le compléter. Celle-ci pourrait être observée à travers un secteur de Higgs étendu par de nouvelles particules scalaires (i.e de spin nul) comme prédit par certains modèles comme le modèle à deux doublets de Higgs (2HDM) [4] ou certains modèles de supersymétrie [5].

Dans cette analyse, deux nouvelles particules scalaires X et S sont recherchées avec les données du Run 2 représentant 140 fb^{-1} collectés par ATLAS dans des collisions entre protons à $\sqrt{s} = 13$ TeV. Le canal de désintégration utilisé est $X \rightarrow SH$ dans lequel S se désintègre en une paire de quarks b et H est le boson de Higgs du MS qui se désintègre en une paire de photons.

Les plages des masses considérées sont entre 170 et 1000 GeV pour X et entre 15 et 500 GeV pour S. Des recherches similaires ont été menées dans le même état final [6] ou bien d'autres comme $b\bar{b}b\bar{b}$ [7] ou $b\bar{b}\tau^+\tau^-$ [8] mais cette analyse est la première à sonder des valeurs de m_X et m_S inférieures à respectivement 250 et 50 GeV.

La sélection des évènements est la même que celle utilisée pour l'analyse $HH \rightarrow b\bar{b}\gamma\gamma$ qui partage le même état final. Les évènements sont sélectionnés s'ils ont :

- Deux photons isolés et bien identifiés et ayant une impulsion transverse vérifiant $p_T > 0.35 m_{\gamma\gamma}$ pour le photon principal et $p_T > 0.25 m_{\gamma\gamma}$ pour le secondaire. La masse invariante des deux photons $m_{\gamma\gamma}$ doit également être comprise entre 105 et 160 GeV.
- Entre 2 et 5 jets centraux (i.e avec une pseudorapidité $|\eta| < 2.5$) parmi lesquels exactement un ou deux sont étiquetés jets de b avec une efficacité de sélection de 77%.

En effet, pour certaines hypothèses de signal quand $m_S \ll m_X$, les jets de b issus de la désintégration de S sont collimatés dans la même direction et sont donc reconstruits comme un seul jet dans le détecteur. Une région de recherche avec un seul jet étiqueté jet de b est donc définie pour viser spécifiquement ces signaux. Empiriquement, on observe avec l'efficacité de sélection qu'ils vérifient $m_S/m_X < 0.09$.

Les bruits de fond de l'analyse peuvent être séparés en deux catégories en fonction de $m_{\gamma\gamma}$. Le bruit de fond résonant est composé d'évènements avec un seul boson de Higgs qui comportent aussi la désintégration caractéristique $H \rightarrow \gamma\gamma$ et dont les principaux représentants sont ttH et ZH. Le bruit de fond continu est composé d'évènements avec deux photons et d'autres jets quelconques regroupés sous le label "$\gamma\gamma$ + jets ". Une région de signal (SR) est donc définie (une pour chacune des sélections avec 1 ou 2 jet(s) étiqueté de b) pour les évènements vérifiant $120 < m_{\gamma\gamma} < 130$ GeV. A l'intérieur des SR, le bruit de fond continu reste tout de même dominant en terme de nombre d'évènements.

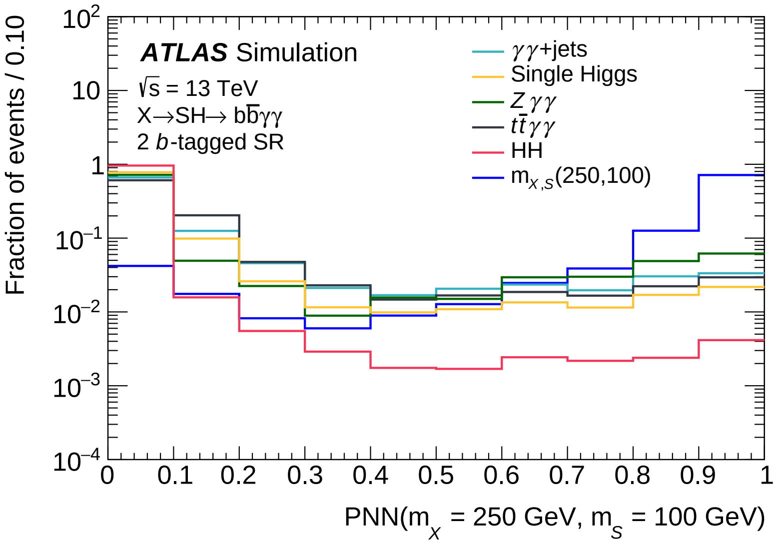

FIGURE 5 : Exemple de distribution du score du PNN pour les paramètres (m_X, m_S) = (250, 100) GeV des différents bruits de fond et du signal correspondant dans la région avec 2 jets de b. Toutes les distributions sont normalisées à l'unité.

Les évènements en dehors de celle-ci mais compris dans la sélection initiale forment la région de contrôle et qui sert notamment à contraindre la normalisation du bruit de fond continu.

Un algorithme basé sur un réseau de neurones d'apprentissage profond paramétrique (PNN) est entraîné pour distinguer le signal du bruit de fond résonnant et continu au sein de la région de signal. Les paramètres du PNN sont les masses des particules recherchées m_X et m_S ce qui permet de cibler précisément une hypothèse de signal donnée. Dans la région avec un seul jet de b, seul m_X est utilisé car aucune information sur m_S ne peut-être obtenue dans l'unique jet reconstruit.

Dans la région à 2 jets de b, les informations utilisées par le PNN pour effectuer la discriminations sont les masses invariantes $m_{b\bar{b}}$ et $m^*_{b\bar{b}\gamma\gamma}$ (avec $m^*_{b\bar{b}\gamma\gamma} = m_{b\bar{b}\gamma\gamma} - (m_{\gamma\gamma} - 125\text{ GeV}))$ qui correspondent aux masses de S et X. De manière similaire, dans la région 1 jet de b, $m_{b\gamma\gamma}$ et p_T^b sont utilisés car la masse invariante d'un seul jet n'est pas calibrée correctement ce qui oblige à utiliser l'impulsion transverse à la place.

Le PNN est entraîné sur des simulations Monte-Carlo de signal et des bruits de fond principaux $\gamma\gamma$ + jets, ttH, ZH et ggFH. Dans la région avec 1 jet de b, les processus VBF H et HH sont également utilisés. L'intérêt du PNN est qu'il ne nécessite qu'un seul entraînement global sur tous les signaux grâce aux paramètres d'entrée au lieu d'avoir autant d'entraînements à réaliser que d'hypothèses de signal à tester.

La Figure 5 montre un exemple de distribution du score du PNN dans la région avec 2 jets de b. Le PNN donne en sortie un score compris entre 0 et 1 pour chaque événement et la distribution de ces scores montre comme voulu que les bruits de fond obtiennent un

		Incertitudes de normalisation (%)					
	Source	ttH	ZH	HH	ggFH	$(m_X, m_S) = (250, 110)$	$(600, 170)$
Évènement	Déclenchement via photons	1.0	1.0	1.0	1.0	1.0	1.0
	Empilement	0.9	0.8	0.6	0.4	1.1	0.5
Photons	Résolution en énergie	0.4	0.4	0.3	0.4	0.6	0.3
	Échelle d'énergie	0.2	0.2	0.1	0.1	0.5	0.4
	Identification	1.6	1.6	1.4	1.6	2.0	1.8
	Isolation	1.6	1.6	1.5	1.6	1.7	1.4
Jets	Échelle d'énergie	1.4	0.9	0.6	1.8	1.2	0.4
	Résolution en énergie	7.3	4.6	2.9	7.5	5.8	2.5
Étiquetage de saveur	Efficacité des jets de b	2.1	3.0	2.5	3.1	3.7	2.2
	Efficacité des jets de c	0.4	0.7	0.1	1.7	0.1	0.0
	Efficacité des jets légers	0.8	0.4	0.4	2.7	0.4	0.5

TABLE 2 : Incertitudes de normalisation (en %) dans la SR pour les bruits de fond principaux et deux exemples de signal dans la région avec 2 jets de b.

score proche de 0 et le signal visé un score proche de 1.

Une part importante de mon travail a été d'implémenter la prise en compte des incertitudes systématiques expérimentales et d'en mesurer l'impact sur le résultat final. Celles-ci sont prises en compte via des simulations Monte-Carlo dédiées. L'acceptance des différentes sélections peut-être ainsi affectée ce qui impacte la distribution du score PNN en changeant la normalisation des différents processus. La distribution en elle-même varie également dans chaque bin : on parle d'incertitude de forme.

Le Tableau 2 montre les incertitudes de normalisation sur les bruits de fond principaux ainsi que sur deux exemples de signaux. Celles-ci ne dépassent pas 8% par type d'incertitude. Les catégories dominantes sont la résolution en énergie des jets et l'étiquetage des jets de b. Pour les signaux, ces incertitudes varient en fonction de m_X et m_S et sont de manière générale plus importantes à basse masse.

D'autres types d'incertitudes affectent l'analyse : les incertitudes systématiques théoriques qui regroupent les variations liées aux incertitudes des quantités physique impliquées comme la valeur de la constante de l'interaction forte α_S ou la valeur de la section efficace de production d'un processus. L'incertitude principale dans cette catégorie et de l'analyse en général est celle liée à la modélisation des évènements $\gamma\gamma +$ jets dans la SR.

Les résultats de l'analyse sont obtenus par un fit binné de la distribution du score PNN maximisant la fonction de vraisemblance. Celle-ci est obtenue en comparant le nombre d'évènements attendus dans chaque bin au nombre d'évènements observés au moyen d'une loi de Poisson. Le paramètre d'intérêt du fit est la section efficace du signal $X \to SH \to b\bar{b}\gamma\gamma$. Les incertitudes systématiques aussi bien théoriques que expérimentales sont prises en compte comme paramètres de nuisance dans le fit.

Un test statistique permet de comparer les hypothèses de découverte du signal et de bruit

de fond uniquement. Les données sont globalement conformes avec l'hypothèse bruit de fond uniquement. L'écart le plus important est observé pour $(m_X, m_S) = (575, 200)$ GeV où l'hypothèse de signal a une significance statistique de 3.55σ. Il faut cependant prendre en compte le fait que la multitude de tests réalisés pour toutes les hypothèses de masse augmente statistiquement la probabilité d'observer un excès quelque part. Avec ce *look-elsewhere effect*, la significance statistique globale est de 2.0σ.
Comme aucun excès par rapport au bruit de fond n'est détecté, des limites supérieures pour la section efficace de production au seuil de confiance de 95% sont établies. Ces limites sont illustrées en Figure 6.

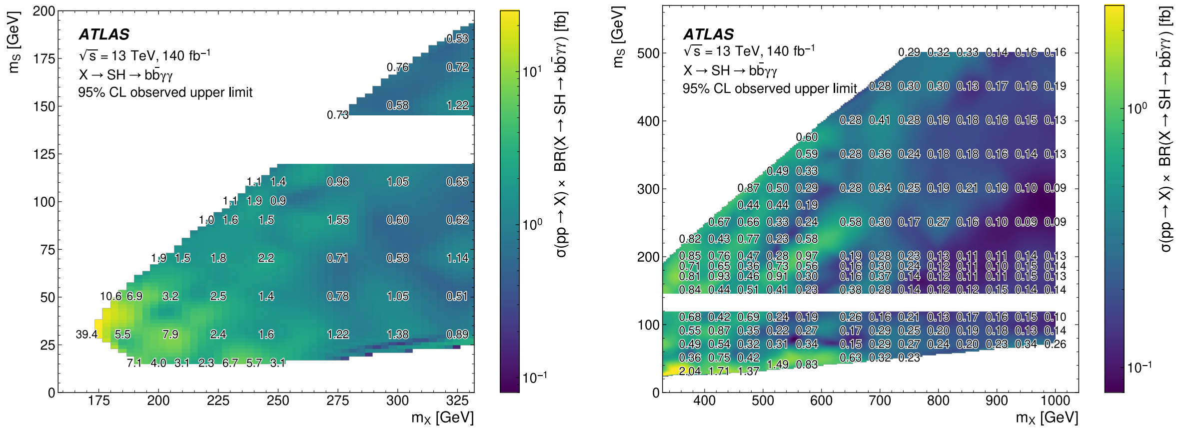

(a)

(b)

FIGURE 6 : Limites supérieures sur la section efficace de production du signal $X \to SH$ dans l'état final $b\bar{b}\gamma\gamma$ dans le plan (m_X, m_S) pour les petites (a) et grandes (b) valeurs de m_X [9].

Les limites observées varient entre 39 fb pour $(m_X, m_S) = (170, 30)$ GeV (25 fb attendu) et 0.09 fb pour (1000, 250) GeV (0.14 fb attendu). La sensibilité de l'analyse diminue à basse masse en raison d'une efficacité de sélection du signal plus faible. A haute masse, l'efficacité est relativement constante tandis que la quantité de bruit de fond diminue ce qui explique une meilleure sensibilité. Les limites sont également logiquement plus élevées à l'endroit où est observé le léger excès discuté plus haut.
Pour finir, l'impact des incertitudes systématiques expérimentales peut-être estimé en regardant leur effet sur la limite attendue en enlevant leur contribution en tant que paramètres de nuisance. Le ratio entre les limites supérieures obtenues dans ce cas et lorsqu'elles sont prises en compte est montré en Figure 7.

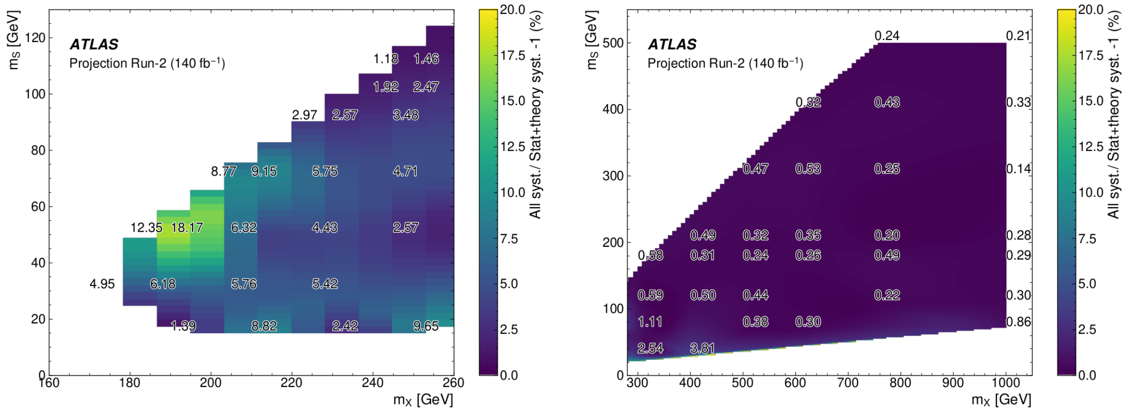

(a)

(b)

FIGURE 7 : Différence relative entre les limites attendues obtenues avec et sans tenir compte des incertitudes systématiques expérimentales dans la région avec 2 jets de b pour les petites (a) et grandes (b) valeurs de m_X.

Comme indiqué plus haut, l'effet des incertitudes expérimentales varie en fonction de m_X et m_S. Les incertitudes liées à l'étiquetage de saveur des jets diminuent avec l'impulsion transverse p_T ce qui signifie qu'elles sont plus importantes à basse masse ou quand $m_X \gg m_S$. Il en est de même pour les incertitudes liées à la résolution en énergie des jets. Pour ces raisons, l'impact des incertitudes expérimentales sur la limite est plus important à bas m_X ou il peut atteindre 20%. A haute masse, celui-ci reste en dessous des 1%.

Pour conclure, cette analyse présente donc une méthode innovante pour sonder l'état final $b\bar{b}\gamma\gamma$ via des réseaux de neurones paramétriques. Elle est sensible à l'excès détecté par l'expérience CMS dans le même état final pour (m_X, m_S) = (650, 90) GeV. Nos résultats ne confirment pas cet excès et établissent des limites supérieures sur la section efficace de production du signal $X \to SH$ sur tout l'espace des masses m_X et m_S testées.

Contents

List of Figures

List of Tables

Introduction

The description of the elementary components of matter have been a subject of interest since the Classical era. Today, modern science have provided two theories that describe the Universe at the fundamental level : General Relativity which is the description of gravity and models the Universe at the astronomical scale and the Standard Model of particle physics (SM). In this thesis, we will focus on the Standard Model, which describes the elementary particles and their interactions at the smallest scale with a quantum field theory.

The Standard Model was established during the second half of the 20th century following a huge theoretical effort to account for the experimental results of that time. The resulting theory is based on strong mathematical principles such as local gauge invariance and mediating particles which are associated to the fundamental interactions. The Standard Model has made predictions that were confirmed experimentally sometimes decades after the original prediction, as with the Higgs boson, discovered in 2012.

However, it is established that the Standard Model does not perfectly describe our Universe. The most obvious flaw is that it does not incorporate gravity due to the lack of a quantum theory of gravitation but it also does not account for some astronomical phenomena such as the existence of dark matter. Therefore, everything seems to point out to that a theory beyond the Standard Model exists, of which the SM could be a (very good) low energy approximation.

In this context, the Higgs mechanism and the Higgs boson which was discovered by the CMS and ATLAS experiments at CERN appear to be of crucial importance. The Higgs mechanism is a feature of the Standard Model explaining the particles masses with a phenomenon named spontaneous symmetry breaking. However, the mechanism might take another form beyond the one described by the Standard Model, potentially addressing some of the unresolved questions in physics. Consequently, Higgs boson physics remains a focal point in the search for new physics.

The Higgs boson, which lies at the heart of the Higgs mechanism, has been thoroughly studied during the last decade to check if its characteristics remain consistent with the SM predictions. But many important features have not been probed yet, such as the Higgs boson self coupling which is linked to the form of the Higgs potential. Chapter 1 provides a description of the Standard Model and the Higgs mechanism as well as an overview of current Higgs boson physics and possible Beyond the Standard Model theories linked to the Higgs sector.

The experimental exploration of the Higgs mechanism has been made possible by the CERN infrastructure and especially the Large Hadron Collider (LHC). This particle accelerator collides protons at an energy of 13.6 TeV which makes it the current "energy frontier". The CMS and ATLAS detectors are located on the LHC and record what is happening during the collisions.

These detectors must constantly be upgraded in an effort to keep on with the best technologies available and the change of the accelerators parameters. A new phase called High-Luminosity LHC will begin in 2029 with the objective to increase the accelerator luminosity to collect more data. The detection systems will have to be transformed accordingly to cope with the harsher environment and as such the current ATLAS Inner Detector will be replaced by the brand new Inner Tracker (ITk). Chapter 2 presents in detail the ATLAS experiment and the main modifications that are bound to happen for the HL-LHC phase.

It is crucial to asses that the combined performance of the detector remain at a good level with the new configuration. Chapter 3 presents the adaptation of a flavour tagging algorithm named DIPS to the HL-LHC configuration. Flavour tagging consists in identifying the quark at the origin of a jet in the detector. It is particularly important because heavy flavour quarks are often produced by Higgs boson decays.

Finally, Chapter 4 presents an ATLAS analysis to research two additional scalar particles X and S which could extend the Higgs sector in the $X \to S(\to b\bar{b})H(\to \gamma\gamma)$ decay channel. An overview of the analysis strategy will be provided with a particular stress on the systematic uncertainties since they were my main contribution to the analysis.

1 Theoretical introduction and Higgs boson searches at LHC

Table of contents

Introduction

Our current way of understanding the fundamental building blocks of matter, the elementary particles, is described by a theory called the Standard Model (SM).
Without going all the way back to the classical era and the idea of the atom, the history of particle physics can be traced back to the very end of the 19th century with the discovery of the electron by Thomson in 1897. In the first half of the 20th century, many other particles were identified, either in the laboratory like the neutron or directly in nature when the observation of the cosmic rays reaching Earth led to the discovery of the muon. At first, the observed particles corresponded to the building blocks of the matter surrounding us like the protons, neutrons and electrons forming the different atoms. But in the 1950s, tons of other particles were produced and observed in particle accelerators without any apparent ordering, a situation described as ’a zoo of particles’ [10].
Then, similarly to what happened with the Periodic Table of Elements, a classifying model of the new discovered particles called the ’Eightfold way’ was suggested by Gell-Mann [11]. The underlying justification behind the Eightfold way was soon found when the quark model was proposed by Gell-Mann and Zweig in 1964 [12, 13]. All

previously discovered particles including the proton and the neutron were considered to be made of different arrangement of quarks, a new type of smaller and elementary particles.

Important progresses were made in parallel to uncover the different interactions between the particles. In the 1960s, Glashow, Weinberg and Salam united the electromagnetism and the weak interaction in a single model called the electroweak theory [14, 15, 16]. It is a quantum field theory (QFT) which is based on the mathematical concept of gauge symmetry [17]. The picture was completed by Quantum Chromodynamics (QCD), the theory of the strong interaction which affects the quarks and describes how the atomic nucleus holds together.

The overall theory regrouping them, now called the Standard Model of particle physics, allowed to have a coherent way of describing the elementary particles and their interactions. Decisive proofs of the model happened with the discovery of the neutral currents in 1973 and of the W and Z bosons mediating the electroweak interaction at CERN in 1983 with masses corresponding to the theory prediction. Its coronation waited about 30 years when the Higgs boson, a particle crucial for a feature of the model called electroweak symmetry breaking, was discovered at CERN in 2012. The Higgs boson discovery about half a century after its prediction is a decisive result for the coherence and predictive power of the theory.

However, as performing as the Standard Model is, it still does not address some fundamental questions in physics such as the description of gravity, the 4th fundamental force of nature. Interestingly, one of the best way to overcome the Standard Model is to study its prediction with very high precision to find a discrepancy with experimental results which could hint at an underlying physics beyond it. In particular, the newly discovered Higgs boson and the global Higgs physics sector constitutes a promising portal to probe these questions.

In this chapter, an overview of the Standard Model and its underlying mathematical structure is given in 1.1. The Higgs mechanism, a crucial feature of the model and the global subject studied in this thesis is introduced in 1.2. Finally, the limitations and flaws of the Standard Model and possible hints to overcome it and study them at LHC are detailed in 1.3.

1.1 The Standard Model of Particle Physics

The first part of this section introduces the fundamental particles of the Standard Model and their categories. The three other parts will describe the interactions between them, which are conveniently also represented by particles.

1.1.1 Classification of elementary particles

All currently known fundamental particles are shown in Figure 1.1 along with their symbol, mass, electric charge and spin properties. Each particle belongs to one of the two distinct categories of the **bosons** which have integer spin and the **fermions** which have half-integer spin. At the elementary particle level, the fundamental bricks of matter are fermions (with a spin $s = 1/2$) and the particles carrying the interactions are bosons. A major difference between them arises with their collective behaviour as fermions follow the Fermi-Dirac statistics whereas bosons follow the Bose-Einstein statistics.

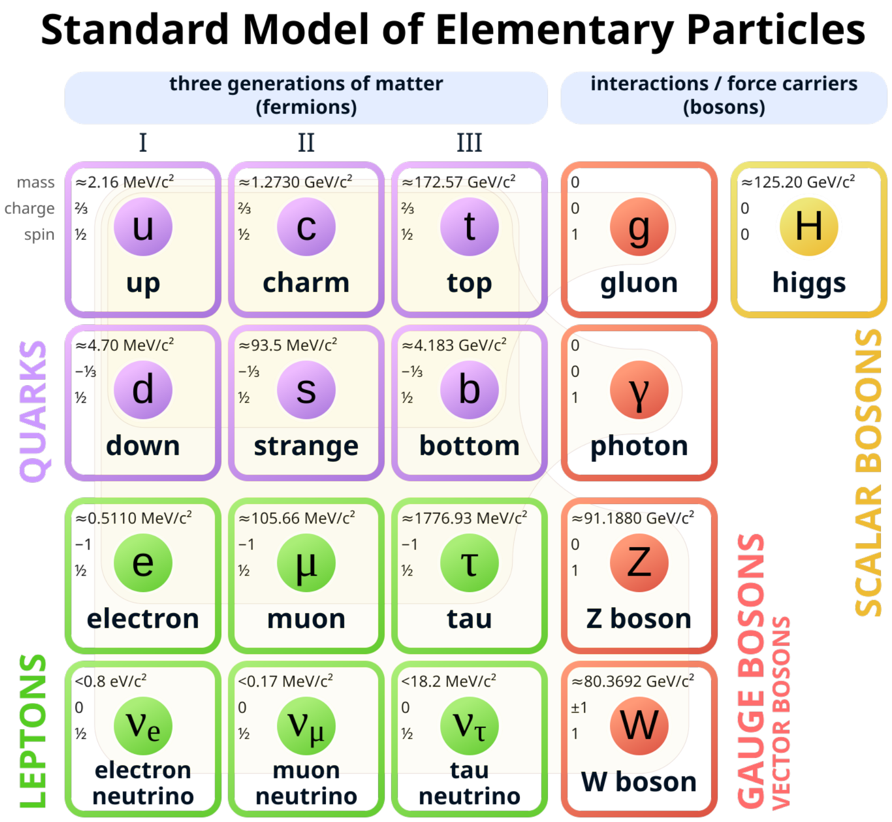

Figure 1.1: Table displaying all the known elementary particles from the Standard Model [18].

The elementary bosons are :

- The **photon** γ : it is the particle mediating the electromagnetic force.
- The **gluons** g : at the numbers of 8, they are the mediators of the strong interaction. Contrary to photons which are uncharged, gluons carry a colour charge and are therefore sensitive to the interaction that they are mediating.
- The $W^{\pm}$ and Z **bosons** : they are the mediators of the weak interaction. Contrary to gluons and photons, these particles have a non-zero mass.

- The **Higgs boson** H : this particle is not mediating any interaction but is rather at the origin of the mass of the W and Z bosons and all the fermions with a process called the Higgs mechanism which will be explained in Section 1.2.

The elementary fermions are divided in two categories :

- **Quarks** are particles sensitive to the strong interaction. There are six different quarks (they are called *flavours*) and they come in three *generations* which means that from one generation to another the particles are identical except for their masses. The quarks from the first generation which are the lightest are therefore the only one that are stable. The up (u), charm (c) and top (t) quarks have an electric charge of 2/3 while the down (d), strange (s) and bottom (b) quarks have a charge of -1/3 (in terms of fraction of the elementary charge e).

- **Leptons** are the remaining fermions which are not sensitive to the strong interaction. Leptons are also subdivided into charged leptons which have electric charge of -1 and neutrinos which don't have any electric charge. The charged leptons are the electron (e), the muon (μ) and the tau (τ) and they get heavier with each generation similarly to quarks. For each charged lepton there is an associated neutrino with which they form a doublet : the electron-neutrino (ν_e), the muon-neutrino (ν_μ) and the tau-neutrino (ν_τ). The neutrinos have a really small yet non zero mass which has not been measured yet.

All these particles also have counterparts called *antiparticles* which are absolutely identical except that they have an opposite charge.

Composite particles Elementary particles can be combined to form composite particles. Combinations of 2 and 3 quarks are respectively named *mesons* and *baryons* and a combination of any number of quarks is called a *hadron*. Some of them are quite familiar : protons, composed of 3 valence quarks, 2 up and one down, and neutrons, composed of 2 d and one u, are the basis of the atomic nuclei. Along with electrons, they form the atoms. As such, the ordinary matter surrounding us is conveniently only composed of fermions from the first generation that are stable. Antimatter particles can also be stable, however their effective lifetime is short as they would be annihilated should they come across any particle of ordinary matter.

The Standard Model is a Quantum Field Theory (QFT) that mainly consists in the regroupment of Quantum Chromodynamics (QCD) describing the strong interaction and the Electroweak theory (sometimes written EWT) describing the electroweak interaction which includes the electromagnetic and the weak forces. The electromagnetic interaction alone is described by Quantum Electrodynamics (QED). According to the QFT, the elementary particles can be seen as excitations of different quantum fields. Their interactions rely on the local gauge invariance principle which means that the interaction laws are invariant against certain group of symmetries. The SM gauge invariance group is :

$$SU(3)_C \otimes SU(2)_L \otimes U(1)_Y \tag{1.1}$$

where $SU(3)$ is the symmetry group of QCD and $SU(2) \otimes U(1)$ is the one of the electroweak interaction. These symmetry groups and the corresponding interactions will be described in more details in the next section.

1.1.2 Quantum Electrodynamics

The interactions between particles are described by a Lagrangian (or more accurately a Lagrangian density). Lagrangians are the keystone of any theory as the equations of motion can directly be obtained from them with the Euler-Lagrange equation.
The starting point is the Lagrangian describing free particles (i.e that are not interacting in any way). It is called the Dirac Lagrangian because of its link with the first equation to combine both special relativity and quantum mechanics : the Dirac equation. It describes the free motion of massive spin 1/2 particles which are represented by objects called spinors ψ. Written using the so-called natural units where $e = c = 1$, the Dirac Lagrangian is :

$$\mathscr{L}_{\text{Dirac}} = \bar{\psi}(i\gamma^{\mu}\,\partial_{\mu} - m)\psi \tag{1.2}$$

where γ^{μ} are Dirac gamma matrices, $\partial_{\mu} = \partial/\partial x_{\mu}$ represents the 4^{th} dimensional derivative and $\bar{\psi} = \psi^{\dagger}\gamma^{0}$ [1] is the Dirac adjoint of the spinor.
For QED, the symmetry group under which the Lagrangian and the equation of motions are invariant is $U(1)$. First we can notice that the Dirac Lagrangian is invariant with respect to the global $U(1)$ symmetry which corresponds to a change in the phase of the spinor : $\psi \rightarrow \psi' = e^{i\alpha}\psi$.
Now what will happen if we want the Lagrangian to be invariant under a *local* $U(1)$ symmetry i.e where the phase change α depends on the position x ? The Lagrangian is then transformed as :

$$\begin{aligned}\mathscr{L} \rightarrow \mathscr{L}' &= e^{-i\alpha(x)}\bar{\psi}i\gamma^{\mu}(e^{i\alpha(x)}\partial_{\mu}\psi + i\partial_{\mu}\alpha(x)e^{i\alpha(x)}\psi) - m\bar{\psi}\psi \\ &= \mathscr{L} - i\partial_{\mu}\alpha(x)\psi\end{aligned} \tag{1.3}$$

which is different from the initial Lagrangian. To preserve the local $U(1)$ symmetry, we can replace the initial derivative ∂_{μ} with a *covariant derivative* D_{μ} and assume the existence of a new vector field A_{μ} that transforms as follows :

$$\begin{aligned}\partial_{\mu} \rightarrow D_{\mu} &= \partial_{\mu} + iqA_{\mu} \\ A_{\mu} \rightarrow A'_{\mu} &= A_{\mu} - \frac{1}{q}\partial_{\mu}\alpha\end{aligned}$$

---

[1] Here † represents the complex conjugate

where q is a constant representing the strength of the interaction. Adding this term will conveniently cancel out the additional terms and assure the local $U(1)$ symmetry at the cost of modifying the initial Lagrangian. This new QED Lagrangian is then :

$$\mathscr{L}_{QED} = \bar{\psi}(i\gamma^{\mu}D_{\mu} - m)\psi - \frac{1}{4}F_{\mu\nu}F^{\mu\nu} \tag{1.4}$$

where $F_{\mu\nu} = \partial_{\mu}A_{\nu} - \partial_{\nu}A_{\mu}$. It can also be written like this to illustrate more explicitly its physical meaning :

$$\mathscr{L}_{QED} = \bar{\psi}(i\gamma^{\mu}\partial_{\mu} - m)\psi - q\bar{\psi}\gamma^{\mu}A_{\mu}\psi - \frac{1}{4}F_{\mu\nu}F^{\mu\nu} \tag{1.5}$$

- The first term is the initial Dirac Lagrangian representing the free propagation of the fermions.
- The second term $-q\bar{\psi}\gamma^{\mu}A_{\mu}\psi$ represents the interaction between the fermions and the particle mediating the electromagnetic interaction, which is of course the photon. The coupling strength of the interaction is simply the electric charge q.
- The last term $-\frac{1}{4}F_{\mu\nu}F^{\mu\nu}$ is the kinetic term of the propagation of the photons.

Quantum electrodynamics has allowed us to show the recipe that will be identical for the other interactions described by the SM : start from the free particle Lagrangian, impose a local gauge invariance under a certain symmetry group and then cancel the additional terms that arise with new fields to preserve the symmetry. The new fields correspond to additional particles mediating the interaction.

1.1.3 Quantum Chromodynamics

The strong interaction which is responsible for the binding of the atomic nucleus is described in the Standard Model by a theory called Quantum Chromodynamics (QCD). The associated symmetry group of the strong interaction is $SU(3)_C$ which is the group of unitary 3×3 complex matrices, and the generators of this group are the Gell-Mann matrices λ_a. C stands for *colour* which is the "charge" of the strong interaction.
Starting from the Dirac Lagrangian again, the corresponding change under $SU(3)_C$ for the spinor is :

$$\psi(x) \to \psi'(x) = e^{ig_S\alpha^a(x)\frac{\lambda_a}{2}\psi(x)} \tag{1.6}$$

where g_S is the coupling constant that represents the strength of the strong interaction. The a index ranges from 1 to 8 and stands for every of the 8 Gell-Mann matrices. The covariant derivative that will cancel additional terms is :

$$D_{\mu} = \partial_{\mu} + ig_S\frac{\lambda_a}{2}G^a_{\mu} \tag{1.7}$$

G^a_μ are eight gauge fields that represent the gluons mediating the strong interaction. To respect the gauge invariance, they must verify :

$$G^a_\mu \rightarrow G'^a_\mu = G^a_\mu + \alpha^b(x) f^{abc} G^c_\mu + \frac{1}{g_S}\partial_\mu \alpha^a(x) \tag{1.8}$$

where f^{abc} are the structure constants of $SU(3)_C$ and are linked to the commutation relations between Gell-Mann matrices. In addition, the gluons fields strength tensors verify :

$$G_a^{\mu\nu} = \partial_\mu G^a_\nu - \partial_\nu G^a_\mu + g_S f^{abc} G^b_\mu G^c_\nu \tag{1.9}$$

which introduces trilinear and quadrilinear terms of interactions between gluons themselves. In the end, the QCD Lagrangian is :

$$\mathscr{L}_{QCD} = \bar{\psi}(i\gamma^\mu \partial_\mu - m)\psi - g_S \psi \gamma^\mu \frac{\lambda_a}{2} \psi G^a_\mu - \frac{1}{2} G_a^{\mu\nu} G^a_{\mu\nu} \tag{1.10}$$

Like for QED, the physical meaning is obtained by separating the Lagrangian between the free propagation term, the quarks and gluons interaction term and finally the gluons propagation term which comes along with self-interaction between them.

A particularity of QCD that turns out to have a lot of experimental impact is that the strong interaction coupling constant α_s depends on the energy scale considered. At high energy and short distances like inside a proton, the coupling constant is small ($\alpha_S = o(1)$), QCD can be approximated as a perturbation theory and quarks can be considered as free particles, a phenomenon called *asymptotic freedom*.
On the other hand, at low energy, α_s is of the order of 1 which means that QCD is non perturbative. When two quarks are pulled apart, the gluons from the interaction, which are also interacting between each other, make a significant contribution to the attraction between the initial quarks because of the large value of α_S (Figure 1.2 - left). As a result, coloured objects cannot propagate as free particles and quarks and gluons form bound states that are colourless. This is known as *colour confinement* [19].

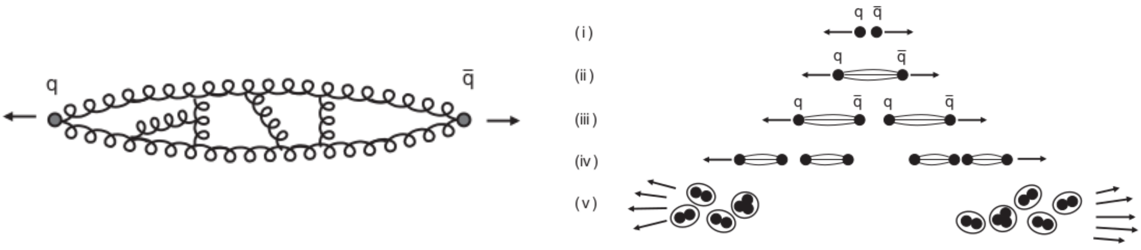

Figure 1.2: Sketches illustrating the gluon-gluon interactions between quarks at long range (left) and the process of hadronization (right). Figures from [19] pp. 249-253

.

Experimentally, when a quark-antiquark pair is produced in a particle accelerator, they will first move away from each other until the increasing interaction energy between them becomes so large that a new quark - antiquark pair can be produced. This process repeats itself until newly created pairs have low enough energy to form bound hadrons states. As a result, single quarks are never observed directly but their signature in a particle detector is a stream of hadrons and other particles grouped in a single direction named *jet*. The whole process is named *hadronization* (Figure 1.2 - right).
The reconstruction of jets and the identification of the original quarks are of key importance in physics analyses presented in this thesis and involving quarks in the final state.

1.1.4 Weak and electroweak interaction

The weak interaction is the force responsible of the radioactive β decay and plays an important role in the nuclear fission and fusion. It was first described by Fermi who proposed a four fermions point-like interaction model in 1933. In the 1960s, it was included in the electroweak theory from Glashow, Weinberg and Salam [14, 15, 16] which unites the weak and the electromagnetic forces in a single unified theory.
The gauge symmetry group under which electroweak theory is build is $SU(2)_L \otimes U(1)_Y$ where $SU(2)$ is the non abelian group of unitary complex matrices of dimension 2. Its generators are the Pauli matrices σ_x, σ_y and σ_z, well-known for their representation of the spin group in quantum mechanics.
A particularity of the weak interaction is that it violates parity which means that it does not treat left and right handed [2] components of a particle in the same way. To reflect this in the equations, the left and right handed components of fermions (written L and R) are respectively regrouped in a doublet and a singlet such that :

$$\psi = \begin{pmatrix} L \\ R \end{pmatrix} \text{ where } L = \begin{pmatrix} \nu_e \\ e_L \end{pmatrix} \text{ and } R = e_R \tag{1.11}$$

$U(1)_Y$ symmetry (which is not exactly the same as the $U(1)$ from QED) affects both left and right-handed components with the following transformation :

$$\psi \to \psi' = e^{\frac{i}{2}\beta(x)}\psi \tag{1.12}$$

To impose local gauge invariance we introduce a new gauge field B_μ which transforms as $B_\mu \to B_\mu - \frac{1}{Yg'}\partial_\mu \beta(x)$ exactly like in QED. The charge of the $U(1)$ group is called the **weak hypercharge** Y and g' is the corresponding coupling constant.
On the other hand, $SU(2)_L$ only affects left handed doublets, therefore the transformation

---

[2] The right/left handed components of a particle are defined in the sense of the chirality operators P_R and P_L. Formally $\psi = P_R\psi_R + P_L\psi_L$ where $P_L = \frac{1-\gamma^5}{2}$ and $P_R = \frac{1+\gamma^5}{2}$ where γ^5 is a Dirac gamma matrix.

is :

$$\begin{pmatrix} \nu_e \\ e_L \end{pmatrix} \to e^{\frac{i}{2}\sigma_j \alpha(x)^j} \begin{pmatrix} \nu_e \\ e_L \end{pmatrix} \text{ and } e_R \to e_R \tag{1.13}$$

Similarly, we will have to introduce three new gauge fields $W_\mu^{1,2,3}$ to preserve local gauge invariance. The $SU(2)_L$ charge is the **weak isospin** I and the associated coupling constant is g. Weak isospin obeys similar laws as angular momentum spin, hence explaining the left handed doublet (which have $I = 1/2$ and eigenvalues $I_3 = \pm 1/2$) and right-handed singlet (which have $I = 0$ and do not participate in the weak interaction). These new quantum numbers are linked to the electric charge Q with the Gell-Mann-Nishijima formula :

$$Q = I_3 + \frac{Y}{2} \tag{1.14}$$

The weak isospins and electric (hyper)charges of the elementary particles are regrouped in Table 1.1.

The covariant derivative that needs to be added in the Lagrangian to guarantee the symmetry is :

$$D_\mu = \partial_\mu - \frac{i}{2} g' Y B_\mu - \frac{i}{2} g I \sigma_j W_\mu^j \tag{1.15}$$

Finally, we can write the electroweak Lagrangian using our left and right-handed components L and R :

$$\mathscr{L}_{EW} = \bar{R} i \gamma^\mu (\partial_\mu + i g' B_\mu) R + \bar{L} i \gamma^\mu (\partial_\mu - \frac{i}{2} g \sigma_j W_\mu^j + \frac{i}{2} g' B_\mu) L - \frac{1}{4} W_{\mu\nu}^j W_j^{\mu\nu} - \frac{1}{4} B_{\mu\nu} B^{\mu\nu} \tag{1.16}$$

where $W_{\mu\nu}^j = \partial_\mu W_\nu^j - \partial_\nu W_\mu^j + g W_\mu^j \times W_\nu^j$ and $B_{\mu\nu} = \partial_\mu B_\nu - \partial_\nu B_\mu$.

A subtlety is that the new fields introduced to fix additional terms and ensure gauge invariance B_μ and $W^{1,2,3}$ do not correspond directly to real particles physical states. They are rather mixing combinations of those fields :

$$W_\mu^\pm = \frac{1}{\sqrt{2}} (W_\mu^1 \pm i W_\mu^2) \tag{1.17}$$

$$\begin{pmatrix} A_\mu \\ Z_\mu \end{pmatrix} = \begin{pmatrix} \cos\theta_W & \sin\theta_W \\ -\sin\theta_W & \cos\theta_W \end{pmatrix} \begin{pmatrix} B_\mu \\ W_\mu^3 \end{pmatrix} \tag{1.18}$$

We therefore obtain the $W^\pm$ and Z bosons fields and also get back our electromagnetism photon represented by A_μ. θ_W is called the Weinberg angle and represents the relative strength between electromagnetism and weak interaction :

$$\tan\theta_W = \frac{g'}{g} \tag{1.19}$$

This Lagrangian was build to respect $SU(2)_L \otimes U(1)_Y$ local gauge symmetry but it doesn't contain any mass term for the new $W^\pm$ and Z bosons. Adding them, as well as mass terms for fermions would break the symmetry. However, the weak interaction asso-

LH fermions		Q	Y	I_3	RH fermions		Q	Y	I_3
Leptons	ν_e, ν_μ, ν_τ	0	-1	1/2	Leptons	ν_e, ν_μ, ν_τ	0	0	0
	e^-, μ^-, τ^-	-1	-1	-1/2		e^-, μ^-, τ^-	-1	-2	0
Quarks	u, c, t	2/3	1/3	1/2	Quarks	u, c, t	2/3	4/3	0
	d, s, b	-1/3	1/3	-1/2		d, s, b	-1/3	-2/3	0

Table 1.1: Electroweak quantum numbers (electric charge Q, weak hypercharge Y and weak isospin I_3) of the fermions depending on their chirality.

ciated to these bosons is experimentally found to have a short range which is associated to massive propagators. To address this paradox, a mechanism to spontaneously break the Electroweak symmetry was proposed independently by P.Higgs [20] and by F.Englert and R.Brout [21] in 1964. This Brout-Englert-Higgs (BEH) mechanism, often called Higgs mechanism for short, is described in the next section.

1.2 The Higgs mechanism and Higgs boson properties

1.2.1 Higgs mechanism

The Higgs mechanism is based on the addition of a new complex scalar field to the SM Lagrangian. This field, noted $\phi(x)$, is defined as a $SU(2)$ doublet like :

$$\phi(x) = \begin{pmatrix} \phi^+ \\ \phi^0 \end{pmatrix} = \frac{1}{\sqrt{2}} \begin{pmatrix} \phi^1 + i\phi^2 \\ \phi^3 + i\phi^4 \end{pmatrix} \tag{1.20}$$

with an associated norm $\phi^\dagger \phi$. A potential $V(\phi)$ is associated to this new field :

$$V(\phi) = \mu^2 \phi^\dagger \phi + \lambda (\phi^\dagger \phi)^2 \text{ where } \mu^2, \lambda > 0 \tag{1.21}$$

This potential has a particular shape illustrated in Figure 1.3 which has received the infamous "Mexican-hat" nickname. Its main feature is that it has an unstable local maximum for $\phi = 0$ and its global minimum is reached when :

$$|\phi^\dagger \phi| = -\frac{\mu^2}{2\lambda} \tag{1.22}$$

The $U(1)$ symmetry is still respected and there are an infinity of possible ground states respecting condition 1.22. Any ground state can therefore be taken, a process known as spontaneous symmetry breaking. We write the chosen ground state as :

$$\phi_g = \frac{1}{\sqrt{2}} \begin{pmatrix} 0 \\ \sqrt{\frac{-\mu^2}{\lambda}} \end{pmatrix} = \frac{1}{\sqrt{2}} \begin{pmatrix} 0 \\ v \end{pmatrix} \tag{1.23}$$

where we introduce the vacuum expectation value v : as its name suggests, it is the value taken by the Higgs potential in the ground state.

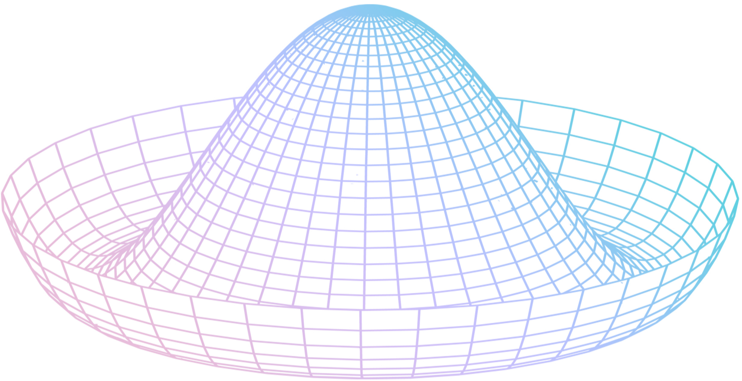

Figure 1.3: Illustrative representation of the Higgs potential in the Re(ϕ) - Im(ϕ) plane [22].

Using perturbation theory we can expand the small perturbations of the field around the ground state like

$$\phi = \frac{1}{\sqrt{2}} \begin{pmatrix} 0 \\ v+H \end{pmatrix} \tag{1.24}$$

A Lagrangian is associated to the new Higgs field and it is build with the covariant derivative to respect the $SU(2) \otimes U(1)$ symmetry :

$$\mathscr{L}_{Higgs} = (D^{\mu}\phi)^{\dagger}(D_{\mu}\phi) - V(\phi) \tag{1.25}$$

Without loss of generality, we can replace the initial Lagrangian with its expansion around the broken symmetry state :

$$\begin{aligned} \mathscr{L}_{Higgs} &= (\partial_{\mu}H)^2 + \frac{g'^2+g^2}{4} Z_{\mu}Z^{\mu}(v+H)^2 + \frac{g^2}{4} W_{\mu}^{+}W^{-\mu}(v+H)^2 - V(v+H) \\ &= (\partial_{\mu}H)^2 + \frac{g^2+g'^2}{4} v^2 Z_{\mu}Z^{\mu} + \frac{g^2+g'^2}{2} v Z_{\mu}Z^{\mu}H + \frac{g^2+g'^2}{4} Z_{\mu}Z^{\mu}H^2 \\ &+ \frac{1}{4} g^2 v^2 W_{\mu}^{+}W^{-\mu} + \frac{1}{2} g^2 v W_{\mu}^{+}W^{-\mu}H + \frac{1}{4} g^2 W_{\mu}^{+}W^{-\mu}H^2 \\ &+ \mu^2 H^2 + \frac{\mu^2}{v} H^3 + \frac{\mu^2}{4v^2} H^4 \end{aligned} \tag{1.26}$$

In this Lagrangian, we can identify the mass terms of the gauge bosons that we were looking for which are of the form $\frac{1}{2}$ mass^2 × field^2. The mass of the $W^{\pm}$ and Z bosons can therefore be deducted from the parameters of the Higgs mechanism :

$$m_W = \frac{1}{2} g v \text{ and } m_Z = \frac{1}{2} v \sqrt{g^2+g'^2} \tag{1.27}$$

The term $\mu^2 H^2$ can be identified as the mass term for the particle associated to the Higgs field : the Higgs boson. Its mass is

$$m_H = \sqrt{2}\mu = \sqrt{2\lambda}v \tag{1.28}$$

The VVH and VVH^2 terms where $V = Z$ or W correspond respectively to the triple and quartic coupling between the massive gauge bosons and the Higgs boson. Finally, the last terms in the Lagrangian only containing H or H^2 correspond to the self-interactions of the Higgs boson. They will be detailed in Subsection 1.2.3.

This Higgs mechanism has therefore enabled the $W^{\pm}$ and Z gauge bosons to be massive like the experience suggests without breaking the local gauge symmetry. A last feature of the SM that needs to be explained is the fermions mass terms that are still missing in the Lagrangian.

The interaction between the Higgs field and the fermions fields is described by this term in the Higgs Lagrangian :

$$y_f(\bar{L}\phi R + \bar{R}\phi^{\dagger} L) \tag{1.29}$$

where y_f is the strength of the coupling for the corresponding fermion f. When the symmetry breaking happens, we plug the expansion around the ground state into the expression of the Lagrangian and we obtain :

$$-\frac{y_f}{\sqrt{2}}v(\bar{L}R + \bar{R}L) - \frac{y_f}{\sqrt{2}}H(\bar{L}R + \bar{R}L) \tag{1.30}$$

Two interactions are described here : the first part has the standard expression of a mass term (for instance in eq. 1.2) and, by identification, the mass of the fermions is found to be

$$m_f = \frac{y_f v}{\sqrt{2}} \tag{1.31}$$

This interaction between the fermions and the Higgs *field* due to its non zero vacuum expectation value v, which gives birth to their mass, is known as the *Yukawa coupling*. The second term represents the interaction between the fermions and the Higgs *boson*. The coupling strength is

$$\frac{y_f}{\sqrt{2}} = \frac{m_f}{v} \tag{1.32}$$

1.2.2 Higgs boson properties and experimental searches

As important for the consistency of the Standard Model as it is, the Higgs boson was not discovered until 2012 when the ATLAS and CMS experiments at LHC announced its observation [23, 24]. The experimental study of the Higgs boson is of crucial importance, firstly to determine if the observed particle does indeed correspond to the one responsible of Electroweak symmetry breaking (EWSB) in the Weinberg-Salam model, and secondly to determine its parameters with precision to look for any inconsistency with the SM prediction.

In this section, we will provide an overview on what's already known on the Higgs boson more than 10 years after its discovery [25, 26] and what remains to be studied, while also stressing out its parameters interesting from an experimental point of view like the way it can be produced at LHC or its main decay channels.

Higgs boson main properties The Higgs boson mass is a free parameter in the Standard Model. The value obtained from statistical combinations of ATLAS and CMS measurements is 125.25 ± 0.17 GeV [27], which is consistent with the electroweak scale.
The Higgs boson has a short predicted lifetime in the SM of $1.56 \cdot 10^{-22}$ s, meaning that it can only be observed through its decay products. The corresponding width is 4.1 MeV which is currently beyond direct experimental reach. Nonetheless, it can be constrained through off-shell H production and the current best measurements from ATLAS [28] and CMS [29] experiments are $4.5^{+3.3}_{-2.5}$ MeV and $3.2^{+2.4}_{-1.7}$ MeV respectively, which is consistent with the SM prediction.
Finally, the Higgs boson is predicted to have spin-parity quantum numbers $J^P = 0^+$. Studying the angular distributions of H decays to leptons and photons [30, 31] allowed to confirm these properties and rule out other spin and parity states at the 99.9% confidence level (CL).

Higgs boson production The Higgs boson can be produced and observed at the LHC using proton-proton collisions. During the collisions, different processes can lead to the production of one or several Higgs bosons, either alone or along other particles (in that case the process is called associated production).

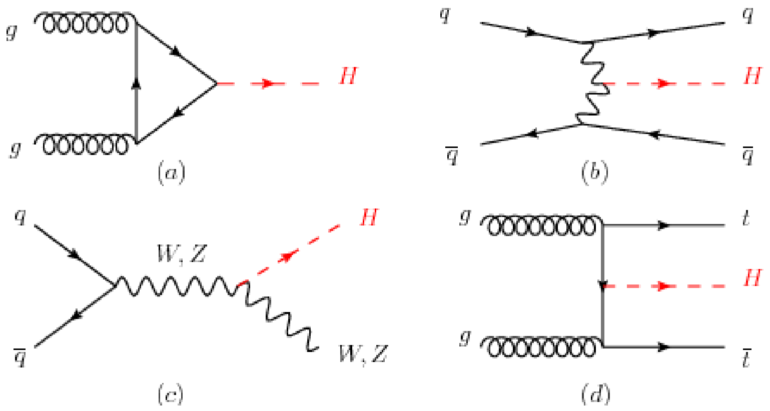

Figure 1.4: Leading order Feynman diagrams representing the main Higgs boson production modes at LHC : ggF (a), VBF (b), VH (c) and ttH (d) [32].

Here is the list of the main ones sorted by decreasing cross section at $\sqrt{s} = 13$ TeV [33]. The associated leading order Feynman diagrams are presented in Figure 1.4 :

- **Gluon-gluon fusion** (ggF or ggH) where gluons from the protons interact to form a triangle of massive virtual particles that will produce a Higgs boson. This is the largest production mode at LHC with a predicted cross section of $\sigma^{H}_{ggF} = 48.5$ pb.
- **Vector boson fusion** (VBF) is the second largest production mode, although its cross section is much lower : $\sigma^{H}_{VBF} = 3.78$ pb. Here, two vector bosons ($W^{\pm}$ or Z) coming from incident quarks fusion to form a single Higgs boson. The experimental signature of this mode are the jets coming from the initial quarks that are only slightly deflected. It is also the best way to access the trilinear coupling between the vector bosons and the Higgs in the Higgs Lagrangian (eq. 1.26).
- **Associated production with a vector boson** (VH), with again $V = W^{\pm}$ or Z, is the third largest production mode. The associated cross section are $\sigma^{WH} = 1.37$ fb and $\sigma^{ZH} = 0.88$ fb. A vector boson is produced from a quark-antiquark fusion and will then radiate a Higgs boson, hence the alternative name 'Higgs-Strahlung'. This mode also allows to probe the trilinear $W/Z\ H$ coupling.
- **Associated production with top quarks** (ttH) allows a direct measurement of the top Yukawa coupling even if the production rate is really low : $\sigma^{ttH} = 0.51$ fb. Another possibility, although rarer, is an associated production with the bottom quark bbH. Even if these processes have a complicated final state, the leptonic decays of the $W^{\pm}$ boson in particular can be used to identify it.

The production cross section of the Higgs boson is also affected by the centre of mass energy of the proton-proton collisions. At the time of discovery during LHC Run 1, the centre of mass energy was $\sqrt{s} = 7$ TeV but was increased to 13 TeV and 13.6 TeV during Run 2 and 3 respectively. The production cross section increases with higher available energy in the collision as illustrated in Figure 1.5, thus allowing the LHC to produce more Higgs bosons in the most recent runs.

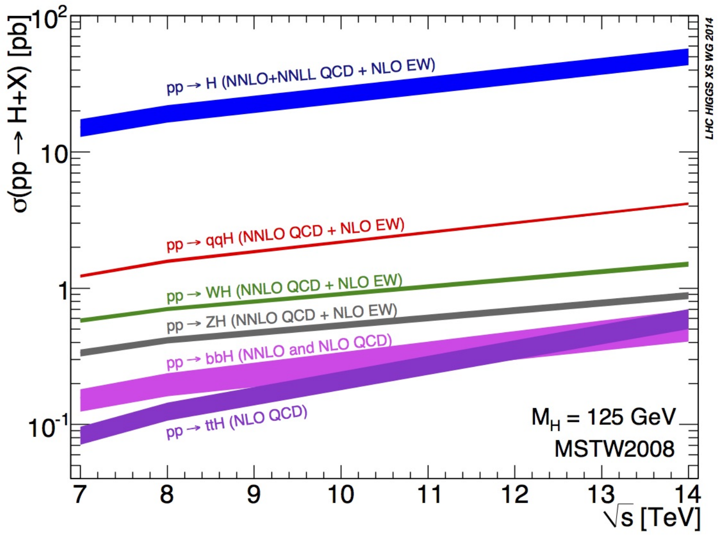

Figure 1.5: Theoretical cross section production of Higgs boson with m_H = 125 GeV as a function of the centre of mass energy $\sqrt{s}$ [33].

Main decay channels The different decay modes and their relative importance can be computed theoretically as a function of the mass of the Higgs boson, thus allowing us to obtain the predicted branching ratios (BR) at the experimentally determined mass (Table 1.2).

Decay channel	Branching ratio (%)
$H \to b\bar{b}$	$58.2^{+0.70}_{-0.76}$
$H \to WW^*$	21.4 ± 0.32
$H \to gg$	8.18 ± 0.42
$H \to \tau^+\tau^-$	6.27 ± 0.10
$H \to c\bar{c}$	$2.89^{+0.16}_{-0.06}$
$H \to ZZ^*$	2.62 ± 0.039
$H \to \gamma\gamma$	0.227 ± 0.0048
$H \to Z\gamma$	0.153 ± 0.0089
$H \to \mu^+\mu^-$	0.0218 ± 0.00037

Table 1.2: Branching ratios of the principal decay modes of the Higgs boson for m_H = 125 GeV [33].

The largest decay channels of the Higgs boson are $b\bar{b}$ and W^+W^-, also written WW^* since one of the W boson is produced offshell because $m_H < 2m_W$. The discovery of the particle in 2012 made use of three particular decay channels that have interesting properties from an experimental point of view.
The first channel used is $H \to ZZ^{(*)} \to 4l$ ($l = e, \mu$), also called the golden channel. Despite its low branching ratio of $1.24 \cdot 10^{-4}$, it has a really high signal over noise ratio.

The second channel $H \to \gamma\gamma$ has an even lower branching ratio (0.23%) but the process benefits from the excellent mass resolution of the photons in the detector. As the photons are massless, the decay involve a loop of virtual massive particles, explaining the small BR. These two channels are also useful to provide precision measurements, for instance on the Higgs boson mass [34]. On the contrary, $H \to WW^*$ was also used to exploit its large branching ratio.
The analysis on these channels were combined by the CMS and ATLAS experiments to announce the discovery of a new particle compatible with the SM Higgs boson in 2012 [23, 24]. The discovery plots of the ATLAS Collaboration, which can be said to be of historical importance, are presented in Figure 1.6.

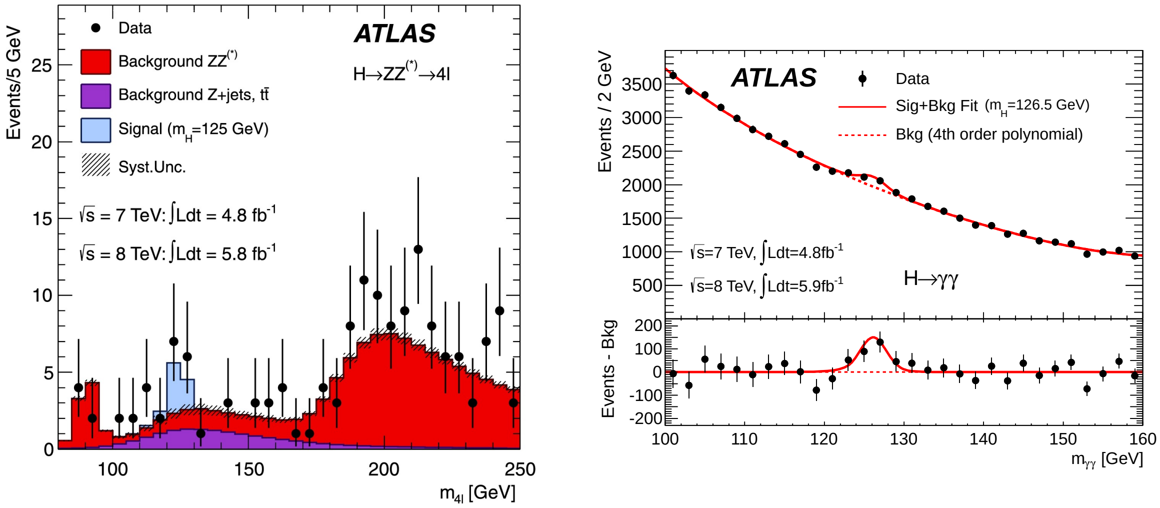

Figure 1.6: Discovery plots of the Higgs boson by the ATLAS Collaboration. It represents the four leptons (left) and two photons (right) invariant masses where an excess coming from the Higgs particle can be observed [23].

Coupling strengths Observing the different Higgs boson decays is interesting not only from an experimental point of view but also because it allows to check the consistency of its couplings with the elementary particles.

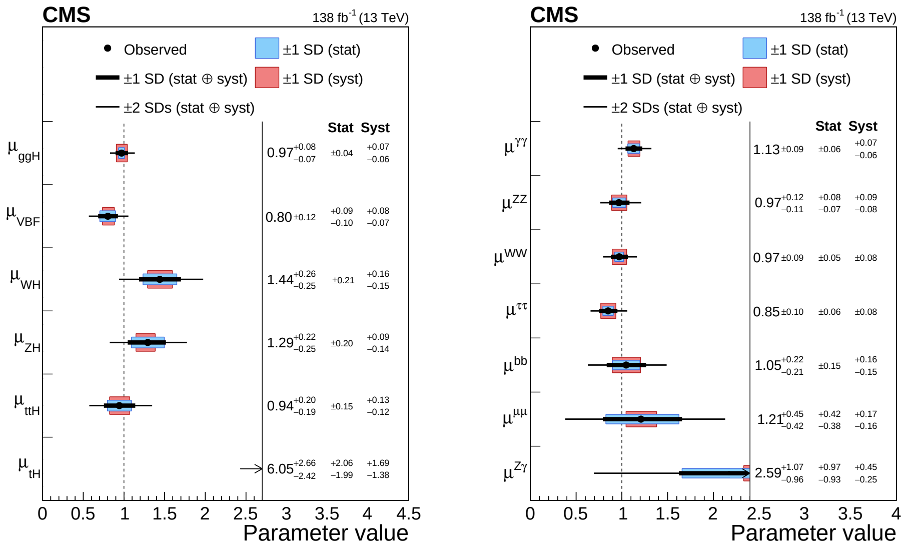

Figure 1.7: Signal-strength parameters measured by the CMS experiment for various production modes μ_i (left) and decay channels μ^f (right) [25].

The ATLAS and CMS experiments have observed individually a substantial number of decays, starting with the most common $H \rightarrow b\bar{b}$ [35, 36], $H \rightarrow WW^{(*)}$ [37] or $H \rightarrow \tau^+\tau^-$ [38, 39]. The consistency of the decay rates with respect to the Standard Model prediction can be characterised by the signal strength μ which is the ratio between the measured cross section to the SM value. For now, the observed values μ for all decays are compatible with 1 which means that the measured branching ratios are compatible with the SM. This result is summed-up in Figure 1.7, along with the production modes of the Higgs which are also compatible with the predicted rates at, for instance, $\sqrt{s} = 13$ TeV. The decay rates of the Higgs boson can be used to probe the Yukawa couplings with other elementary particles. The couplings with 3$^{\text{rd}}$ generation fermions and the W and Z bosons have already been measured by the ATLAS and CMS experiments with various precision levels. Some limits have also been put on the ones with two 2$^{\text{nd}}$ generation fermions, the muon and the c quark. As expected, the couplings are proportional to the mass of the particles (Figure 1.8) which is a wonderful check of the validity of the Higgs mechanism prediction over three order of magnitudes. It is interesting to note that these results went above what was expected during the conception of the LHC as, for example, the muon or c quark decay channels where believed to have too much background and a too low production rate to put constraints on them.

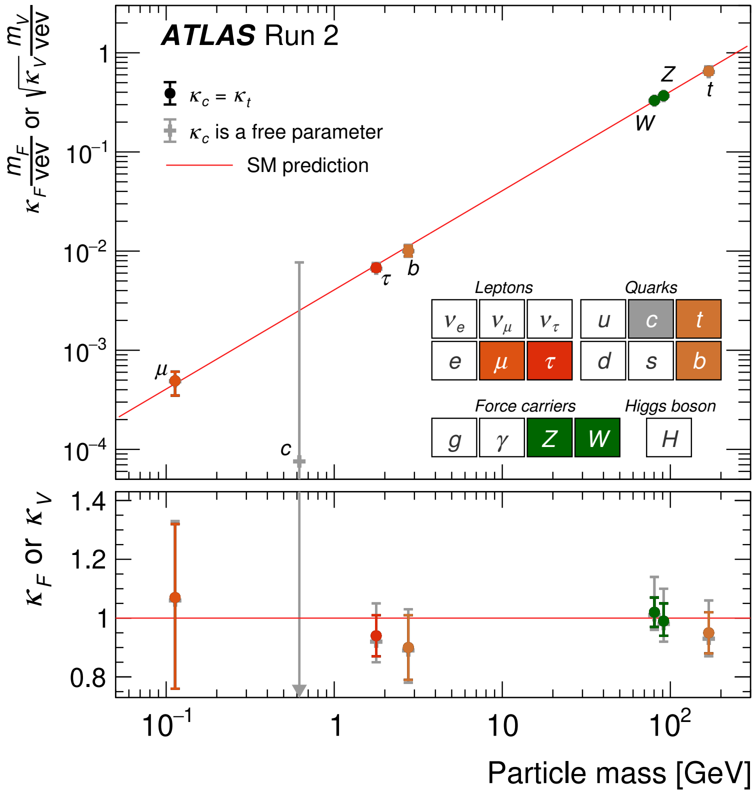

Figure 1.8: Reduced coupling between the Higgs boson and elementary fermions and bosons as a function of their mass. The ratio with SM prediction is shown in the bottom panel [40].

Similarly to what is done with the different signal strength μ values, the κ-framework is used to regroup the so-called *coupling modifiers* of the Higgs couplings [41]. For each coupling, the scaling factor κ is defined by the ratio between the measured value of the coupling and the SM predicted one, assuming all the other couplings are equal to their SM value. It allows to take into account the correlations between the coupling values and check for Beyond Standard Model (BSM) enhancement or reduction of processes. Lastly, another important coupling to probe is the Higgs boson coupling with itself. It is the main subject of the next subsection.

1.2.3 Higgs self-coupling and Higgs boson pair production

Recalling the expression of the Higgs Lagrangian in Equation 1.26 which made appear additional terms of interactions between the Higgs boson itself :

$$V(H) = \mu^2 H^2 + \frac{\mu^2}{v} H^3 + \frac{\mu^2}{4v^2} H^4 \tag{1.33}$$

It can be written in terms of the Higgs potential parameters :

$$V(H) = \lambda v^2 H^2 + \lambda v H^3 + \frac{1}{4}\lambda H^4 \tag{1.34}$$

where

$$\lambda = \frac{m_H^2}{2v^2} \tag{1.35}$$

λ, sometimes written λ_{HHH}, is the trilinear Higgs self-coupling [42]. Its value is of crucial importance as it controls the shape of the Higgs potential. The Mexican hat shape from Figure 1.3 is actually only the simplest form for the additional potential to account for the Higgs mechanism but more complex forms are also possible. In an extreme case if λ is negative, the current vaccum state in which the Universe is set could be a metastable state.

As seen in Equation 1.35, the SM value of λ is linked to the Higgs mass and the vacuum expectation value v. Its current indirect measurement with single Higgs production is around $\lambda_{SM} = 0.13$. However, the only direct way to measure Higgs self-coupling is through Higgs boson pair production (or di-Higgs).

The drawback of HH is that it has a really small production cross section at the current LHC energies, almost 2000 times lower than single Higgs. As such, di-Higgs has not been observed yet and for now the measurements have only been able to set upper limits to its cross section. Nevertheless, observing the process is something that is reachable with the expected full dataset of the HL-LHC and is indeed one of the major objectives of the upgrade of the LHC.

Main production modes of HH Similarly to single Higgs, a pair of Higgs boson can be produced in various ways at the LHC. The production modes of di-Higgs are closely linked to which couplings are accessible when measuring the corresponding production mode. They are presented with decreasing cross section :

- **Gluon-gluon fusion** (ggF) is by far the dominant production mode with a cross section of $\sigma_{ggF}^{HH} = 31.1^{+2.1}_{-7.2}$ fb at $\sqrt{s} = 13$ TeV [43]. The two leading order Feynman diagrams involved in the process (Figure 1.9) are called the 'box' and the 'triangle' diagram depending on the form of the intermediate massive top quark loop. The two diagrams interfere destructively which explains the really small production rate of di-Higgs compared to single Higgs. The 'box' diagram is sensitive to the Higgs-top quark coupling λ_t whereas the 'triangle' one is sensitive to the Higgs self-coupling λ.

- **Vector Boson Fusion** (VBF) is the second most important contribution to the Higgs boson pair production but its cross section is much smaller than ggF : $\sigma_{VBF}^{HH} = 1.73 \pm 0.004$ fb [43]. However, it provides sensibility to trilinear c_V and quadrilinear c_{2V} couplings between the Higgs and the vector bosons as illustrated in Figure 1.10.

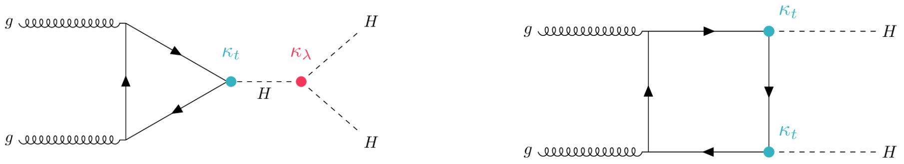

Figure 1.9: Leading order Feynman diagrams of the dominant gluon–gluon fusion production process for di-Higgs. The 'triangle' diagram (left) can probe the Higgs trilinear coupling modifier $\kappa_\lambda = \lambda/\lambda_{SM}$ whereas the 'box' diagram (right) is affected by the Higgs-top Yukawa coupling modifier κ_t [42].

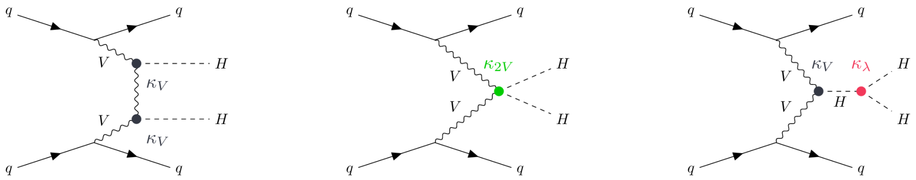

Figure 1.10: Leading order Feynman diagrams of the vector boson fusion production process for di-Higgs. The right diagram is sensitive to the Higgs self-coupling and the other two diagrams can probe the VVH and $VVHH$ vertices [42].

Finally, the other di-Higgs production modes such as VHH, $ttHH$ or $tjHH$ account for less than 5% of the total production in total.

The predicted production rate of di-Higgs could vary if some BSM scenarios are true. Such a change can be quantified by the Higgs self-coupling modifier $\kappa_\lambda = \lambda/\lambda_{SM}$. The theoretical dependency of di-Higgs cross section to κ_λ is illustrated by the red line in Figure 1.13. The box and triangle diagram interference can cause the cross section to be smaller than the SM one even if the Higgs self-coupling is larger than its predicted value. On the other hand, some values of κ_λ predict an improved HH production rate. That's why the process is closely looked at, as an early detection could be a clear sign of new physics since the SM process is not expected to be discovered before HL-LHC. The search for BSM processes will be detailed in section 1.3.

Di-Higgs decay channels The decay channels of a pair Higgs boson pairs can be simply deduced from the single Higgs decay modes (see Figure 1.11). Compared to single-Higgs, the global small production rate of the process imposes several constraints and encourages experimental researches to use at least one $H \to b\bar{b}$ decay to benefit from its large branching ratio.

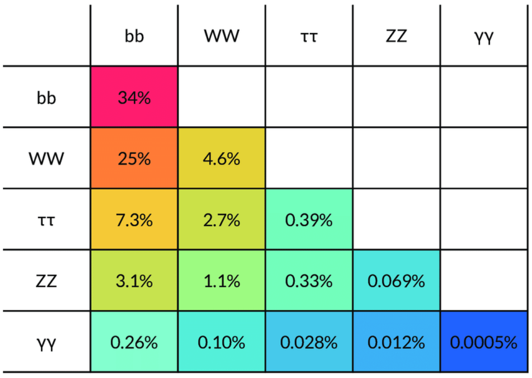

	bb	WW	ττ	ZZ	γγ
bb	34%				
WW	25%	4.6%			
ττ	7.3%	2.7%	0.39%		
ZZ	3.1%	1.1%	0.33%	0.069%	
γγ	0.26%	0.10%	0.028%	0.012%	0.0005%

Figure 1.11: Branching ratios of the decay modes of SM HH depending on the decay of each of the Higgs boson (Image credit : K.Leney [44]).

.

$b\bar{b}b\bar{b}$ is the most common process but nevertheless only represents 34% of the final states. It also suffers from a really large multijet background. $b\bar{b}\tau\tau$ offers a good compromise between a sizeable cross section (7.3%) and a relatively small background mainly composed of $t\bar{t}$ and $Z \to \tau^+\tau^-$ events. The hadronic, leptonic and semi-leptonic decays of the τ lepton are studied seprately and then combined.
Finally, the $b\bar{b}\gamma\gamma$ channel, which will be the main channel used in this thesis, benefits from a low background and an excellent trigger and photon reconstruction efficiency leading to a very good $\gamma\gamma$ mass resolution. The drawback is the really small branching ratio (0.26%) which means that only 12 $HH \to b\bar{b}\gamma\gamma$ events have been produced during LHC Run 2.

Experimental searches for HH at LHC The ATLAS and CMS experiments have searched for HH production in various final states. ATLAS have published analyses using the entirety of LHC Run 2 data (collected between 2015 and 2018) for the three main channels $b\bar{b}\gamma\gamma$ [42], $b\bar{b}b\bar{b}$ [45] and $b\bar{b}\tau\tau$ [46]. Previous researches, using either Run 1 or partial Run 2 data, have also probed other final states involving W bosons like WW^*WW^* [47], $b\bar{b}WW^*$ [48] or $\gamma\gamma WW^*$ [49] to exploit the 20% branching ratio of the $H \to WW^*$ decay but these analyses suffer from the large $t\bar{t}$ background. Finally, the very recent multileptons [50] and $b\bar{b}ll + E_T^{\text{miss}}$ [51] researches performed with the full Run 2 dataset use transversal final states that can probe various decay channels at once. The different channels can then be combined [52, 53] to obtain an overall limit on the HH production rate, as illustrated in Figure 1.12. As no signal is found, upper limits are set on the cross section and HH signal strength μ_{HH}. The observed 95% CL upper limit of μ_{HH} is 2.9 (2.4 expected).

This measurement is used to put constraints on the Higgs self-coupling modifying factor κ_λ as seen in Figure 1.13 and on the Higgs quartic interaction with vector bosons $HHVV$ κ_{2V}. The combined 95% CL observed (expected) constraints are $-1.2 < \kappa_\lambda < 7.2\,(-1.6 < \kappa_\lambda < 7.2)$ and $0.6 < \kappa_{2V} < 1.5\,(\,0.4 < \kappa_{2V} < 1.6)$ [53]. They are the best constraints on κ_λ thanks to the five channel combination. As

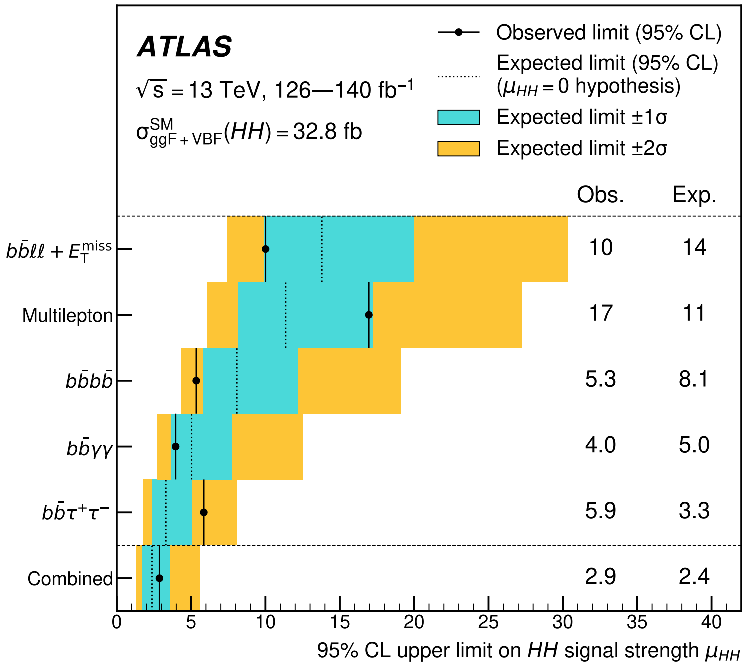

Figure 1.12: Observed and expected 95% CL upper limits on the signal strength for the inclusive ggF and VBF di-Higgs production from the $4b$, $b\bar{b}\tau^+\tau^-$, $b\bar{b}\gamma\gamma$, multilepton and $b\bar{b}ll+E_T^{\text{miss}}$ decay channels and their statistical combination performed by ATLAS [53].

indicated previously, single Higgs measurements sensitive to these couplings at the next-to-leading order can be combined with the HH ones to put further constraints on them [52].

The CMS experiment also performed a research of a pair of Higgs bosons with the $b\bar{b}b\bar{b}$, $b\bar{b}\tau^+\tau^-$, $b\bar{b}\gamma\gamma$, $b\bar{b}ZZ$ and multilepton final states and their combination [25] and the observed (expected) final constraints on μ_{HH} is 3.4 (2.5), which is the same order of magnitude as ATLAS.

It appears that no HH signal has been observed, which means that no BSM process has been found to increase the production rate of this process yet. However, a deviation from the predicted SM cross section of HH is not the only way for BSM physics to be involved here. A large number of the HH searches described here also looked for a resonant production of the HH process i.e an intermediate particle X that would decay to a pair of Higgs bosons. Beyond Standard Model physics and its research in the $b\bar{b}\gamma\gamma$ final state will be the subject of the next section.

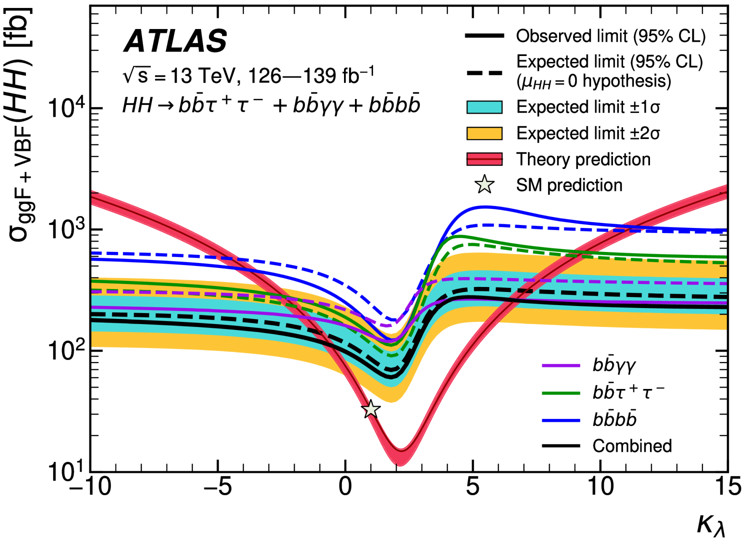

Figure 1.13: Observed and expected 95% CL exclusion limits set by ATLAS on the production cross section of the combined ggF and VBF HH processes as a function of κ_λ. The red line show the theory prediction where all parameters and couplings are set to their SM values except for κ_λ [52].

1.3 Beyond standard model physics and the search for new scalar bosons

The Higgs boson is crucial in the current particle physics landscape because it represents at the same time an accomplishment for the Standard Model and an opportunity to test it and provide new insights on the possible physics beyond it. In this section, the limits of the Standard Model will be presented first. This will be followed by a brief overview of some Beyond Standard Model (BSM) theories that intend to fix some of the SM shortcomings. Lastly, the experimental characteristics of additional scalar bosons predicted by BSM models and which are the subject of the analysis presented in Chapter 4 will be discussed.

1.3.1 The limits of the Standard Model

The predictive power of the Standard Model has been thoroughly tested with high precision for a large number of processes and at different energies. However, as briefly mentioned earlier, the SM suffers from limitations in the sense that it does not provide a satisfying explanation for some important physics phenomena. This includes :

- **Neutrino oscillation** constituted the first experimental results not predicted by the SM. The phenomenon was observed in 1998 by the Super-Kamiokande experiment [54] which noticed a deficit in atmospheric muon neutrino flux. This deficit pointed out that the neutrinos were oscillating between flavours, a feature that requires them to be massive. The SM considers the neutrino to be massless (as seen in Section 1.2), yet the neutrino mass can be added without breaking the SM gauge invariance principles.

- **Gravitation**, the 4th fundamental interaction in nature is not described by the Standard Model. Even though gravitation is by far the weakest force in terms of coupling, it governs the dynamics of the Universe at the astronomical scale. The current theory used to describe it is the General Relativity and unsuccessful attempts have been made to incorporate it to the Standard Model. The research of a theory encompassing both the Standard Model and gravity to form a so-called 'Theory of everything' is considered to be one of the greatest challenge of modern physics.

- **Dark matter** consists of hypothetical particles introduced to explain the astrophysical observation that the galaxies are heavier than they appear. The rotation curves of the galaxies are indeed rather flat as opposed to the Newtonian decrease they should obey according to the observed mass of the stars in the galaxies [55, 56]. The dark matter could account for this invisible mass by forming halos surrounding the galaxies. However the Standard Model does not provide any massive particle that could play the role of dark matter. Such a particle would be massive, stable, and interact extremely weakly with the 'ordinary' matter. To tackle this issue, a large number of BSM models are including in their prediction additional particles that could be dark matter candidates.

- **The asymmetry between matter and anti-matter** is not explained by the SM. A charge - parity (CP) symmetry violation term is included in it but is currently estimated to be too low to meet the Sakharov conditions [57]. They are the conditions required to explain why our Universe is made of baryons and not an equal number of baryons and anti-baryons.

- **The hierarchy problem** comes from the virtual particles loop corrections that are applied to the Higgs boson mass. These corrections need to be cancelled to avoid divergences, which is done in a renormalisable theory such as the SM by defining a cut-off value Λ above which the additional terms from the virtual particles are 0. The problem arises because the cut-off value needs to be really precisely determined to cancel the loop corrections of the Higgs boson mass. This can be considered as 'fine-tuning' and the sign that the SM is only a low energy approximation of a more global description of physics.

- Finally, some **tensions in SM precision tests** arose in the last years. For instance, the measurement of the magnetic moment of the muon [58] is slightly different than the SM prediction [59], even if alternative theory computations could lead to a smaller discrepancy [60]. The mass of the W boson, which is quite constrained by other experimental values such as the top quark or the Higgs boson mass, was found to be higher than expected in a measurement from the CDF experiment at

Fermilab [61]. Other measurements [62, 63] and the experimental average are staying in line with the theory prediction nonetheless.
Lastly, the $R(D)$ and $R(D^*)$ values measured by the LHCb experiment, which are the ratio between B^0 mesons decaying into D or D^* mesons together with τ or μ leptons and their corresponding neutrinos, differ by 3.3 standard deviation from the SM prediction [64]. This could possibly hint to lepton flavour universality (LFU) violation or the existence of hypothetical particles named leptoquarks mediating the $b \to cl\bar{\nu}$ ($l = \mu, \tau$) transitions in addition to the SM processes.

All these limitations motivate the development of theoretical models which intend to address the SM problems, or at least a part of them. They are the subject of the next section.

1.3.2 Example of BSM models predicting additional scalar bosons

Theories extending the Standard Model are based on the addition of new terms in the SM Lagrangian. They are often motivated by mathematical considerations such as additional symmetries since this approach worked well for the establishment of the SM. They all have the constraint to keep the SM as a low energy limit because of its a remarkable predicting power in the current accessible energy range.
A popular example is Supersymmetry (SUSY) which is a family of BSM models that assume the existence of an additional symmetry under which every particle in the SM has a supersymmetric partner with a different spin (super-partners of fermions are bosons and vice versa). This symmetry should be broken at the SM energy scale to take into account that the SM super-partners, which should have the same mass, have not been discovered yet. There are a large number of SUSY models depending on how this symmetry is broken and they all present the advantage to tackle the hierarchy problem by cancelling the particle loops divergences with the contributions from the super-partners. SUSY predicts the union of the coupling constants of the different interactions at high energy and provides a dark-matter candidate as the lightest supersymmetric particle would be stable. SUSY also has some consistency problems in itself, such as the "μ problem" which arises because of the supersymmetric Higgs mass μ which should naturally be at the Planck energy scale level but appears to be at the electroweak scale to provide correct mass terms. As we will see, some SUSY models provide an explanation for the naturalness of this parameter.
The Higgs sector, a term regrouping all the particles involved in the Higgs mechanism, is often extended by new particles in BSM models, whether alone or in addition to supersymmetry. The BEH mechanism is actually only one of the simplest way to provide mass to the electroweak bosons and the fermions but not the unique solution. Modifications to the Higgs sector range from alternative expressions of the Higgs potential to the prediction of additional real or complex fields. These fields could lead to the existence of additional physical states bosons, with the constraint that one of them must correspond

to the already observed SM-like Higgs boson.

The extension of the Higgs sector can provide an explanation for some shortcomings of the SM, for instance by adding CP violating terms in the Lagrangian. These additional terms can also break some "accidental" symmetries of the SM like Flavour Changing Neutral Currents that could violate baryon and lepton number conservation. In that case, the associated couplings must be suppressed to recall for its apparent conservation at the SM energy scale.

To cope with the variety of BSM models which predict a broad spectrum of decay channels for additional particles, *benchmark frameworks* are used to provide a phenomenology typically representative of a specific model. This allows to design analysis sensitive to several models and exclude values of coupling parameters if the observed limits exceed the predicted cross sections.

The following (non-exhaustive) list sums up and briefly presents some of the most common BSM models predicting additional scalar bosons that could be observed at LHC and ATLAS. The current status of searches for experimental evidence of these models is presented in Subsection 1.3.3.

Minimal Supersymmetric Standard Model The Minimal Supersymmetric Standard Model (**MSSM**) [65] is the simplest realistic model allowed by SUSY. It has a very large number of free parameters (105) which reflects our ignorance on how the supersymmetry is broken. The MSSM Higgs sector is composed of two Higgs doublet ϕ_1 and ϕ_2. After the spontaneous symmetry breaking, this results in 5 physical particles : one charged Higgs pair $H^{\pm}$, one CP-odd neutral scalar A and two CP-even neutral states H and h [3]. It depends on only two free parameters which are usually taken as the ratio between the vacuum expectation values of the Higgs doublets $\tan\beta = v_1/v_2$ and the mass of one of the neutral Higgs boson, conventionally the CP-odd one m_A.

To cope with the vast possibility of couplings and decay channels with the new predicted particles, latest analyses suggest six benchmarks scenarios for studying them at LHC [66]. In some cases like the M_h^{125} and $M_h^{125}(\tilde{\chi})$ scenarios, the heavy CP-even Higgs bosons H could decay into a pair of the SM-like h. A search for this process with resonant pair production in SM Higgs boson is presented in the next subsection.

Next-to-Mininal Supersymmetric Standard Model The Next-to-Mininal Supersymmetric Standard Model (**NMSSM**) [5, 67] relies on two Higgs doublets fields like the MSSN but adds an electroweak singlet superfield N.

The superfield allows to tackle the μ problem of the MSSM as its value naturally arises as the vacuum expectation value of N. The Higgs sector has then two additional degrees of freedom which result in seven 'Higgs particles' : three CP-even H, h and h_S, two CP-odd A ans A_S and two charged Higgs $H^{\pm}$. Similarly to MSSM, benchmark scenarios are used to characterize the different observations that could be made at LHC in function of typical parameters of the model [33]. The NMSSM has the particularity to allow chain

---

[3] Here the observed SM Higgs boson would be h. It will be written this way in all this subsection.

Higgs-to-Higgs decays which could take the form of either symmetric ($H \to hh$ or $h_S h_S$) or asymmetric ($H \to hh_S$ and $A \to A_S h_S$ or $A_S h$) decays.

Two-Higgs-Doublet Model The Two-Higgs-Doublet Model (**2HDM**) [4, 68] consists, as its name suggests, in the addition of a second Higgs doublet to the Higgs sector. The 2HDM is not a SUSY theory which opens more possibility for the couplings between Higgs bosons and fermions but nevertheless its Higgs sector has the same structure as the MSSN one.
There are four types of 2HDM models depending on the considered coupling of the Higgs doublets to fermions. After the symmetry breaking, the doublets result in five Higgs bosons which are composed of two CP-even scalars H and h, a neutral CP-odd A and two charged bosons $H^{\pm}$. The decay $H \to hh$ could be allowed if $m_H > 2m_h$ and be observed as a resonance in the di-Higgs production. An interesting feature of the 2HDM is that it can allow CP violation in the Higgs sector, therefore providing a solution to the matter-antimatter asymmetry.
Another possibility is to further extend the 2HDM Higgs sector with either a real scalar singlet (N2HDM) [69] or a complex singlet (2HDM+S) [70] . The additional singlet would mix with the doublet of the Higgs sector and allow for asymmetrical Higgs decay.

Two-Real-Scalar-Singlet The Two-Real-Scalar-Singlet model (**TRSM**) [71] extends the Standard Model with two real scalar singlets. After symmetry breaking, the scalar singlet fields are mixed to form three mass eigenstates which would be three CP-even bosons. The model has seven free parameters which are the masses of the new bosons, the mixing angles and the two new vacuum expectation values of the singlets.
Similarly to NMSSM, benchmark scenarios are proposed by theorists to facilitate the experimental study at LHC. All of them predict Higgs to Higgs decays from the heaviest one to the lightest ones, either symmetrically or asymmetrically. In benchmark points 2 and 3 from [71] in particular, the observed Higgs boson h is found to be one of the two lightest additional bosons, meaning that its experimental signature could be used.

Other models also account for additional heavy bosons that are not part of the Higgs sector, such as the Randall–Sundrum bulk model where radion and graviton (which is spin 2) would be observable excited modes of the gravitational field [6, 72].
Finally, another different approach to BSM physics consists in using Effective Field Theories (EFTs). As the Standard Model is supposed to be a low energy approximation of a more complex theory, the effects of BSM physics which are supposed to happen at a high energy are parameterised in terms of effective couplings at low-energy in EFTs. This approach can be used for instance to interpret the results of the di-Higgs analyses in terms of constraints on additional effective coupling constants [73].

1.3.3 Experimental signature of additional scalar bosons

In the context of this thesis, the search for additional scalar bosons can take the form of a research of a heavy scalar resonance, written X, that can decay either symmetrically to a pair of SM Higgs boson H, or asymmetrically to H and a lighter scalar S.

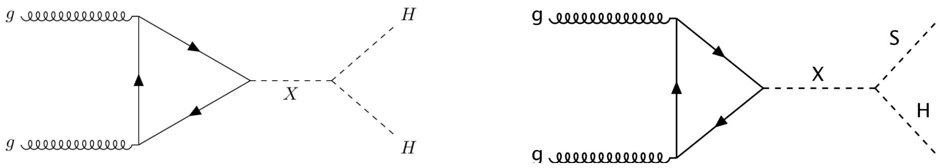

Figure 1.14: Feynman diagram of the gluon-gluon fusion production of a heavy scalar resonance X decaying symmetrically into a Higgs boson pair (left) [74] or asymmetrically into the Higgs boson and another scalar boson S (right) [9].

The heavy resonance could be produced at the LHC via gluon-gluon fusion similarly to the SM Higgs boson as illustrated in Figure 1.14. The narrow width approximation, which states that the width Γ_X of the massive scalar X is negligible with respect to its mass, can be assumed to simplify the signal form. It was notably checked to be true with the TRSM model where the ratio Γ_X/m_X doesn't exceed 1.1%. However this assumption is not always true as Higgs-like bosons widths tend to increase quickly with the mass as shown in Figure 1.17.

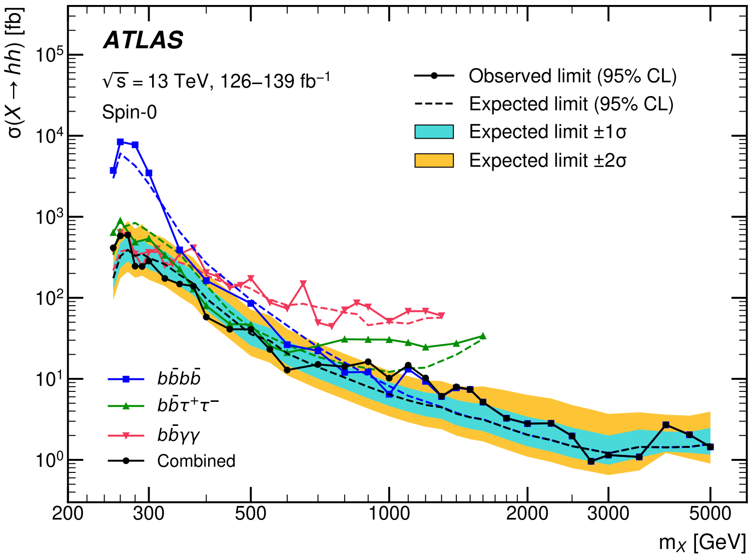

Figure 1.15: Observed and expected upper limits at the 95% CL on the resonant Higgs boson pair production cross section as a function of the resonance mass m_X. Here h is the SM Higgs boson [75].

Resonant HH production The CMS [76] and ATLAS [75] experiments performed a search of a resonant di-Higgs pair production. The analysis make use of the different decay channels of the HH pair. Considering only the three main ones, at high mass, the $b\bar{b}b\bar{b}$ final state provides the best constraints while $b\bar{b}\tau^+\tau^-$ performs well for intermediate values of m_X. Finally the $b\bar{b}\gamma\gamma$ channel has the best sensitivity in the low mass region thanks to its high trigger and reconstruction efficiencies for photons. The overall sensitivity increases with m_X.
The limits set by, for instance, the ATLAS experiment are illustrated in Figure 1.15. They can be interpreted by some of the models described in the previous section to constrain their space parameters. Figure 1.16 presents the interpretation with the MSSM in the two benchmark scenarios M_h^{125} and $M_h^{125}(\tilde{\chi})$.

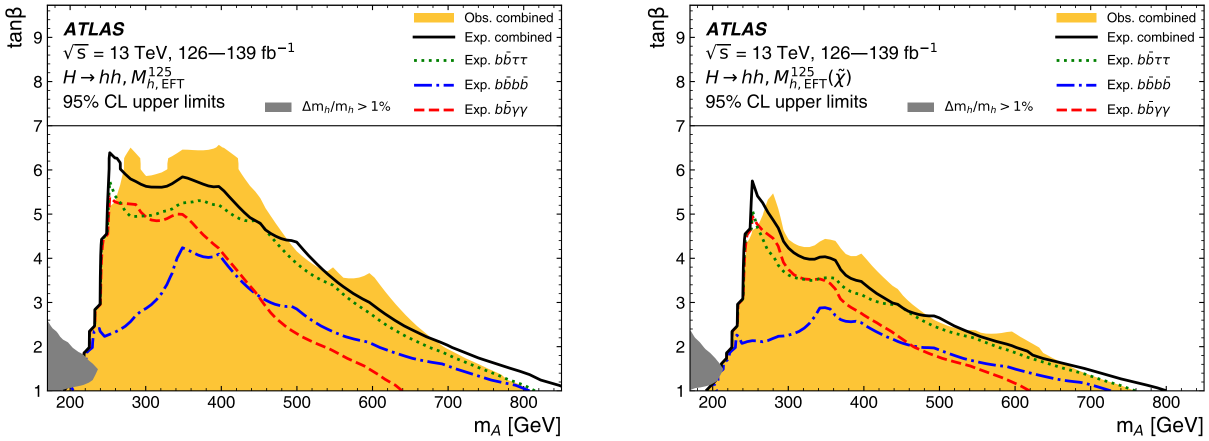

(a)

(b)

Figure 1.16: Observed and expected exclusion limits at the 95% CL on the MSSM parameter space for the (left) $M_{h,EFT}^{125}$ and (right) $M_{h,EFT}^{125}(\tilde{\chi})$ benchmark scenarios for each of the individual channels and their combination. The dark shaded regions are excluded from the search because a mass of 125 GeV would be excluded for h with these $\tan\beta$ and m_A values [75].

Resonant SH production The predicted production rate of the scalar resonance X and the different decay modes allowed for the S particle are strongly depending on the considered theoretical model. However, according to Figure 1.17, if S has Higgs boson Standard Model-like features, it will decay most of the times into a $b\bar{b}$ pair if its mass is lower than 150 GeV, furthermore motivating the search for S in the $S \to b\bar{b}$ decay mode at low m_S. At higher mass, however, the favoured decay modes will be WW^*, $t\bar{t}$ and ZZ^*. The $b\bar{b}\gamma\gamma$ channel has been checked to be very competitive with appropriate benchmark points of the TRSM model.

Similarly to the resonant di-Higgs production, the CMS and ATLAS experiments

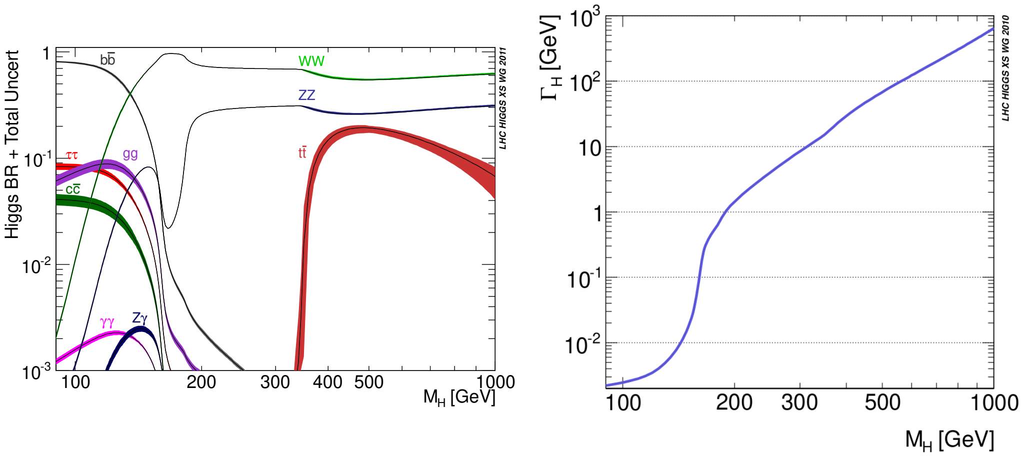

Figure 1.17: Theoretical properties of the SM Higgs boson as a function of its mass m_H : decays branching ratio (left) and width (right) [77].

made several analyses to search for the $X \rightarrow SH$ process. In particular, ATLAS probed the $X \rightarrow S(VV)H(\tau\tau)$ (with V being either a W or Z boson) decay mode [78] while CMS looked at the $X \rightarrow S(b\bar{b})H(b\bar{b})$ [7], $X \rightarrow S(b\bar{b})H(\tau^+\tau^-)$ [8] and $X \rightarrow S(b\bar{b})H(\gamma\gamma)$ [6] channels.

A small excess with respect to the background-only scenario was reported in the latter analysis with a local (global) significance of 3.8 (less than 2.8) standard deviation at (m_X, m_S) = (650, 90) GeV as shown in Figure 1.18.

The results can be interpreted with models predicting an asymmetric Higgs to Higgs decay like the NMSSM. Theory computations [79, 80] can give the maximum cross sections allowed for those processes. Comparing these values with the observed limits on the $X \rightarrow SH$ production rate allows to discard some values of m_X and m_S if the limits are lower than the predicted cross section as illustrated in Figure 1.19.

To conclude, the excess in the $b\bar{b}\gamma\gamma$ channel therefore adds extra motivation to the search of these two scalar bosons. The analysis looking for the $X \rightarrow SH \rightarrow b\bar{b}\gamma\gamma$ process with the ATLAS detector full Run 2 dataset will be covered in Chapter 4.

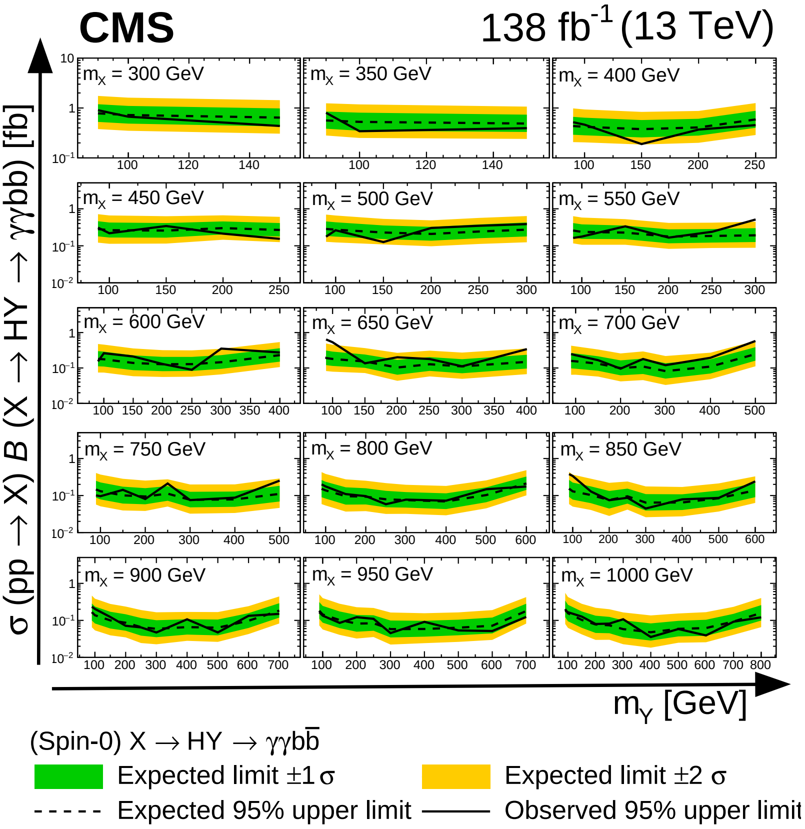

Figure 1.18: Expected and observed 95% CL exclusion limit on production cross section of the $pp \to X \to HY \to b\bar{b}\gamma\gamma$ signal obtained by the CMS experiment. The dashed and solid black lines represent expected and observed limits respectively. The green and yellow bands represent the ±1 and ±2 standard deviations for the expected limit. The middle plot in the 3rd row shows the highest excess observed for m_X = 650 GeV and m_Y = 90 GeV [6].

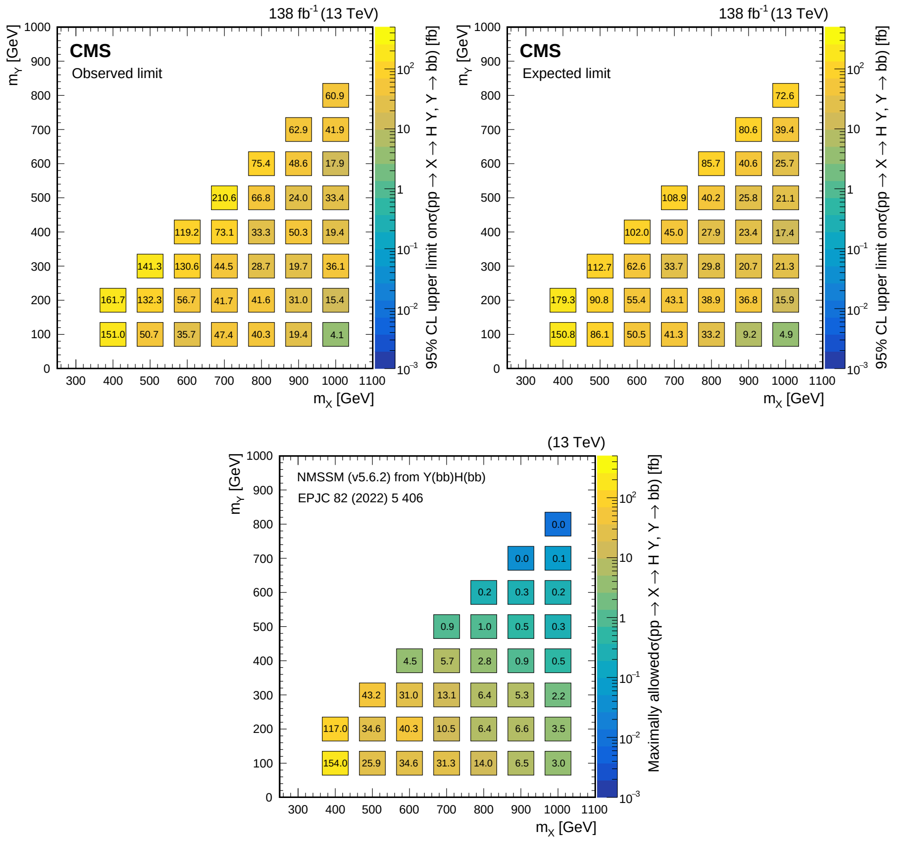

Figure 1.19: Observed (top left) and expected (top right) upper limits at 95% CL on the product of the X production cross section σ and the branching fraction of the $X \to Y(b\bar{b})H$ decay $\mathscr{B}$ [76]. Limits are obtained by combining the $b\bar{b}b\bar{b}$ [7], $b\bar{b}\tau^+\tau^-$ [8] and $b\bar{b}\gamma\gamma$ [6] channels. The corresponding maximally allowed values of $\sigma\mathscr{B}$ in the NMSSM computed with [79] are also shown for comparison (bottom).

2 The ATLAS experiment at LHC

Table of contents

The theories detailed in the previous chapter to describe elementary particles must of course be confronted to experiment. The Large Hadron Collider (LHC) which is the largest particle accelerator in the world is the ideal experimental infrastructure to probe the Standard Model and beyond. The ATLAS experiment, situated on the LHC, is a multipurpose detector that is meant to explore the energy frontier and specifically study Higgs boson physics.

In this chapter, general information about the LHC is first given in Section 2.1. The ATLAS detector, which is the major object of this thesis, is then described in more details in Section 2.2, and the particle reconstruction in Section 2.3. Finally, the upgraded version of ATLAS and the associated tracking performance is depicted in Section 2.4.

2.1 The Large Hadron Collider

The Large Hadron Collider (LHC) [81] is the world's current largest and highest energy particle accelerator. It is situated at CERN, between the France-Switzerland border and consists in a circular ring of 27 km in circumference that allows proton-proton collisions up to a centre-of-mass energy of 13.6 TeV.

The LHC falls within the long history of particle accelerators and cutting-edge research at CERN. CERN (which stands for *European Organization for Nuclear Research* - the CERN acronym comes for its previous name in french) is an international organization that was established in 1954 to regroup the european research on nuclear and particle physics and to broadly coordinate efforts in high energy physics of laboratories and universities from all over the world. As previously mentioned, it took an important place in the establishment of the Standard Model with for example the discovery of weak interaction neutral currents in 1973, W and Z bosons in 1983 or more recently the Higgs boson in 2012. These discoveries have been made possible by the large instrumental facilities that were built at CERN. Different particle accelerators were constructed throughout the years like the Linac in 1959, the Proton and the Super Proton Synchrontron (PS and SPS) in 1960 and 1971 and the Large Electron Positron collider (LEP) in 1989.
A lot of those accelerators are still running today as the PS, SPS and Linac are used as protons injectors to the LHC and other experiments. They form an impressive complex of accelerators, as seen in Figure 2.2. The LHC also uses the same tunnel as the LEP which was running between 1989 and 2000.

The LHC has started to run in 2008 and underwent different phases throughout its operation : data-taking periods (named Runs) are alternating with Long Shutdowns where maintenance and accelerators and detectors upgrade are taking place. Run 1 took place between 2008 and 2013 with proton-proton collisions at a centre of mass energy of 7 and 8 TeV, followed by Run 2 from 2015 to 2018 with collisions at 13 TeV. We are currently in the Run 3 data taking period with interactions at $\sqrt{s} = 13.6$ TeV which started in July 2022 and should last until 2025. The luminosity have also been increased between the Runs. A phase of operation named High Luminosity LHC (HL-HLC) with large improvements is planned for 2029. Upgrades for HL-LHC, notably for the ATLAS detector are the subject of Section 2.4. The previous and future planned operation schedule of the LHC is summed-up in Figure 2.1. The LHC could therefore remain in service until the 2040s. After that, new larger accelerators like the Future Circular Collider (FCC) should take over and carry on the quest to study elementary particles.

2.1.1 Accelerating system

The protons colliding at LHC are originally coming from hydrogen H_2 gas tanks. They are first converted into H^- ions in the Linac 4 accelerator (which took over when Linac

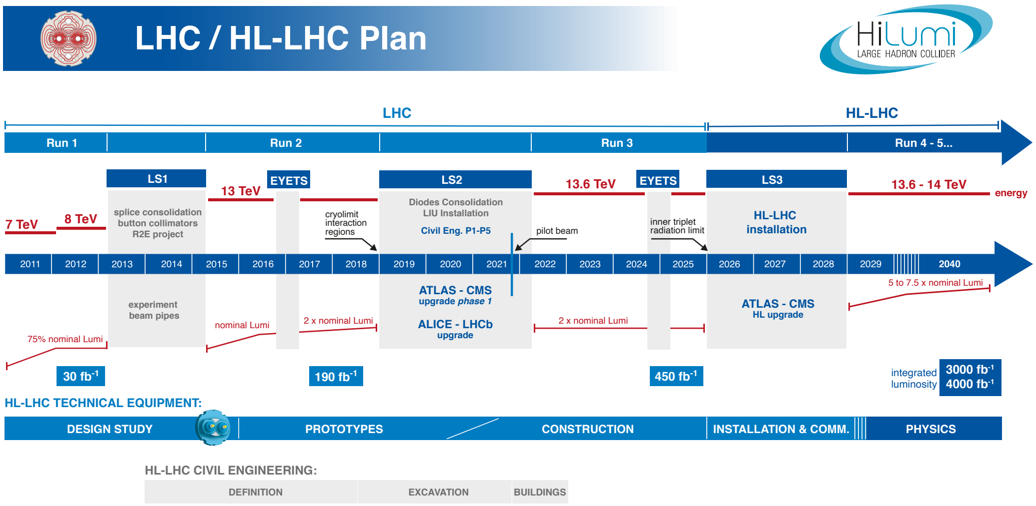

Figure 2.1: Schedule of the LHC and HL-LHC operation [82].

2 was decommissioned in 2018 [83]) where they reach an energy of 160 MeV. In the Proton Synchrotron Booster, the protons are stripped from the two electrons of the H^- ion and injected into the PS which accelerates them up to 26 GeV. The next step is the SPS which makes them reach 450 GeV before they can enter the main LHC ring. The LHC injection chain can be seen among other CERN accelerators in Figure 2.2.

The accelerator is situated in a tunnel which is 100 m deep in average. It does not form a perfect circle but is rather composed of circular sections where magnets bend the beam alternating with linear sections where the protons gets accelerated. There are actually two parallel beam pipes, one for protons rotating clockwise and one for the others rotating counter-clockwise. They collide at interaction points where the detectors are located (see below). A strong vacuum of 10^{-7} Pa is required inside the beam pipes to avoid the protons to hit any remaining atom [81].

Magnetic systems Powerful magnets are placed all over the circular portions of the ring to both keep the protons inside it and focus their bunches. The magnets are divided into dipoles and quadrupoles which respectively guide the beam on the circular trajectory and focus it horizontally and vertically. Additional multipoles magnets also exist to provide higher order corrections. The magnets are made in niobium and titanium (NbTi) and provide a magnetic field of 8.3 T. To reach such value, they need to be powered by strong currents of the order of 11 kA. This can only be achieved by using superconducting magnets which need to be cooled down at 1.9 K using superfluid helium.

Radio frequency cavities Radio frequency (RF) cavities are dispatched in the linear sections of the LHC. Their role is to accelerate the protons and to focus them into bunches

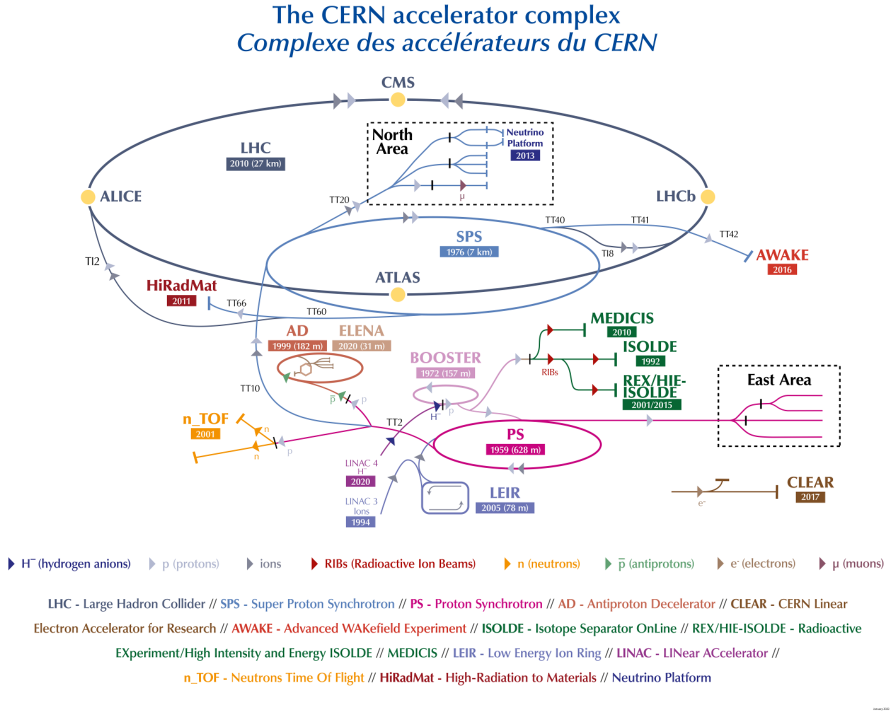

Figure 2.2: Layout of the CERN accelerator complex including the LHC in 2022 [84].

which is a critical feature as the more focused are the protons, the higher the number of collisions and thus the quantity of data taken. The RF cavities provide a strong electric field of 5 MV/m to accelerate the protons from 450 GeV in the SPS to 6 or 6.8 TeV in the LHC depending in the Run.

Finally, even if the LHC is primarily a proton-proton collider, another activity consists in colliding heavy ions such as oxygen or lead nucleus. These collisions intend to study the quark-gluon plasma, a particular state of matter which occurs when a large number of nucleons are colliding thanks to collective effects . The centre of mass energy of lead-lead collisions can reach 5.02 TeV.

2.1.2 Proton beams at LHC

The finality of LHC is to make these proton beams collide at interaction points where detectors are located. The different experiments at the LHC will be detailed in the next section but before, some general insights about proton-proton collisions at LHC will be given.

Luminosity There are 2808 bunches of protons at the same time in the LHC, which translates to a collision between bunches every 25 ns. Each bunch is composed of approximately 10^{11} protons. The physical quantity associated to the performance of collider is the *luminosity*. Instantaneous luminosity is defined as :

$$\mathscr{L} = \frac{1}{\sigma}\frac{dN}{dt} \tag{2.1}$$

where N is the number of inelastic pp collisions and σ is the cross-section of the process. $\mathscr{L}$ is therefore expressed in $m^2 s^{-1}$ and depends on the accelerator's characteristics like the size of the beams or the collision frequency whereas σ will quantify the likeliness of a physical process to happen.
The total number of event collected can be obtained by integrating the instantaneous luminosity :

$$N = L_{int}\sigma = \int \mathscr{L}(t)dt\sigma \tag{2.2}$$

The integrated luminosity L_{int} is an indicator of the number of proton-proton collisions recorded by the detector. It is expressed in inverse barn (b^{-1}) where the barn is a unit of surface used to quantify the cross-section ($1\mathrm{b} = 10^{-28}\ m^2$).
The nominal instantaneous luminosity of LHC is $10^{34}\ \mathrm{cm}^2\mathrm{s}^{-1}$. The values varied between $0.5 \cdot 10^{34}$ and $2 \cdot 10^{34}$ during Run 2 and lead to an integrated luminosity of 139 fb^{-1} after some data quality requirements. This will be the dataset used for the search for additional scalar bosons presented in Chapter 4. With the plans to increase instantaneous luminosity for Run 3 and HL-LHC, the prospected integrated luminosity is respectively of 300 fb^{-1} and 3000 fb^{-1}.

Pile-up As we've seen, increasing the instantaneous luminosity means increasing the quantity of data recorded. But when two bunches of protons are colliding, there are usually more than one pair of protons interacting. Physicists are interested in recording the highest energetic interaction of the bunch (referred as the hard-scatter interaction) while the other softer interactions, referred as *pile-up*, are only considered as a background to it. Increasing the luminosity will therefore increase the number of those unwanted interactions, possibly decreasing the quality of the data recorded while increasing its quantity.

As seen in Figure 2.3, the pile-up value is strongly depending on the data-taking period since the LHC beam parameters are varying over time. The LHC nominal pile-up is 20 which is lower than the average pile-up observed during Run 2. It is expected to increase up to 140 in average and with maximum values around 200 during HL-LHC. Limiting the effect of pile-up on performance is therefore a priority for the HL-LHC era. However, the current detector is already performing well despite experiencing pile-up levels higher than originally designed for. An example of efforts towards this goal will be given in Chapter 3 with the flavour tagging performance.

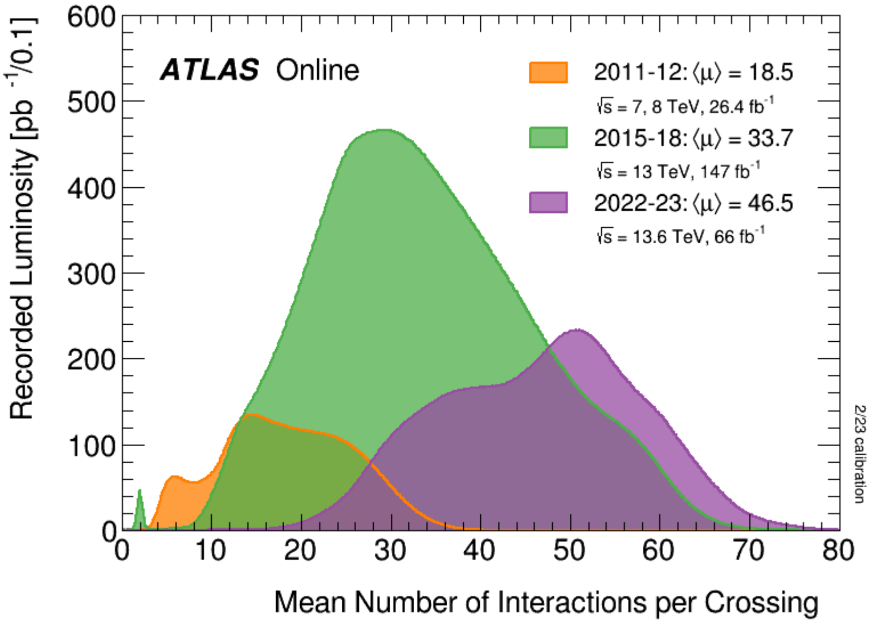

Figure 2.3: Average number of interactions per bunch crossing in the ATLAS detector weighted by the integrated luminosity for Run 1 and 2 and the beginning of Run 3 [85].

2.1.3 Experiments at the LHC

To complete the physics program of the LHC, four main experiments were built on the collider.

ATLAS (A Toroidal LHC ApparatuS) and **CMS** (Compact Muon Solenoid) are multi purpose detectors with primary focuses on Higgs and top physics as well as precision tests of the Standard Model. The two detectors have a different conception, CMS is notably much more compact (21 m long vs 46) but heavier (14,000 tons vs 7,000) than ATLAS. The magnetic field is provided in CMS by a huge solenoid, giving its name to the experiment. It must be confined by a 'yoke' made of steel which is responsible of the heaviness of the detector. ATLAS will be described in more details in Section 2.2 as it is the main focus of this thesis.

LHCb (Large Hadron Collider beauty) is an experiment dedicated to the matter-antimatter asymmetry and CP violation through b-quark physics. It can also make precision tests of the Standard Model like lepton flavour universality or lepton flavour violation. LHCb has the particularity to be an asymmetric detector as most of the b-quarks are produced along the beam axis direction.

ALICE (A Large Ion Collider Experiment) is a detector specialized in heavy-ion collisions. This allows to specifically study the strong interaction with the Quantum Chromodynamics theory and the quark-gluon plasma (QGP).

2.2 The ATLAS detector

The ATLAS detector [86] is located 100 m underground at the LHC Interaction Point 1. It has the form of a lying cylinder of 44 m in length and 25 m in radius and weight 7,000 tons, which makes it the largest detector build around a particle collider. Most of the detector's specifications were designed to observe the Higgs boson but are also useful to study top quark physics, precision tests of the SM and any BSM phenomena at the TeV scale.
The three main subdetectors of ATLAS are the Inner Detector, the calorimeters (both electromagnetic and hadronic) and the Muon Spectrometer. They are presented in the following subsections along with two important features of ATLAS which are the magnets and the trigger and data acquisition systems. The Run 2 ATLAS detector will be presented here since the data used for the analysis presented in Chapter 4 was taken under this configuration.

ATLAS layout and coordinate system ATLAS uses a Cartesian coordinate system with the origin situated at the interaction point (IP). The z axis corresponds to the beam pipe while the x axis points towards the centre of the LHC ring and the y axis towards the surface. Additional spherical and cylindrical coordinates are also useful : (r,ϕ) are the radial and azimuthal coordinates in the plane perpendicular to the beam axis (the transverse plane, in which quantities such as the transverse momentum p_T or the transverse energy E_T are defined) while θ is the angle with respect to the beam axis [86]. Finally, pseudorapidity η is a Lorentz-invariant variable useful to describe the angle with respect to the beam axis. It is defined as $\eta = -\ln(\tan(\theta/2))$. A pseudorapidity of 0 therefore corresponds to the direction perpendicular to the beam axis and $\eta = \infty$ is the beam axis direction. It is also used to define the angular distance in the (η,ϕ) plane $\Delta R = \sqrt{\Delta\phi^2 + \Delta\eta^2}$

2.2.1 Inner Detector

A key feature of the detector is to measure the momentum of particles emitted during the collisions. To do so, the trajectory of the particles which is bent under the magnetic field must be carefully tracked. The Inner Detector (ID) [87, 88] aim to provide precise momentum measurement and vertex identification through a good tracking resolution. The objective of the ID is to record the trajectory and provide some insights for particle identification. It is designed to preserve as much as possible the particle's energy which will be recorded in the calorimeters.

The ID is composed of three subdetectors which cover tracking up to $|\eta| < 2.5$:

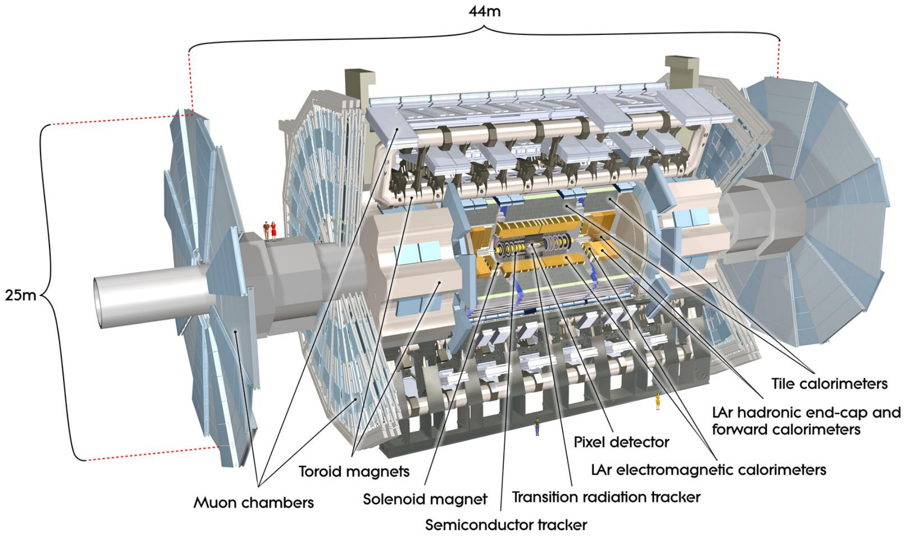

Figure 2.4: Cut-away general view of the ATLAS detector [86].

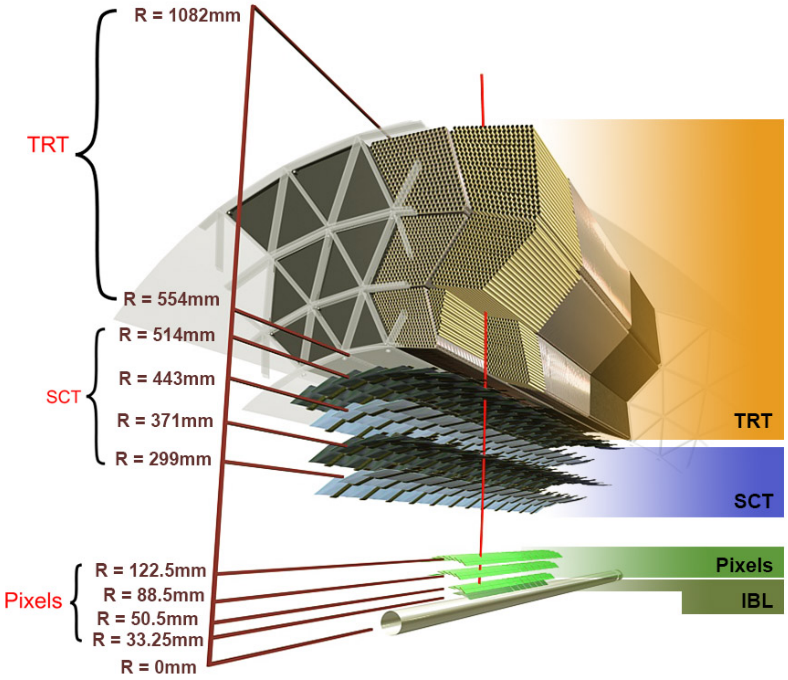

Figure 2.5: Representation of the ATLAS Inner Detector layers in the barrel [89].

Pixel Detector The Pixel Detector [90] consists in concentric layers of silicon pixels which are the type of detector that achieve the highest granularity. The layers are parallel to the beam axis in the barrel and perpendicular to it in the end-cap. The Pixel Detector

is the innermost part of the detector with its outermost layer situated at $R = 1.22$ m. Between Run 1 and 2, another layer was added close to the beam pipe at $R = 33.25$ mm : the Insertable B-Layer (IBL) [91].
The pixels are 50 × 400 μm large in the $R-\phi$ dimensions and the pixels of the IBL are smaller (50 × 250 μm) since they are more recent. There are 92 million reading channels in total. This leads to a particle hit position resolution of 10 μm in the (r,ϕ) plane and 115 μm in the z direction (respectively 8 μm and 40 μm in the IBL layer) [86].

Semi Conductor Tracker (SCT) The SCT is relatively similar to the Pixel Detector but uses silicon strip sensors instead which are narrower (12.8 cm long and 80 μm large). It is situated further away from the beam than the Pixel detector, therefore performing tracking in the transverse plane. The 6 million electronic channels allow the hit resolution to reach 17 μm in the (R,ϕ) and 580 μm in the z direction [86].

Transition Radiation Tracker (TRT) The TRT is the outermost subdetector of the ID and uses a different detecting technology than the Pixel and the SCT. It is made of straw tubes filled with a gas mixture composed of Xe, CO_2 and O_2. Xe was replaced by Ar between Run 1 and 2 in tubes which encountered large gas leakage [92]. This gas mixture is ionized by the passing particles and the charges produced can be collected in the wires. The tubes are parallel to the beam axis and cover a region up to $|\eta| = 2$ resulting in a 130 μm resolution in (R,ϕ) but give no information on the z position.
The TRT compensates the worse precision and less important coverage with respect to the Pixel and the SCT by a large number of measurements in the tubes at a large radius which is important for the overall p_T measurement. Finally, the TRT takes part in electron identification (see Section 2.3.2).

2.2.2 Calorimeters

Calorimeters are detectors conceived to measure the energy of particles. They work by stopping the incoming particles and collecting the energy deposited during the slowing down process. They also participate in the particle identification process and provide position measurement for photons which do not interact in the Inner Detector.
In ATLAS, the calorimeters are situated directly on the outside of the ID (Figure 2.6). In the central region which is also covered by the ID, fine precision measurements of electrons and photons are possible while the coverage is less dense in the forward region but still allow to achieve good performance in jet and missing transverse energy (E_T^{miss}) reconstruction.
There are actually two type of calorimeters depending on the type of particle intended to be measured : the electromagnetic calorimeter collects the energy of particles interacting with the electromagnetic interaction like electrons and photons whereas the hadronic calorimeter is designed to measure strongly interacting particles like neutrons or pions. Both calorimeters used by ATLAS are of the sampling type, meaning that layers composed of absorbing materials alternate with layers measuring the deposited energy.

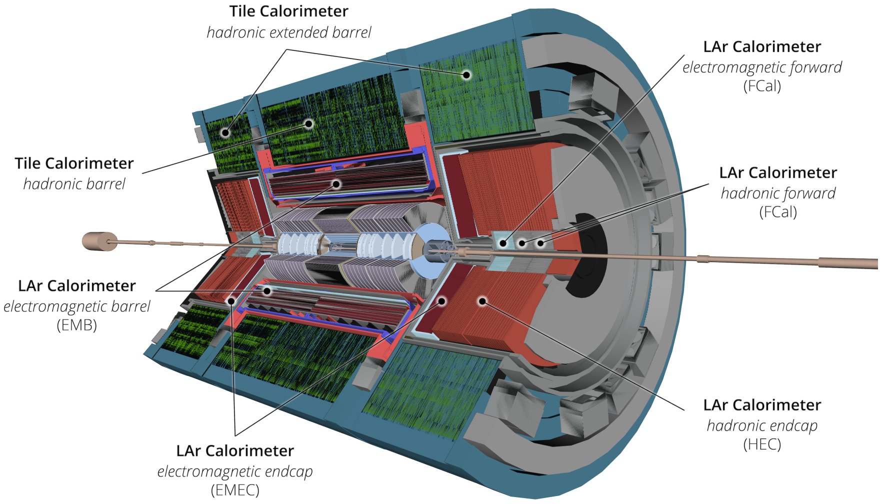

Figure 2.6: Cut-away view of the ATLAS electromagnetic and hadronic calorimeters system [93].

Electromagnetic calorimeter The Electromagnetic calorimeter (EM Cal) [94] is the innermost calorimeter and is designed to collect the energy and identify electromagnetically interacting particles. Charged particles like electrons typically loose their energy through bremsstrahlung and the energetic photons from the bremsstrahlung radiation will interact with the nuclei of the medium to form electron-positron pairs. These two alternating and self-maintained processes will form what is called an *electromagnetic shower*. EM calorimeters intend to collect all the deposited energy of the shower to trace back to the incoming particle initial energy.

The EM calorimeter is composed of a barrel (for $|\eta| < 1.475$), two end-cap sections ($1.375 < |\eta| < 3.2$) and a Forward Calorimeter (FCal) which covers the region closest to the beam axis ($3.1 < |\eta| < 4.9$). It consists in absorbent layers made of lead (as the stopping power increases with the atomic number) immersed in liquid argon (LAr) which is the active material. The lead layers and connecting electronics have an accordion shape because this geometry naturally provides a full azimuthal (ϕ) coverage without blind spots. The FCal is also filled by LAr but uses copper and tungsten instead of lead as a stopping element.

The LAr calorimeter energy resolution takes the form [94]:

$$\frac{\sigma(E)}{E} = \frac{a}{\sqrt{E}} \oplus \frac{b}{E} \oplus c \qquad (2.3)$$

a represents the sampling term due to the part of the EM shower which is not recorded in the calorimeter and is of the order of 10%. b corresponds to the noise which is either from electronic or pile-up origin and is dominant below 20 GeV. c is a constant term coming from the design of the calorimeter and its calibration system. It will dominate at the high end of the energy spectrum. The total energy resolution depends on the type of the measured object.

Hadronic calorimeter Hadrons like protons, neutrons or pions interact with matter by forming so-called *hadronic showers*. Their strong interactions with the nucleus from the medium produce secondary particles which will perpetuate the process until the energy falls below a certain threshold. Hadronic showers are also intertwined with EM showers because neutral pions can be produced and decay into a pair of photons.
The ATLAS hadronic calorimeter is composed of three distinct parts which have a different detector type. A tile calorimeter [95] is placed in the barrel, which is itself divided into three parts. It is located directly outside the EM calorimeter and spread radially between 2.28 m and 4.25 m, making it cover a pseudorapidity range up to $|\eta| = 1.7$. It is made of steel layers and plastic scintillating tiles. They are the active material that firstly produce secondary photons which will be converted into electric current. The tile calorimeter is the heaviest component of ATLAS with a weight of around 2,900 tons. In the end-cap region ($1.5 < |\eta| < 3.2$), a LAr calorimeter is used again but with a different geometry and copper instead of lead as the stopping layer. Finally, the hadronic LAr FCal completes the EM one in the beam axis direction ($3.1 < |\eta| < 4.9$).

2.2.3 Muon spectrometer

The muon spectrometer (MS) [96] is the outermost and largest part of the ATLAS detector. They have an outer radius of around 20 m and the muons are almost the only particles reaching this far because they emit very few bremsstrahlung radiation due to their relatively high mass and they also interact loosely with nuclei. The role of the MS is to precisely measure the momentum of the muons using the deflection of their trajectory caused by the toroidal magnets (see next section) and also to be used as a trigger system for bunch identification.
The MS uses two different type of chambers to perform the momentum measurement :

- Monitored Drift Tubes (MDT) are situated in the barrel and the beginning of end-caps to cover up to $|\eta| < 2.7$ and provide an excellent spatial resolution of the muons hits.
- Cathode Strip Chambers (CSC) covers the innermost layer of the end-cap (between $2 < |\eta| < 2.7$) with a higher granularity than the MDT.

The triggering task of the Muon Spectrometer is done by two other devices in the central region ($\eta < 2.4$) :

- Resistive Plate Chambers (RPC) are used in the barrel.
- Thin Gap Chambers (TGC) are used in the end-caps.

The MS provides a 50 μm resolution on the hits position in order to reach a 10% p_T resolution at 1 TeV [86].

2.2.4 Magnet system

Magnetic fields are crucial features of a particle detector as the curvature of the charged particles trajectories allows to measure their momentum. As such, the design of the ATLAS magnet system drove the design of the entire detector [97, 98].

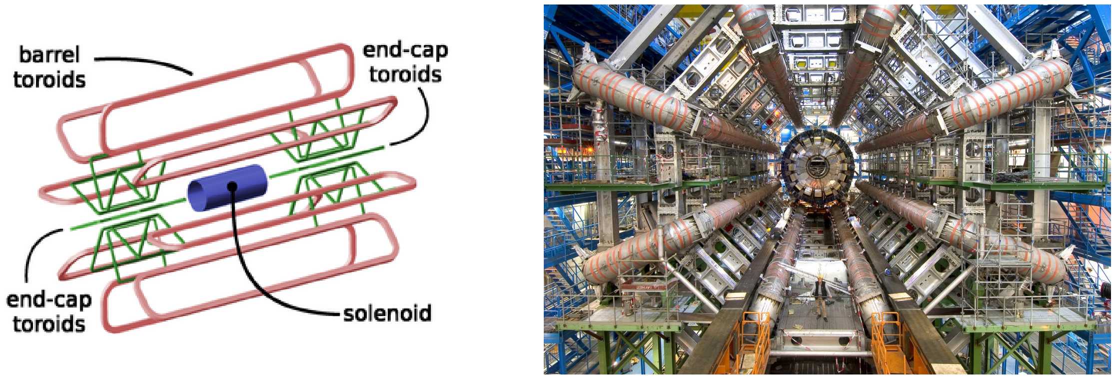

Figure 2.7: Sketch representing the magnet system of ATLAS (left) [99] and picture of the barrel toroidal magnets during the construction of the detector (right - Image credit : M.Brice/CERN).

.

It is composed of a central solenoid and a barrel and end-cap toroidal superconducting magnets (Figure 2.7 - left). The solenoid is situated between the Inner detector and the EM calorimeter and provides a 2 T magnetic field in the beam axis direction for the tracking purpose of the ID. The toroidal magnets are intertwined with the Muon Spectrometer and are the largest and most recognizable part of ATLAS (Figure 2.7 - right). The resulting magnetic field is not uniform and varies from 1 T in the end-caps to 0.5 T in the barrel [86].

2.2.5 Trigger system and data acquisition

As discussed before, bunch of protons collide once every 25 ns in the ATLAS detector. This represents a colossal amount of data which is impossible to process and store with current means. A *trigger* system is therefore used to only select events which are more likely to be interesting for physics analysis. This system named Trigger and Data Acquisition (TDAQ) functions in multiple level.
The first one [100], called L1, uses partial information from the detector to make a first selection to reduce the rate of events from 40 MHz to 100 kHz. This hardware system uses information from the calorimeters and the dedicated system of the MS (RPC and TGC) to make the decision to record the event or not in 2 μs in average. A second level called High Level Trigger (HLT) [101] operates another selection. It is a software trigger based on the full available data in "regions of interest" that has been defined by L1. This

further reduces the event rate to an average of 1.2 kHz which makes up a data size of around 80 TB per day since the size of an ATLAS event is of the order of 1 MB [102]. The treatment to go from those raw detectors measurement to reconstructed particle objects is studied in the next section.

2.3 Objects reconstruction and identification

This section presents how the different information from the subdetectors are recombined to reconstruct physical objects like electrons, photons, muons or jets that are used to make physics analysis in ATLAS.

2.3.1 Tracks and vertices

The tracks are the reconstructed trajectories of particles in ATLAS.
They are essentially based on *hits* which are the places where particles are passing through a layer of the Inner Detector. Hits are reconstructed as *clusters* formed of groups of neighbouring pixels or strips where energy has been deposited.
As discussed in Subsection 2.2.1, tracking itself is carried out for $|\eta| < 2.5$ and $p_T >$ 0.5 GeV. Going from the hits information in the detector to the final track object is done in three steps and involves several algorithms [103, 104].
Firstly *seeds*, which are combination of three hits space points, are created. The seeds are then extended to become track candidates with a Kalman filtering algorithm [105] which adds additional space points from other layers of the ID.
An ambiguity solving step is needed to remove fake tracks among the candidates. Quality criteria such as the number of holes (i.e a missing measurement on a track where a hit would be expected) or the number of hits in the SCT and pixel detectors are applied and track candidates are assigned a score to keep the best ones. Shared hits, which are merged clusters of pixel common to two or more tracks, are taken care of by a neural network [106] which identify the number of particles that created a cluster. Finally, the best track candidates are fitted to provide as precise as possible track parameters.

Vertexing A vertex is simply defined as the point at the origin of a track. The vertex finding algorithm [107] reconstructs the vertices of hard-scatter interactions.
A first vertex seed is defined using the tracks collection described in the previous paragraph. A χ^2 fit estimates the best vertex position assuming a helicoidal trajectory of charged particles under the magnetic field. The fit is iterative and at each step tracks receive a weight depending on their compatibility with the vertex position. In the end, tracks that are incompatible with the determined vertex are used as a new seed to find another one until none are left.
Once all the vertices of an event have been found, the vertex which has tracks with the largest transverse momentum p_T sum is labelled as the *primary vertex* (PV). The associated interaction is used for physics analysis while the other vertices are called

pile-up interactions.
In analyses targeting the $H \rightarrow \gamma\gamma$ decay, the diphoton vertex determination also uses the intersection of the extrapolated photon trajectories which are obtained by the longitudinal segmentation of the calorimeter information [108].
In some cases, particles from the PV can decay at a short but sizeable distance of it to form a secondary vertex (SV). They can sometimes be reconstructed, a feature which can be used for jet flavour tagging (see Chapter 3).

2.3.2 Electrons and photons

Photons and electrons are both primarily reconstructed with their energy deposit in the electromagnetic calorimeter.
The reconstruction procedure is illustrated in Figure 2.8. Clusters in the calorimeters are formed of cells encountering a signal at least 4 standard deviation away from the expected electronic noise [109].
The clusters are matched to tracks in the ID which is a way to separate the electrons from the photons since e^- are charged and are more likely to be associated to a track whereas photons should not be associated to any track. However, special attention must be taken to *converted photons* which are photons that interact in the ID to form a e^+e^- pair. This happens around 20% of the time for photons in the central region and up to 65% at $|\eta| = 2.3$. Tracks originating from the ID layers are matched to clusters in the calorimeter in order to reconstruct the interaction vertex called conversion vertex. On the other hand, *unconverted photons* are reconstructed from clusters that are not associated to any track or conversion vertex.

Photons and electrons are then reconstructed separately from the collection of clusters and (possibly) associated tracks. Superclusters which encompasses the original clusters and their neighbours are formed to take into account bremsstrahlung radiations that might deposit energy outside the main cluster. Electron reconstruction is ensured up until $|\eta| = 2.47$. The reconstruction efficiency is around 98-99% [110] but is significantly lowered in the crack between the barrel and the end-cap for $1.37 < |\eta| < 1.52$.
Energy calibration [111] happens at this step using samples of $Z \rightarrow e^+e^-$ decays and takes into account the energy loss by bremsstrahlung in the ID for the electrons. At low E_T, $J/\psi \rightarrow e^+e^-$ decays are used instead. Energy resolution uncertainty varies between 0.05% to 0.4% for electrons depending on the transverse energy and reaches 0.2% for photons.

Photon and electron isolation variables are defined to reduce the contributions from pile-up nearby tracks or energy deposits in the calorimeters [109]. Calorimeter-based isolation variable E_T^{iso} is the sum of the transverse energy measured in topological clusters inside a given cone around the object after subtracting an average expected pile-up contribution. The cone size is $\Delta R = 0.2$ for electrons and either 0.2 or 0.4 for photons. Track-based isolation variable p_T^{iso} corresponds to the scalar sum of the transverse momenta of all tracks with $p_T > 1$ GeV originating from the primary vertex

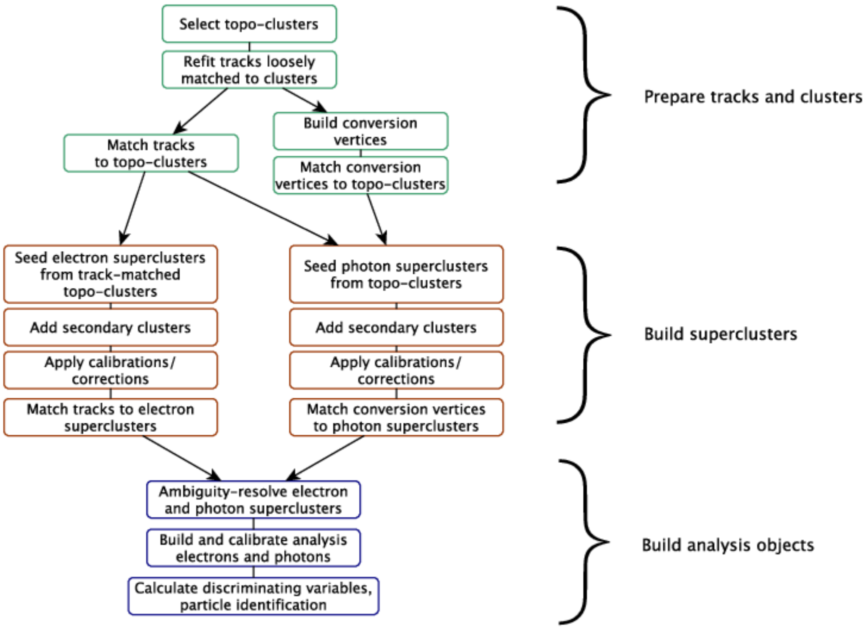

Figure 2.8: Diagram of electrons and photons reconstruction algorithm procedure [109].

and within a similar cone around the photon. Different working points are considered with criteria on the track and calorimeter based isolation variables. Loose (Tight) electrons must verify $E_T^{iso}/p_T < 0.020$ ($E_T^{iso}/p_T < 0.006$) and $p_T^{iso}/p_T < 0.15$ ($p_T^{iso}/p_T < 0.05$). For photons, the calorimeter isolation criteria is $E_T^{iso20}/E_T < 0.065$ for Loose and $E_T^{iso40} < 0.022 \times E_T + 2.45$ GeV for Tight where 20 or 40 indicates the considered cone size $\Delta R = 0.2$ or 0.4. The track isolation criteria is the same for both categories : $p_T^{iso20}/E_T < 0.05$. This leads to efficiency range from 84% to 98% for isolated photons with transverse energies between 30 and 250 GeV.

The final step is the identification where electrons and photons candidates needs to be separated from each other as well as with other objects which could be misidentified jets or secondary electrons. Since the superclusters reconstruction is made independently, they can be candidates for both categories. This ambiguity is intentional as ambiguous electron-photon objects can be used differently depending on the physics analyses.
For electrons, a likelihood discriminant is computed and three operating points are used depending on their score : Loose, Medium and Tight [109]. Corresponding efficiencies are 93%, 88% and 80%. Discriminating variables include the shape of the showers in the EM and hadronic calorimeters, tracks information and properties of the matching between the track and the clusters.
For photons, simple cuts are applied using the shower shape variables. Similarly to e^-, three levels of selection are defined : Tight, Medium and Loose. Identification

efficiency varies between 60% and 95% for unconverted photons and between 50% and 95% for converted ones [110]. The values depend on pseudorapidity and transverse energy and significantly decrease when $E_T < 60$ GeV for unconverted photons (80 GeV for converted ones).

2.3.3 Jets

As previously described in Subsection 1.1.3, jets are collimated streams of various types of particles. As such, they are complex high level objects which use information from various subdetectors to be reconstructed.
Jets are reconstructed using the anti-k_T algorithm [112]. Pairs of objects that have a corresponding p_T are merged in an iterative procedure. The output are perfectly conical hard jets which are characterized by their angular radius $R = 0.4$. The anti-k_T algorithm presents the advantage of being robust against collimated particles misreconstructed as one (refered as collinear security) and on the radiation of soft particles (called infrared security).
ATLAS uses two collections of jets objects :

- Particle Flow (PFlow) jets [113] are reconstructed using information from both tracks in the ID and topoclusters of cells in the calorimeters. If the topoclusters are matched with a charged particles track, the track energy obtained in the ID replaces the one deposited in the EM calorimeter in the computation of the total jet energy. Indeed, for low-energy charged particles, the momentum resolution of the tracker is significantly better than the resolution of the calorimeter.
  Taking into account ID information also allows to include soft particles that wouldn't have an form a topocluster in the calorimeter in the jet.

- Electromagnetic Topocluster (EMTopo) jets are older objects used before Run 2 that are based on calorimeter clusters only. The jets used for upgrade studies in Chapter 3 are EMTopo jets since PFlow jets were not calibrated yet at the time of the studies.

Both collections can define jets with a transverse momentum $p_T > 20$ GeV. However softer jet named *track jets* can also be defined using only information from the ID.

The Jet Vertex Tagger (JVT) algorithm [114] is used to identify jets coming from pile-up interactions. It uses a likelihood discriminant based on two variables linked to the jet p_T fraction coming from the primary vertex.

The jet energy scale (JES) is calibrated with a procedure illustrated in Figure 2.9 [115]. Correction to the pile-up contribution to the energy are made in two steps with a first correction which depends on the jet area and followed by a residual correction which depends on the mean μ and measured N_{PV} number of interaction in the bunch crossing. The absolute calibration consists in compare the jet with simulated one to calibrate the energy and direction. It is followed by the global sequential calibration which smooths

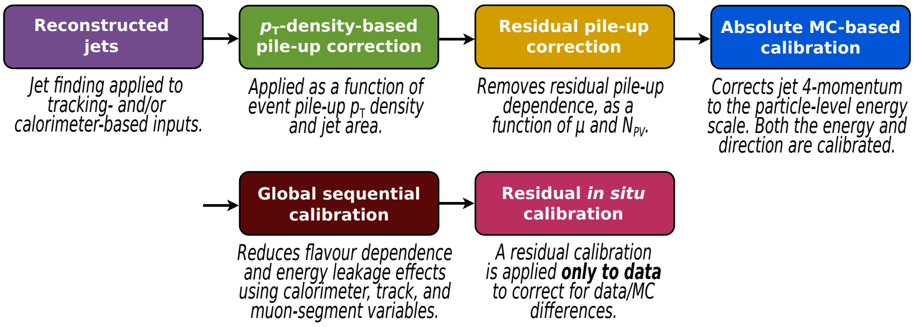

Figure 2.9: Sketch representing the different steps of the jet energy scale calibration which are applied to the four-momentum of the jet [115].

the contributions coming from the different subdetectors in the energy calculation. Lastly, the in-situ calibration computes scale factor to take into account the differences between data and MC.

The jet energy resolution (JER) is depending closely on the jet p_T [115]. It takes the form :

$$\frac{\sigma(p_T)}{p_T} = \frac{N}{p_T} \oplus \frac{S}{\sqrt{p_T}} \oplus C \tag{2.4}$$

N represents an electronic and pile-up noise term, S is a stochastic term accounting for the energy deposits statistical fluctuations and C is a constant term corresponding to the energy deposits in the passive materials of the detector or the non-uniformities of response in the calorimeters.

Finally, the identification of the type of quark at the origin of the jet, referred as *flavour tagging*, is described in more detail in Chapter 3.

2.3.4 Muons, τ leptons and Missing Transverse Energy

This subsection discusses important objects in ATLAS but which are not directly used in the studies of this thesis, muons, τ leptons and missing transverse energy.

Muons The muon reconstruction in ATLAS [116] uses information from the Inner Detector, the calorimeters and of course the Muon Spectrometer. *Combined muons* benefit from a matching track in the ID in addition to the one in the MS and take into account the energy loss in the calorimeters. *Segment-tagged* (ST) are a more loosely defined category which works from an ID track extrapolated to the MS and matching to one of its segment, hence the name. Muons candidates that are too much in the forward region to be covered by the tracking of the ID but are reconstructed thanks to the larger coverage of the MS up to $|\eta| = 2.7$ are called *extrapolated* (ME). Lastly, *Calorimeter tagged* muons (CT) are identified with a track in the ID matched to a signature in the calorimeters corresponding a minimum ionizing particle.

τ leptons Taus reconstruction is done separately between leptonic and hadronic decays. Hadronically decaying taus named $\tau_{had-vis}$ (which have a 65% branching fraction) are reconstructed using jet candidates [117, 118]. A boosted decision tree (BDT) is then employed to separate the taus from the jets using inputs related to tracks or comparison between the energy deposits in the EM and HCal.
Taus decaying leptonically are not directly considered as objects in ATLAS but can be used in analyses with τ in the final state as events with a single electron or muon and missing energy associated to the two neutrinos.

Missing Transverse Energy Since the protons are colliding head-on, the total momentum of the particles emitted in the transverse plane must be equal to 0. If the total transverse energy collected by the detector, which has an almost 4π solid angle coverage, is not equal to 0, it mean that undetected particles have been emitted during the collision. This particles could be neutrinos or more exotic beyond Standard Model particles which could interact extremely weakly with the common matter composing the detector.
Measuring the missing transverse momentum E_T^{miss} (or p_T^{miss}) [119], which is the negative vectorial sum of the transverse momenta of all reconstructed particles and energy deposits in the detector in an event, is of crucial importance for physics analyses involving neutrinos or weakly interacting BSM particles.

2.3.5 Monte-Carlo simulations

Most high-energy physics experiments relies on comparing the observed data to the one expected from the theory. This can be done by performing simulations of the different physics process that can be produced during the collisions and their interactions with the detectors. Having simulations allow to see what are signal and background events characteristics to design methods to separate them, and at the end to notice an excess in the events which could be signal.
The simulation happens in two steps : firstly the physical event is generated in what is called a *Monte-Carlo simulation* (MC) and then the interaction of the process within the detector must be generated.

Event Generation The event generation is itself divided in two steps. The first one is the matrix element (ME) generation which models the hard-scattering pp interaction between the protons. At the energy range of LHC, it's the partons which are the quarks and gluons composing the proton that are interacting. The initial conditions on their energy are described by the parton distribution function (PDF). Their implementation in the generator is called the PDF set.
The matrix element of a process at a given collision energy is computed with the different Feynman diagrams. Since the computation is done up to a certain order using perturbation theory, leading order (LO), next-to-leading order (NLO) and so on diagrams can be taken into account depending on the level of precision needed. Increasing the precision comes at the cost of an increased computation time.

The second step takes place after the hard-scatter interaction. The partons which were produced, and the ones that didn't interact at all (called the *underlying event*) behave like free particles at first but are encounter QCD interactions in a process called hadronization or *parton shower* as described in Section 1.1.3.

In the parton shower, at high energy, simulation uses perturbative QCD with radiation of quarks and gluons. For the hadronization part when the partons recombine to form hadrons at lower energy, the simulation relies on different models since no calculation is possible. The energy scale at which the transition happen is called the factorization scale μ_F. Gluons and photons radiated before (initial state radiation - ISR) or after (final state radiation - FSR) the hard-scatter interaction must also be taken into account. Parton shower simulation relies on either approximation of QCD calculations or phenomenological models to represent them. The models depend on several free parameters which need to be optimized. The final optimized values are called MC generator tunes. The different steps of the MC simulation are illustrated in Figure 2.10.

The task of generating an event is done by using a Monte-Carlo generator. Some of the generators like Pythia, Herwig or Sherpa are able to perform the whole simulation process whereas some generators like MadGraph or Powheg (refers as ME generators) only describe the pp and hard-scatter interaction.

Detector interaction The last part consists in simulating the interaction between the physical events described in the last paragraph to the detector. This is performed in ATLAS by the Geant4 (GEometry ANd Tracking 4) [121] software which simulates the interactions between particles and radiations with the ATLAS material and computes the hits in the ID or the energy deposits in the calorimeters. The results can be compared to the direct output of the MC which is called the *truth level* and permit reconstruction, identification and isolation efficiency studies.

This detector interaction step is the longest and most-CPU consuming task of the simulation. Therefore two types of simulation are used within ATLAS : the FullSim [122] which emulates the entire detector and has the highest precision is used for the physics analyses nominal samples, and the FastSim (AFII) [123] uses a simplified version of ATLAS to quicken the reconstruction process and uses models for the electromagnetic showers caused by charged particles instead of simulating them. This second category is used for the systematic experimental uncertainties.

In the end, the reconstruction step from the information in the detector to the physical objects is exactly the same between simulation and data.

2.4 Upgraded tracking at ATLAS during HL-LHC

The HL-LHC era [124] that will take place from 2029 (see Figure 2.1) aims at increasing the instantaneous luminosity of the collider to gather more statistics much needed for physics analyses. The targeted instantaneous luminosity at HL-LHC is 7.5×10^{34} cm^{-2} s^{-1} which is 3.5 times the one recorded during Run 2. These numbers

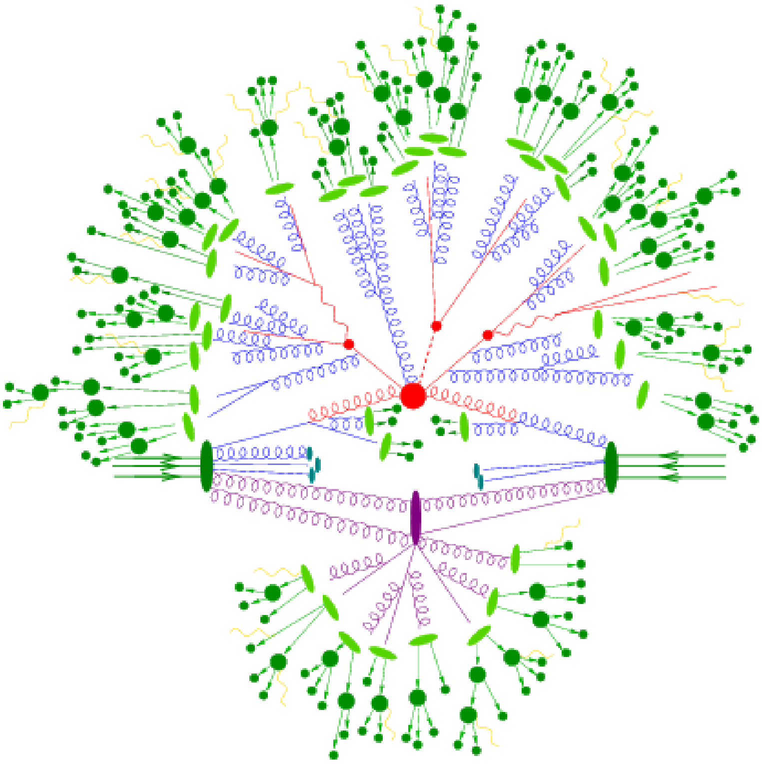

Figure 2.10: Sketch representing a simulated proton-proton collision with the hard-scatter interaction at the top and the underlying event at the bottom. The numerous interactions between quarks (in red) and gluons (in blue) form the parton shower that produces hadrons which will interact with the detector (in green) [120].

could lead to a total collected data equal to 3000 fb^{-1}, more than 20 times the amount from Run 2.

The di-Higgs process could for instance be observed with a statistical significance of 4σ by simply extrapolating Run 2 analysis results with such a dataset [125].

In parallel of this collider upgrade, the ATLAS detector will also undergo some major changes and improvement. These changes will have to tackle the crucial issue of pile-up (Figure 2.11) which comes up with the improved luminosity.

This section describes the main upgrades of ATLAS to prepare for the HL-LHC, with a particular focus on the new Inner Tracker (ITk) in 2.4.2 and the related tracking performance in 2.4.3. They are notably important for the flavour tagging upgrade performance which is discussed in Chapter 3.

2.4.1 Upgraded ATLAS detector for HL-LHC

TDAQ As the luminosity increase essentially implies to process more data, the Trigger and Data Acquisition System will be heavily impacted by the modifications [126]. The

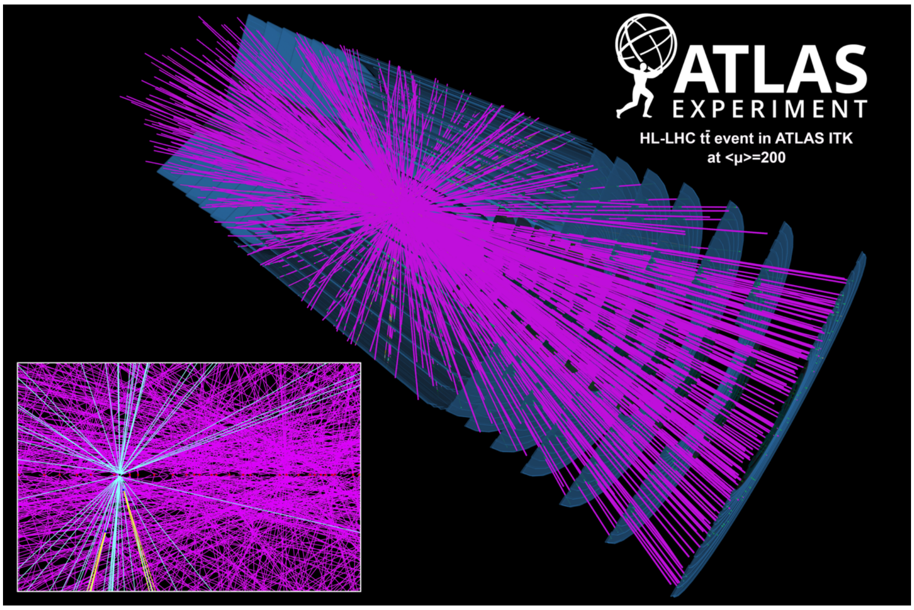

Figure 2.11: Event display of a simulated $t\bar{t}$ event with 200 pile-up at HL-LHC.

readout rate will notably be increased from the current 100 kHz to 1 MHz. To cope with that, several subdetectors will be affected : the electronic readout system of the calorimeters will be replaced [127, 128] as well as the ones from the Muon Spectrometer RPC and TGC detectors. In the MS, the MDT will now also take part in the trigger decision and these hardware changes are already in place since the New Small Wheel has been installed before Run 3 [129].

HGTD The High-Granularity Timing Detector (HGTD) [130] is a new silicon detector meant to mitigate the pile-up effect by improving the timing resolution of the collisions. This new detector will be situated just outside of the ITk in the end-caps, between $|\eta| = 2.4$ and 4. It will be composed of two double-sided silicon layers and the timing information will be provided by low gain avalanche diodes.
The HGTD will allow a time resolution of 30 to 50 ps, which is 6 times smaller than the temporal spread of the collisions in the bunch crossing, therefore helping to determine if a track comes from the hard scatter interaction or from a pile-up one.

2.4.2 Inner Tracker

Improving tracking is essential for HL-LHC since an increased luminosity means a larger number of tracks in every beam crossing. To answer this problematic, the ATLAS Inner Detector will be replaced by the new Inner Tracker (ITk).
The ITk is an all-silicon detector composed of two subsystems : the innermost Pixel detector [131] and the Strip detector [132] which surrounds it. The global layout of the active material of ITk is illustrated in figure 2.12. The latest design, which has been

loosely modified since the Technical Design Reports, comes from reference [2].

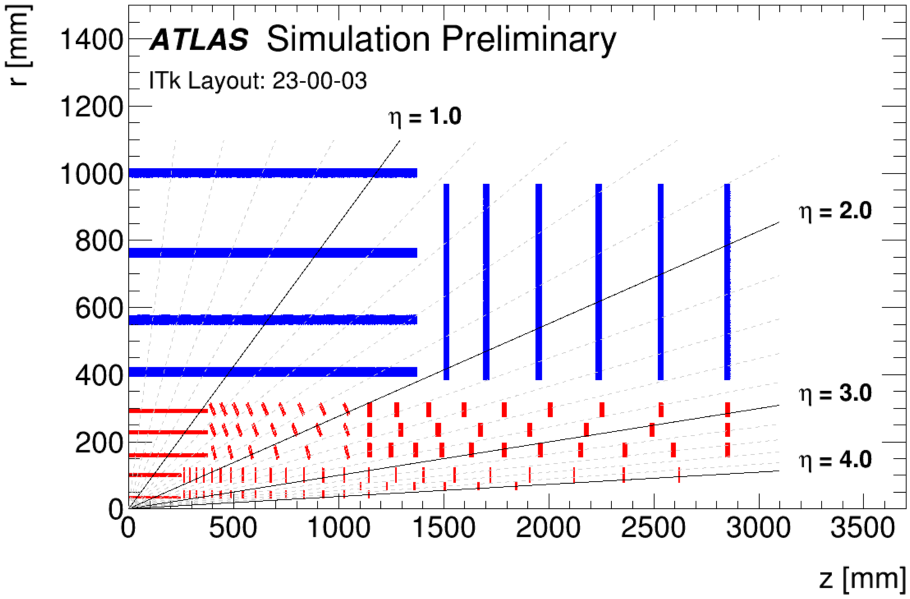

Figure 2.12: General schematic depiction of the ITk layout 23-00-03 in a plane parallel to the beam. Only the active elements are shown with the Strip detector in blue and Pixel detector in red [2].

The Pixel detector consists of five layers parallel to the beam in the barrel and five layers vertical or inclined providing an extended coverage up to $|\eta| < 4$ in the forward region. It has an innermost layer 34 mm away from the beam which is similar to the ID and the outer layer is situated at $R = 291$ mm. The pixel pitch size has been set to 50×50 μm^2 with the exception of the innermost layer for which the sensor size is 25×100 μm^2.

The Strip detector is made of four module layers in the barrel region and six disks in the end-caps to cover the pseudorapidity range $|\eta| < 2.7$. It spreads from $R = 405$ mm to $R = 1$ m. The strip pitches are narrow bands of 24.1 mm or 48.2 mm length depending on the layer and 75.5 mm width. The more recent technology of ITk sensors has allowed to have 10 times the number of strip channels and 60 times the number of pixel channels with respect to the ID which lead to a total number of electronic channels of around 5 billion. It is designed to make at least 9 precision measurements per track.
To take into account the increased radiation exposure, the two first layers of the Pixel detector are expendables and will need to be replaced after the first HL-LHC Runs. The entire design of the detector, including the sensors but also the mechanical structure is meant to be as radiation proof as possible, notably to avoid radiation activation. Using light material allows to do this as well as limit the energy deposited by charged particles. The tracking performance achieved with ITk is detailed in the next section.

2.4.3 Tracking performance

The tracking strategy considered for ITk [2] is, for the time being, quite similar to the one currently used for Run 2 [103]. Seeds are formed from clusters of pixels and strips which are then used to look for track candidates with a Kalman filter algorithm. The search for track candidates can take into account the energy lost through bremsstrahlung if the charged particle is an electron or deposited in the layers if it's a pion. Finally, an Ambiguity Solving algorithm is run to assign clusters to tracks and solve the cases where multiple tracks are assigned to a cluster. The number of reconstructed tracks per bunch crossings increases linearly with the number of interaction which makes tracking combinatories more complex.
Tracks must also fulfill some quality requirements which are η dependant. They are listed in Table 2.1.

Requirements	Pseudorapidty interval		
	$\|\eta\| < 2.0$	$2.0 < \|\eta\| < 2.6$	$2.6 < \|\eta\| < 4.0$
pixel + strip hits	≥ 9	≥ 8	≥ 7
pixel hits	≥ 1	≥ 1	≥ 1
pixel + strip holes	≤ 2	≤ 2	≤ 2
p_T [MeV]	> 900	> 400	> 400
$\|d_0\|$ [mm]	≤ 2.0	≤ 2.0	≤ 10.0
$\|z_0$ [cm]	≤ 20.0	≤ 20.0	≤ 20.0

Table 2.1: Set of requirements applied during track reconstruction [2].

Tracking efficiency Tracking efficiency is assessed through simulated charged particles at different transverse momentum. For instance in Figure 2.13 the efficiency (i.e the fraction of tracks correctly reconstructed) is plotted as a function of the pseudorapidity η in $t\bar{t}$ samples that contain a lot of jets at a mean pile-up of 200.

The tracking efficiency maintains a comparable performance with respect to Run 2 in the region covered by both detectors with less than 5% decrease in efficiency. The fake track rate is 10^{-4} which is almost negligible.

Track parameter resolution Higher-level track parameter resolution with ITk can also be studied. Correctly evaluating them is crucial for multiple combined performance features like flavour tagging. Figure 2.15 shows the resolution of the transverse and longitudinal impact parameter d_0 and z_0. It is evaluated on a muon sample with 100 GeV transverse momentum and zero pile-up. The smaller pixel size especially in the innermost layers compared to the Inner Detector allows a resolution improvement by a factor 2 for d_0 and 4 for z_0.

Similarly, transverse momentum resolution is evaluated on the same sample in Figure 2.15 and shows a 30% increase in performance with respect to Run 2.

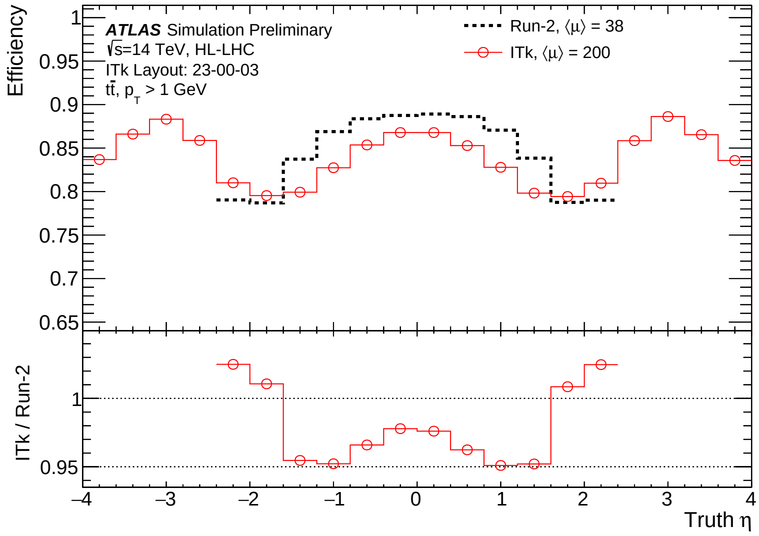

Figure 2.13: Tracking efficiency as a function of pseudorapidity in $t\bar{t}$ events with 200 pile-up with ITk (red) compared to Run 2 (black) [2].

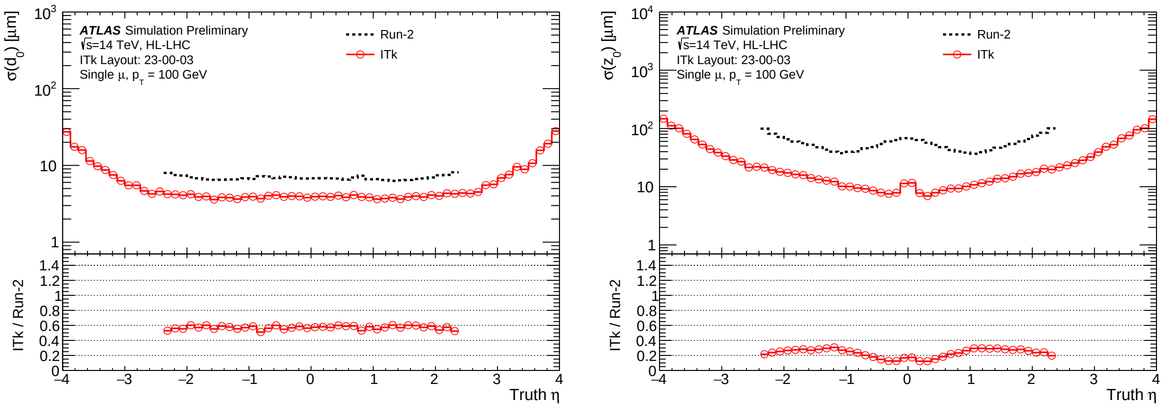

(a) (b)

Figure 2.14: Longitudinal and transverse impact parameter resolution as a function of pseudorapidity with ITk (red) compared to Run 2 (black) [2].

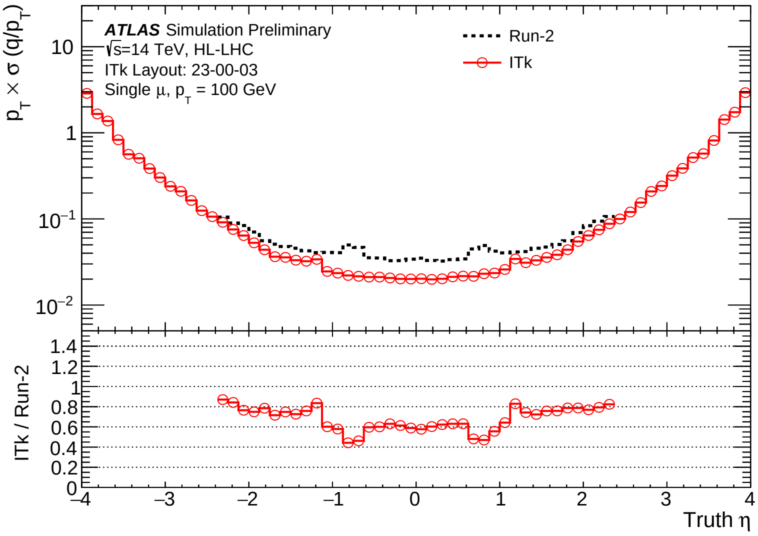

(a)

Figure 2.15: Relative p_T resolution as a function of pseudorapidity with ITk (red) compared to Run 2 (black) [2].

3 Adaptation of a neural network algorithm for jets flavour tagging at HL-LHC

Table of contents

Introduction

b quarks are key particles for various physics searches and measurements carried out by the ATLAS experiment. They are indeed Higgs boson's main decay channel as SM $H \to b\bar{b}$ branching ratio is 58%. The identification of these quarks has therefore a crucial importance for physics analyses related to Higgs boson, in particular for the potential observation of a pair of Higgs bosons, a process which is the priority of HL-LHC, and preliminary analysis of this measurement like the search for two BSM scalar bosons X and S in the channel $X \to SH \to b\bar{b}\gamma\gamma$ which is presented in this thesis.
The ATLAS detector will undergo a complete upgrade for the HL-LHC runs which should start in 2029. It is therefore crucial to study and assess the future performance of

the detector to characterise the future physics potential of ATLAS, and intend to increase or at least maintain current performance. In particular, flavour tagging will notably be impacted by a brand new inner detector (Inner Tracker – ITk) and also by much harsher conditions induced by HL-LHC, with for instance higher pile-up and a much more dense track environment. This chapter will present the work that has been done to adapt flavour tagging algorithms used in Run 2 to the latest HL-LHC simulations of the detector. These algorithms are introduced in Section 3.2 after a brief presentation of the key features and vocabulary of flavour tagging in Section 3.1. Section 3.3.1 will present the implementation of the DIPS algorithms while Sections 3.3.3 and 3.4 will show the performance reached by DIPS and other taggers specifically trained for HL-LHC.

3.1 Properties of b-hadrons

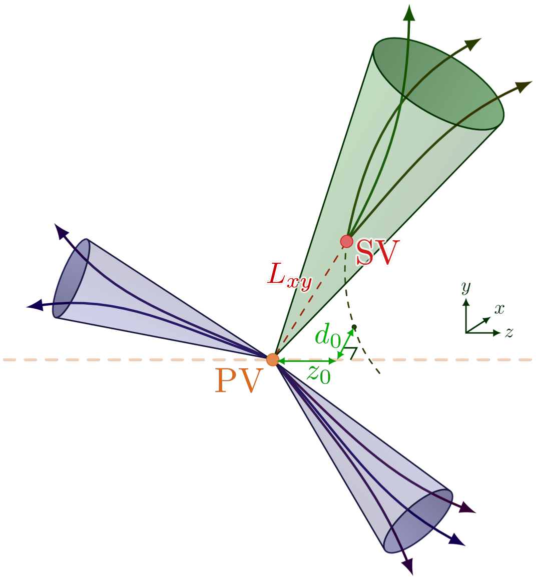

Figure 3.1: A sketch representing the differences between light and b-jets (the blue and green cones respectively) and illustrating the definition of the impact parameters d_0 and z_0. PV and SV are respectively the primary and secondary vertex and L_{xy} the distance between them.

Jets containing b quarks have distinctive characteristics that can be used to separate them from other jets, namely c-jets (containing c-hadrons but no b ones) and light jets (not containing any b or c-hadrons). First of all, b-hadrons have a relatively long lifetime ($\tau = 1.5$ ps) which means their mean transverse flight path is of the order of $L_{xy} = \beta\gamma c\tau = 4$ mm away from the primary vertex (PV) of the event. This is sometimes enough to experimentally identify a so-called secondary vertex (SV) where the b-hadron decays, as the current innermost layer of the inner detector (IBL) is located at a distance $R = 33.25$ mm from the beam. Consequently, tracks coming from this secondary vertex will have a higher impact parameter (IP), defined as the distance of closest approach from the reconstructed track to the PV, than tracks coming from the PV (see Figure 3.1). We can define as well the transverse impact parameter d_0, which is the projection of the IP in the plane transverse to the beam axis, and the longitudinal impact parameter z_0 which is the z-coordinate difference between the PV and the point of closest approach. These two features are exploited by b-tagging algorithms as we will see in the next section.

3.2 Flavour Tagging in ATLAS

ATLAS flavour tagging strategy uses a two level structure of algorithms. The first "low level" algorithms use basic information from the jets like the tracks impact parameter or the vertices to make preliminary predictions, and the second "high level" algorithms are using and combining outputs from the first level to make the final jet tagging prediction. GN1 [133], however, the latest flavour tagging algorithm developed in ATLAS, does not follow this pattern and is a single algorithm combining all information to directly make the tagging prediction.

3.2.1 Low level algorithms

The low level algorithms are based on two families : impact parameter (IP) and secondary vertex (SV) taggers.

3.2.1.1 IP based algorithm

The first type of algorithm, as suggested by its name, is using the impact parameter and its significance (the IP of a track divided by its uncertainty) as a primary source of discrimination between b-jets and light and c-jets. Figure 3.2 illustrates how different are transverse and longitudinal impact parameter distributions depending on the jets flavour. The tail of the b-jets track distribution is larger than the ones from light and c jets as tracks originating from b hadrons tend to have large impact parameters.

IP3D IP3D [134] is an IP-based algorithm developed for LHC Run 2. For each track, the IP significance $s_{d_0} = d_0/\sigma_{d_0}$ or $s_{z_0} = z_0 sin\theta/\sigma_{z_0 sin\theta}$ is compared to predetermined PDF (probability density function) templates based on simulation. There are different template categories depending of the number of hits of the track in the different layers of the inner detector, which is an indicator of the track quality. The template comparison assigns probabilities p_l and p_b for the track to belong to a light or a b-jet respectively. At the jet level, the final discriminant is the sum of the log-likelihood ratio of the different tracks contribution :

$$D_{\mathrm{IP3D}} = \sum_{\mathrm{tracks}} \log \frac{p_b}{p_l} \tag{3.1}$$

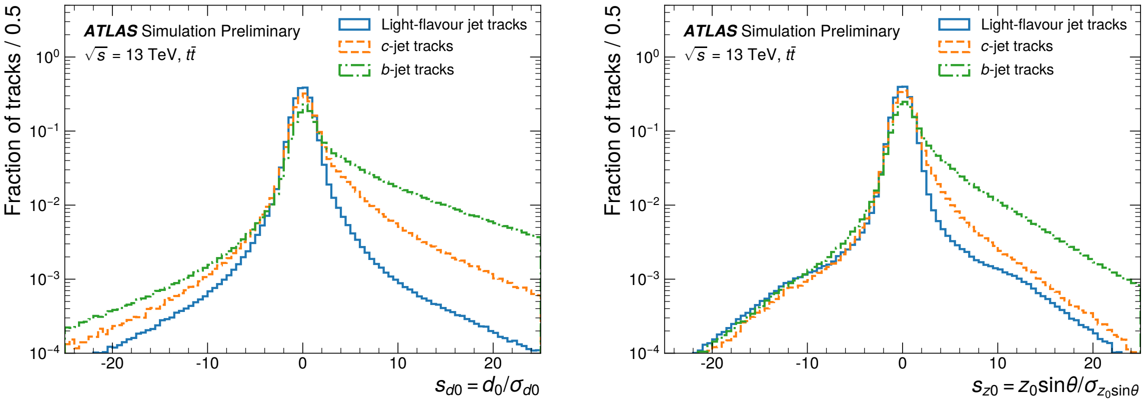

Figure 3.2: Transverse (left) and longitudinal (right) IP significances for b-jets, c-jets and light-flavour jets in $t\bar{t}$ events. The sign of the track IP is indicating if it is in front of or behind the PV with respect to the jet direction [1].

.

Other discriminants are similarly defined to separate b-jets from c-jets or c-jets from light jets. IP3D underwent a complete reoptimisation for upgrade [2] and will be used as a point of reference in the following sections.

RNNIP New algorithms development have been made in the past years to refine the b-jet discrimination, notably using machine learning techniques which allow to take into account correlations between tracks inside a jet. RNNIP [135] is the first IP based algorithm developed by ATLAS which uses machine learning. It is using a recurrent neural network and is capable of taking into account correlations between tracks, something that was a blind spot with IP3D. Indeed, in a jet, if one track has a large impact parameter, then it is more likely to find another track with also a large IP. The recurrent neural network is able to tackle this challenge by learning these dependencies inside sequences of tracks signed transverse and longitudinal IP significances but also other tracks information such as the fraction of the jet transverse momentum carried by the track p_T^{frac}, the angular distance between the track and the jet-axis (ΔR) or the hit multiplicity of the track in the different layers of the inner detector. The network output are probabilities p_b, p_c and p_l for the jet to be a b, c or light jet respectively. The final discriminant for b-tagging is given by :

$$D_{\text{RNNIP}} = \log \frac{p_b}{(1-f_c)p_l + f_c p_c} \tag{3.2}$$

where f_c is a free parameter which balances the c-jets and light jets rejection and chosen as a compromise between them.

DIPS DIPS (Deep Impact Parameter Sets) [1] is the latest-to-date ATLAS IP based algorithm and it consists in a neural network with a deep set based architecture. It uses track IP significance, kinematics, and the number of hits in the silicon detectors as features - the full list of tracks training features is shown in Table 3.1. As illustrated in Figure 3.3, a first neural network ϕ is applied for each track in the jet and then the output is summed and given as an input to a feed forward neural network F. To put this in a more formal way, if p_{track} is the vector of the tracks input, the overall output is given by :

$$\mathscr{O}(\{p_b, p_c, p_l\}) = F(\sum_{\text{tracks}} \Phi(p_{\text{track}})) \tag{3.3}$$

where $\mathscr{O}(\{p_b, p_c, p_l\})$ are the output class probabilities.

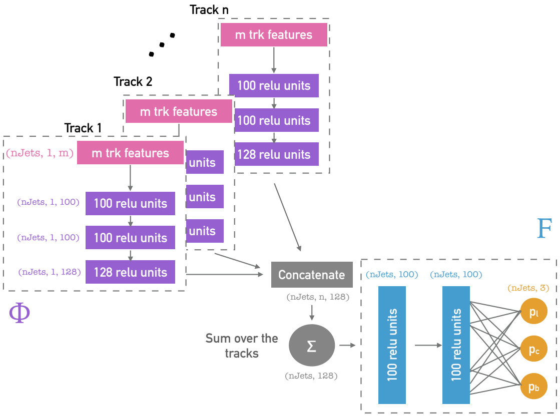

Figure 3.3: Architecture of the DIPS algorithm. The number of hidden units in the different neural network layers doesn't correspond to the latest-to-date optimisation [1].

Similarly to RNNIP, the discriminant for b-tagging is given by :

$$D_{\text{DIPS}} = \log \frac{p_b}{(1-f_c)p_l + f_c p_c} \tag{3.4}$$

DIPS allows for faster training and better performance with respect to RNNIP [1] due to the permutation invariance of the tracks inside a jet. A more complete presentation of DIPS implementation for the upgraded ATLAS detector is included in Subsection 3.3.1.

3.2.1.2 SV based algorithm

The secondary vertex based algorithms family aims at explicitly reconstructing displaced vertices from heavy hadrons. The SV1 algorithm [136] focuses on finding a secondary vertex separated in space from the primary vertex and which might be the sign of a long-lived b-hadron. JetFitter [137] is a topological multi-vertex finding algorithm which tries to reconstruct the full b-hadron decay chain by exploiting the topological structure

Input	Description
s_{d0}	d_0 / σ_{d0} : Transverse IP significance
s_{z0}	z_0 sin θ/ $\sigma_{z0 sin\theta}$: Longitudinal IP significance
log p_T^{frac}	log p_T^{track}/p_T^{jet} : Logarithm of fraction of the jet p_T carried by the track
log ΔR	Logarithm of opening angle between the track and the jet axis
IBL hits	Number of hits in the IBL: could be 0, 1, or 2
PIX1 hits	Number of hits in the next-to-innermost pixel layer : could be 0, 1, or 2
shared IBL hits	Number of shared hits in the IBL
split IBL hits	Number of split hits in the IBL
nPixHits	Combined number of hits in the pixel layers
shared pixel hits	Number of shared hits in the pixel layers
split pixel hits	Number of split hits in the pixel layers
nSCTHits	Combined number of hits in the SCT layers
shared SCT hits	Number of shared hits in the SCT layers

Table 3.1: Track features used as inputs for DIPS.

of the b and c-hadron decays. Like the IP based algorithms, they are intended to serve as inputs for "high level" algorithms presented in the next section.

3.2.2 High level algorithms

MV2 MV2 [138] is a Boosted Decision Tree (BDT) which combines inputs from IP3D, SV1, JetFitter and also kinematic variables like the jet p_T and η. A version of MV2 named MV2c10 has been retrained (on $t\bar{t}$ samples only) for upgrade studies and is used as a baseline to compare the performance of other high level algorithms.

DL1 series The DL1 series of algorithms [138] are based on deep-learning classifiers using fully connected multi-layer feed-forward neural networks which combine inputs of low-level algorithms. The kinematic properties of the jets, namely p_T and $|\eta|$, are also included in the training of the network in order to take advantage of the correlations with the other input variables. A procedure called resampling is applied to have the jets in the training sample uniformly distributed in p_T and $|\eta|$ for each flavour class so that the flavour tagging discriminating power is as independent as possible from the kinematics. The resampling procedure is similar to the one done for DIPS and described in more details in 3.3.1.2.
The DL1 series is composed of 3 different algorithms depending on what input low level algorithms are included :

- DL1 takes SV1, JetFitter and IP3D as inputs.
- DL1r uses RNNIP on top of the first three ones.
- DL1d replaces RNNIP with DIPS.

Different taggers are currently used in ATLAS analyses : DL1r is used in Run 2 analyses using ATLAS software release 21 while other Run 2 analyses reprocessed in release 22 are using either DL1d or GN1. The overall structure of the two latest algorithms of the DL1 series is summed up in Figure 3.4.

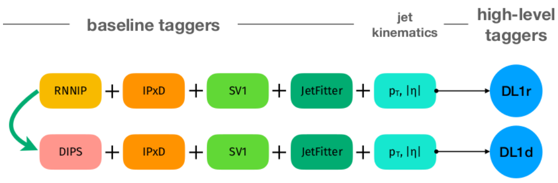

Figure 3.4: General structure of the DL1r and DL1d high level b-tagging algorithms.

3.2.3 GN1

GN1 [133] is a machine learning flavour tagging algorithm using a graph neural network. A particularity of GN1 is that the network has other training objectives in addition to the standard jet flavour prediction. These objectives aim at understanding the true internal structure of the jet by grouping the tracks into vertices and by telling which process produced each of the track observed in the jet. As such, the additional training objectives help the main flavour tagging one and improve overall performance.

GN1 takes as input the same tracks information as RNNIP and DIPS, as well as the jet kinetic variables (p_T and η). The graph structure of the neural network is particularly adapted to reconstruct the inner structure of the jet which can be understood as a graph itself with tracks being the edges and particles vertices corresponding to the vertices of the graph.

As this will be detailed in the next paragraph, GN1 is superseding the performance achieved with the traditional high-level ATLAS flavour tagging algorithms [133].

3.2.4 Flavour tagging performance in Run 2

This section details the performance obtained with some of the algorithms described in the previous section in the context of Run 2 ATLAS as they are part of the analysis presented in this thesis.

Flavour tagging performance quantification The output of a tagger is a b-tagging discriminant distribution. A common tool to evaluate the quality of a tagger is the Receiver Operating Characteristic (or ROC) curve. A cut-value τ on the discriminant distribution is chosen and all jets with a discriminant score above this cut are tagged as b-jets while all jets with a score below τ are rejected. The ROC curve consists in a curve displaying the light or c-jets rejection against the b-tagging efficiency ε_b (the probability of a true b-jet to pass the selection cut) parametrised by this cut parameter τ. Finally, ATLAS analyses are using different working points (WP) for which the tagger is calibrated. A working point consists in a given b-jet efficiency point which corresponds to a given discriminant cut. Improving the quality of a tagger at a working point therefore means improving the light and c-jets rejection for a constant b-jet efficiency. Most usual working points are 60%, 70%, 77 % and 85% b-jet efficiency with 60% being the tightest selection.

To look for b-quarks in the final state is exposing one self to a QCD driven background composed of a large number of jets, with only a small fraction of them being b-jets due to the relatively large mass of the b-quark making their production rate much lower. In the $\gamma\gamma$+jets background from the $SH \rightarrow b\bar{b}\gamma\gamma$ analysis, the proportion of 2 b-jets is for instance less than 1%.

This small proportion of b-jets forces tagging algorithms to reach high levels of rejection as even a small number of mistagged light or c-jets would mean a significant signal contamination. For the 77% b-jet selection efficiency ε_b which is used in the SH analysis, b-tagging algorithms usually reach light jet rejection of around 100 and c-jet rejection of 5, which means that one light (respectively c) jet over 100 (5) will be mistagged as a b-jet and potentially contaminate a signal selection in an analysis. Low level and high level algorithms performance are shown in Figure 3.5 and 3.7 respectively. The pile-up conditions in Run 2 are close to $\langle\mu\rangle = 40$ average number of interactions per bunch crossing.

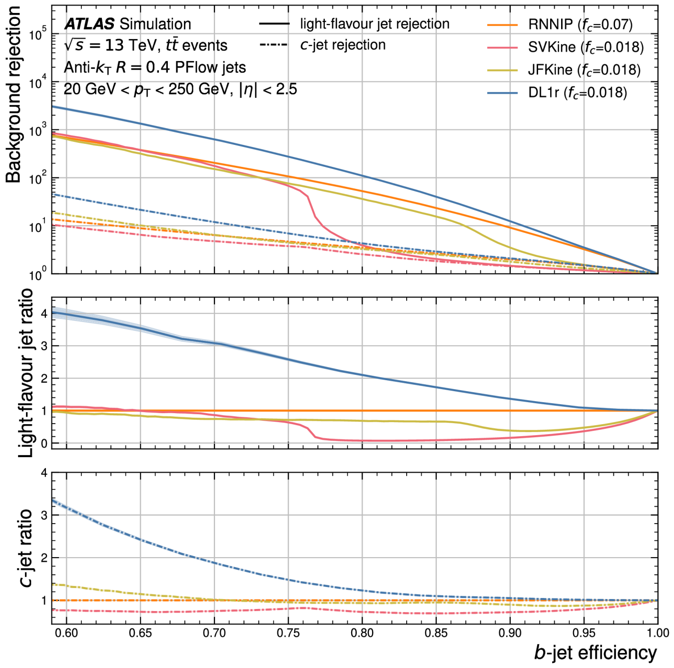

Figure 3.5: The light-flavour jet and c-jet rejection factors as a function of b-jet efficiency ε_b for DL1r as well as the low-level taggers RNNIP, SVKine (a version of SV1) and JFKine (a version of JetFitter). The lower two panels show the ratio of the light-flavour jet rejection and the c-jet rejection of the algorithms to RNNIP [139].

The complementarity of the low level algorithms is illustrated in Figure 3.5. In particular the SV1 and JetFitter algorithms have really poor performance for high b-jet efficiency because their secondary vertex finding efficiencies are of approximately 80% and 90% respectively. In compensation, the IP algorithms like RNNIP have a good performance in this region (and overall better performance than SV1 and JetFitter). The improvement of performance of the high level algorithms can be seen with the DL1r curve which has a performance roughly twice as good as the best low level algorithm.

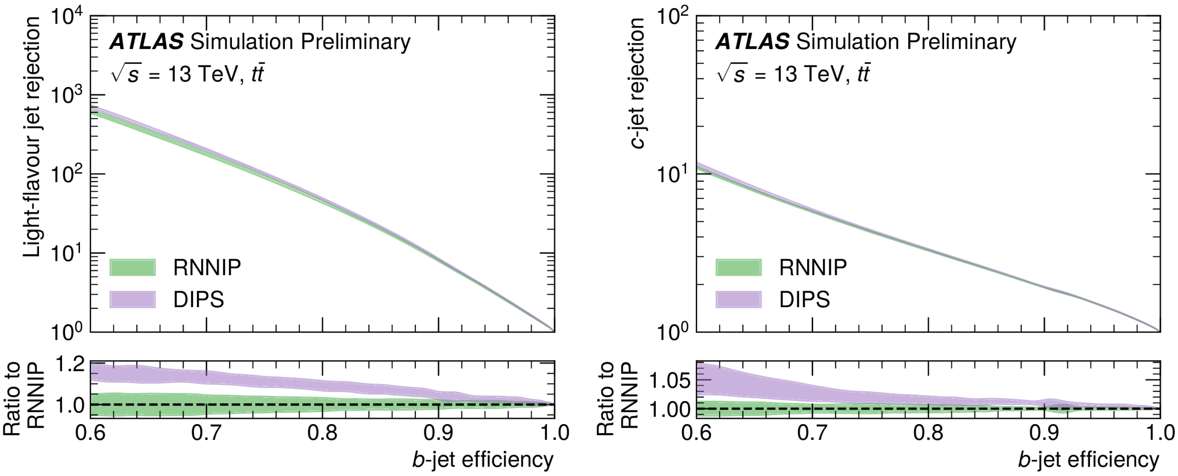

Figure 3.6: Light-flavour jet rejection (left) and c-jet rejection as a function of ε_b (right) for the RNNIP and DIPS algorithms. The error band corresponds to the standard deviation of the rejection between 5 different trainings [1].

Inside the low level algorithms, the evolution and improvement of the structure of the taggers led to an increase of performance over time. This can be seen with the improve of performance of DIPS with respect to RNNIP, which can reach 20% for light jet rejection and 5% for c-jet, as illustrated in Figure 3.6.

Similarly, the progressive amelioration of high level algorithms performance, which was made possible by switching from a BDT to a deep set neural network and also benefits from the better low level input performance is clearly visible in Figure 3.7.
The latest developed algorithm for flavour tagging in ATLAS, GN1, is not a high-level algorithm but rather a all-in-one algorithm that is made to provide the final tagging prediction, therefore its performance can be compared to other high level taggers.

The ROC curves from Figure 3.8 show that GN1 is overperforming the best high level algorithm available at the time. Light jet and c-jet rejection is increased by a factor of at least 2 at a given b-tagging efficiency of 70% and GN1 Lep, a variant of GN1 including an additional track-level input which indicates if the track was used in the reconstruction of an electron, a muon or neither, is showing even more rejection improvement.
These impressive results are not an end in themselves as the graph neural network architecture for flavour tagging is relatively new and has not reach its full potential yet. New features and global upgrades to GN1 are currently under development. GN1 or

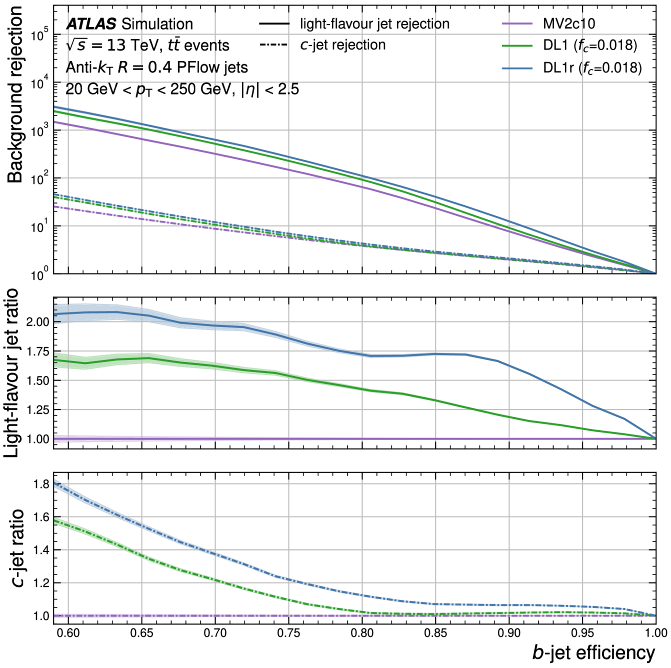

Figure 3.7: The light-flavour jet and b-jet rejection factors as a function of ε_b for the high level taggers MV2c10, DL1 and DL1r. The ratio plots are made with respect to MV2c10 [139].

similar improved versions will most likely be used to reprocess Run 2 data and for Run 3 and future upgrade performance.

Finally, it can be useful to study the performance as a function of kinematic parameters such as the jets p_T. The dependency on p_T will for instance modify the signal selection of the SH analysis as a function of the mass of S . Figure 3.9 shows the light jet rejection as a function of the jet pt for an inclusive b-tagging efficiency of 77%. The performance follows a bell shape, reaching its maximum around 150 GeV and then decreasing again for high p_T jets with a sudden drop in rejection at $p_T \approx 175$ GeV $\approx m_{top}$ mainly due to the overlap of decay products from boosted top-quark decays.

3.3 DIPS training for ITk

This section presents the work that has been done to adapt the low level b-tagging algorithm DIPS in the context of the upgraded inner detector ITk. Previous studies about b-tagging with ITk focused on the more basic IP3D and SV1 algorithms [2]. Final results, including the integration of DIPS in the high level tagger DL1d and the comparison to the GN1 algorithm are presented in Section 3.4 as based of the works from [3].

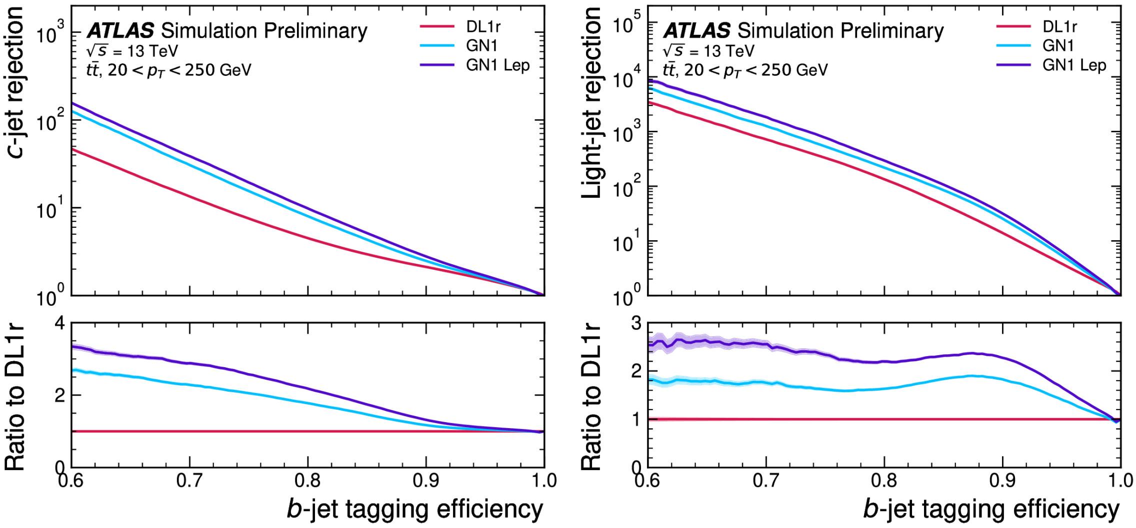

Figure 3.8: Light-flavour jet and c-jet rejection factors as a function of ε_b in the $t\bar{t}$ sample for GN1 and GN1 Lep [133]. Performance is compared to DL1r, the reference high level tagger for Run 2.

3.3.1 Training

3.3.1.1 Samples and physics objects selections

Samples The samples used to train and evaluate DIPS are constituted of simulated $t\bar{t}$ and Z' [1] events produced in the proton-proton collisions at a centre of mass energy of $\sqrt{s} = 14$ TeV which is the targeted centre-of-mass energy for HL-LHC. The association of both $t\bar{t}$ and Z' is done to provide enough statistics in a large range of p_T. The $t\bar{t}$ sample is generated at next-to-leading order in the strong coupling constant αs using Powheg Box and the events are interfaced to the Pythia8 parton shower model with the A14 set of tuned parameters. The Z' sample is generated with Pythia8 with the same tune and PDF set. Finally, the EvtGen 1.2.0 program is used for the simulation of the b and c-hadron decays. Samples are generated with an average number of interactions per bunch crossing of $\langle\mu\rangle = 200$, corresponding to the maximal pile-up expected during HL-LHC. The interaction of the particles with the detector are simulated with the full ATLAS detector simulation which is based on Geant4. The latest version of the ITk geometry, labelled as 23-00-03 [2], is used in these simulations.

Object selection The most important objects used in jet flavour tagging algorithms are tracks and jets.

The tracks selection is presented in Table 3.2. The selection mainly consists in general track quality selection dedicated for ITk [2] as the tracks are required to have a sufficient

---

[1] Z' is an hypothetical BSM particle which is used to provide a sufficient and relatively flat high p_T distribution up to 5 TeV thanks to its large mass. Its branching ratios are arbitrary set to identical values for decays into b, c and light-jets.

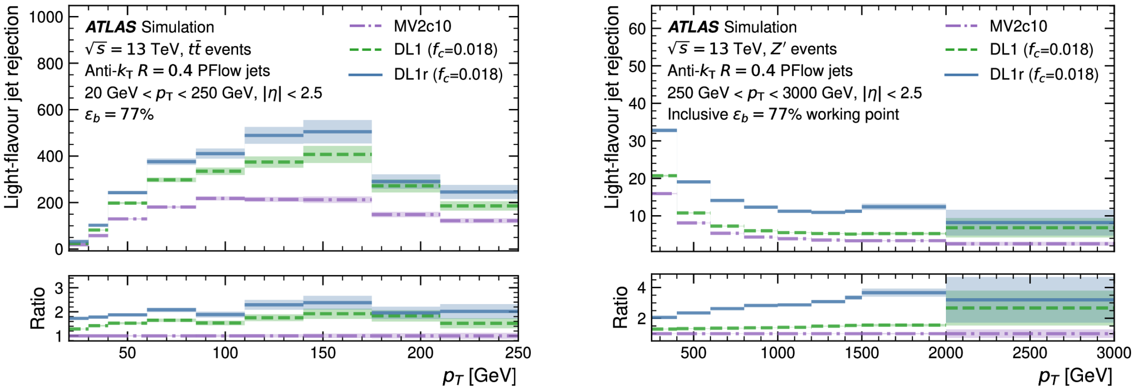

Figure 3.9: High level taggers light-flavour jet rejection at a fixed b-tagging efficiency as a function of jet p_T in low (left) and high (right) p_T regions . In each bin, the b-tagging efficiency is set to 77%, and the resulting background rejection is shown.

number of hits in the different layers and a low number of holes (i.e a missing measurement on a track where a hit would be expected). These quality criteria are depending on η as expected with the larger pseudo-rapidity coverage of ITk and the differences in the amount of material between the regions of the detector. In addition, some flavour tagging specific cuts on transverse and longitudinal impact parameters are applied to reduce contamination from pile-up events tracks. A Loose and a Tight tracks selections are defined and their impact on the flavour tagging performance will be compared in Subsection 3.3.2.2. The criteria on impact parameter ($d0$ and $z0$) values to define these selections are the same as the ones from Run 2.

Jets are reconstructed from clustering energy deposits in the calorimeter with the anti-k_T [112] algorithm with a radius parameter $\Delta R = 0.4$. A selection is applied to keep only jets with $p_T > 20$ GeV and $|\eta| < 4$. An overlap removal with electrons or muons originating from W bosons decay (called lepton veto) using truth information from the simulation is also applied to prevent isolated leptons to be reconstructed as light-jets. As the JVT (Jet Vertex Tagger) algorithm used to remove jets originating from pile-up is not implemented yet for upgrade studies, a truth jet matching is applied instead. It consists in selecting reconstructed jets only if the angular distance ΔR to a truth jet is below 0.3. Finally, the reconstructed primary vertex is required to be less than 0.1 mm along the longitudinal direction away from the true PV of the event in order to discard events with badly reconstructed PV.

Tracks-jets association is made with a matching criteria which is p_T dependent as the boosted jets with higher p_T have a narrower angular opening. The cone size is ranging from $\Delta R = 0.45$ for jets with $p_T = 20$ GeV to $\Delta R = 0.25$ for jets with $p_T > 200$ GeV. The truth jet labelling which is used for the evaluation or the selection as described earlier is based on the presence of a generator-level b or c-hadron or τ hadronic decay products, as there is a fourth category for jets originating from τ leptons which decay hadronically.

Requirements	**Tight tracks selection**		
	$\lvert\eta\rvert < 2.0$	$2.0 < \lvert\eta\rvert < 2.6$	$2.6 < \lvert\eta\rvert < 4.0$
pixel + strip hits	≥ 9	≥ 8	≥ 7
pixel hits	≥ 1	≥ 1	≥ 1
pixel + strip holes	≤ 2	≤ 2	≤ 2
p_T [MeV]	> 1000	> 1000	> 1000
$\lvert d_0\rvert$ [mm]	≤ 1.0	≤ 1.0	≤ 1.0
$\lvert z_0 \sin\theta\rvert$ [mm]	≤ 1.5	≤ 1.5	≤ 1.5

Requirements	**Loose tracks selection**		
	$\lvert\eta\rvert < 2.0$	$2.0 < \lvert\eta\rvert < 2.6$	$2.6 < \lvert\eta\rvert < 4.0$
pixel + strip hits	≥ 9	≥ 8	≥ 7
pixel hits	≥ 1	≥ 1	≥ 1
pixel + strip holes	≤ 2	≤ 2	≤ 2
p_T [MeV]	> 900	> 500	> 500
$\lvert d_0\rvert$ [mm]	≤ 2.0	≤ 2.0	≤ 3.5
$\lvert z_0 \sin\theta\rvert$ [mm]	≤ 5.0	≤ 5.0	≤ 5.0

Table 3.2: Tight (top) and Loose (bottom) selection of jet tracks used by DIPS.

If a b-hadron with $p_T > 5$ GeV is found within $\Delta R < 0.3$, the jet is labelled as a b-jet, otherwise the procedure is repeated for c-hadron and τ hadronic decay products and in the end the remaining jets are labelled as light jets.

3.3.1.2 DIPS training and evaluation

While the transition of the HL-LHC studies to the more recent ATLAS software release 22 (and above) is ongoing, training and evaluation of DIPS had to be made with release 21.9 simulation samples which were the only ones available at the time. Some technical adaptation was required to be able to run these upgrade samples with the standard ATLAS tools for training and evaluating neural network models used for current Run 2 studies. A framework named the Training Dataset Dumper is used to convert the simulation samples to the hdf5 format which is standard for neural network development. The different tracks and jets selection described in the previous section are also applied at this stage. The preprocessing, training and evaluation steps are performed in another framework called Umami [140].
To ensure that the new upgrade framework leads to the same object selection as the previous upgrade studies, a comparison is done between the output of the Training Dataset Dumper and the previous framework. We assure that the distribution of p_T and η, for instance, are identical (Figure 3.10).

Tracks features list is presented in Table 3.3 and required some minor adaptation with respect to the Run 2 list because the layers label of the current ATLAS inner detector must be changed to their ITk counterpart.

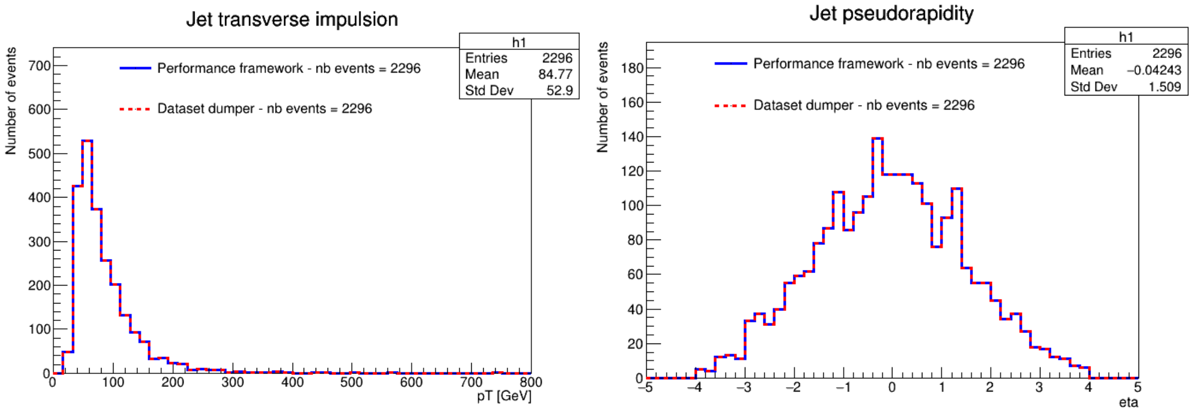

Figure 3.10: Distribution of DIPS jets inputs p_T (left) and η (right) after current (red) and previous (blue) upgrade studies selection.

Training sample DIPS training, validation and evaluation sets are made by using jets from the $t\bar{t}$ and Z' samples mentioned in 3.3.1 to form so-called *hybrid samples*. Jets above 250 GeV are taken from the Z' sample while those below 250 GeV come from from the $t\bar{t}$ sample. The global composition of the sample is 70% of jets (resp. 30%) coming from the $t\bar{t}$ (Z'). However these samples cannot be used directly as they are highly unbalanced in their flavour composition which could bias the training. A procedure called resampling must be applied first to form a set with equal proportions of b, c and light jets. Two resampling procedure have been studied for the training set of upgrade DIPS :

- The first method is called **undersampling** and it consists in removing random jets from the majority tagging class (the light jets) until it matches the number of jets in the minority class (most of the time c-jets)
- The second method is called **pdf sampling**. It requires to fix a target number of jets per class and samples above this target are downsampled whereas samples below are upsampled which means that some jets of the minority class are copied until the target is reached.

In order to ensure an kinematic-independent tagging of the jets, this resampling procedure is applied in 2D bins of p_T and η. The impact of the two procedure on the training and the performance of DIPS is compared in Subsection 3.3.2.1. In addition to this resampling step, the preprocessing of the training set also includes a scaling and shifting step where all the training features of the training jets are scaled and shifted to obtain values between 0 and 1 which is a common procedure in machine learning. The validation and evaluation sets, which are composed of 3.6 million jets each, do not undergo this resampling step. For $t\bar{t}$, the evaluation sample is issued from another sample on which a version of the MV2c10 tagger retrained for upgrade is available for comparison. For Z', the evaluation sample is obtained from the same set as the training jets as MV2c10 have not been

Track Input	**Description**
s_{d0}	d_0 / σ_{d0} : Lifetime signed transverse IP significance
s_{z0}	z_0 sin θ/ $\sigma_{z0 sin\theta}$: Lifetime signed longitudinal IP significance
$\log p_T^{frac}$	$\log p_T^{track} / p_T^{jet}$: Log of fraction of the jet p_T carried by the track
$\log \Delta R$	Log of opening angle between the track and the jet axis
nInnermostPixHits	Number of hits from the innermost pixel layer
nNextToInnermostPixHits	Number of hits in the next-to-innermost pixel layer
nInnermostPixShared	Number of shared hits from the innermost pixel layer
nInnermostPixSplit	Number of split hits in the innermost pixel layer
nPixHits	Number of pixel hits
nPixShared	Number of shared pixel hits
nPixSplit	Number of split pixel hits
nStripHits	Number of strip hits
nStripShared	Number of shared strip hits

Table 3.3: Track features used as inputs for HL-LHC DIPS [3].

retrained on a Z' sample.

Training takes place with 15 million jets when the resampling is done with the pdf method and 3 million when it's with the undersampling method. It should be noted that due to the limited size of the upgrade samples, it is a bit less than the DIPS algorithm presented in [1] and far less than the current best optimization of DIPS for Run 2 at the time of the analysis which is trained with 80 million jets. Hence one can expect a future improvement in performance with an increasing number of training jets.

The neural network is using a learning rate (the step size used when making the gradient descent) of 10^{-3} and the batch size is 15000 (the number of jets used to calculate the gradient at each step).

The training is studied through two different metrics : accuracy and loss. The *accuracy* is the fraction of jets which are correctly tagged while *loss* evaluates how jets are mistagged using cross entropy. They can either be evaluated on the training or on the validation set. The comparison between both performance can be useful to spot potential overtraining. Examples of the metrics of the different training are presented in Figure 3.11 and 3.12.

In general, training convergence is longer than Run 2 DIPS where it took less than 100 epochs. After damped oscillations, convergence seems to be reached after around 350 epochs for the undersampling training whereas for the pdf training the performance seems to constantly oscillate after quickly reaching a plateau at around 50 epochs. In any case, both trainings are evaluated at epoch 400 where they have all converged.

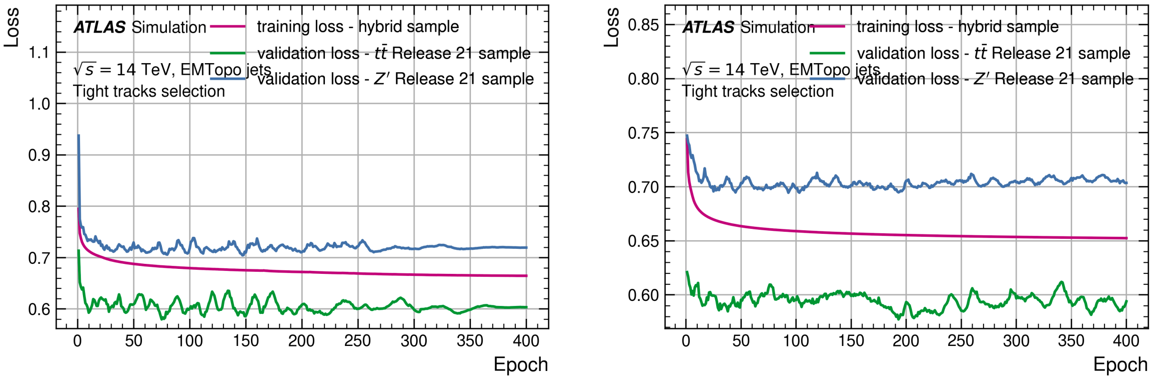

Figure 3.11: Training (purple) and validation loss on $t\bar{t}$ (green) and Z' (blue) sample for undersampling (left) and pdf (right) trainings. The training and validation loss are evaluating the errors of the network on the training and validation set respectively.

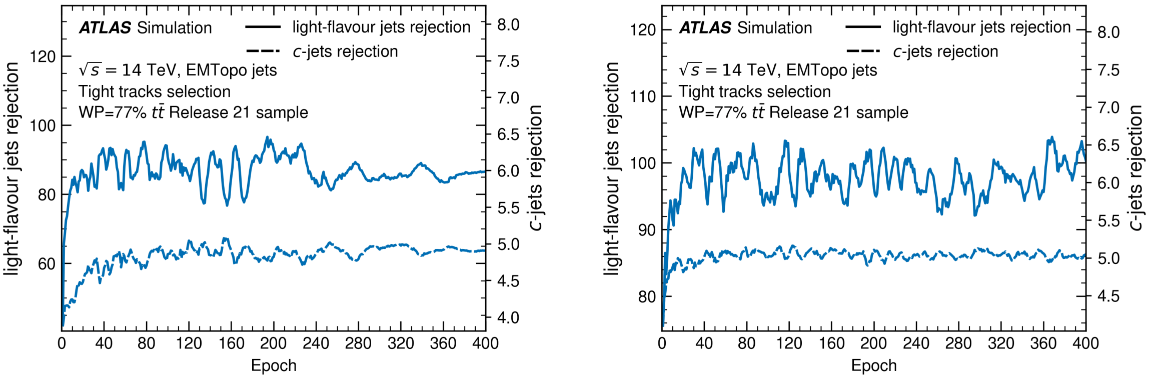

Figure 3.12: Training and validation rejection for undersampling (left) and pdf (right) trainings. The light jet (plain line) and c-jet (dashed line) rejection are evaluated on the $t\bar{t}$ sample validation set at a b-tagging efficiency working point of 77%.

3.3.2 Optimisation studies

3.3.2.1 Resampling methods

The different resampling methods influence the number of jets in the training sample. Initially, after saving the jets of the validation and evaluation sets, the flavour composition of the training samples is shown in Table 3.4.

For the undersampling method (also named *count*), the number of jets in the training sample is limited by the less numerous flavour in a sample in proportion with the $t\bar{t}$ and Z' division of 70-30%. In our case, it's the $t\bar{t}$ c-jets number which is the limitating factor.

With the pdf resampling method, we can make a better use of the jets that we have

Flavour	$t\bar{t}$	Z'	Total
b-jets	4.1M	650k	4.8M
c-jets	755k	700k	1.5M
light jets	4.9M	1.1M	6M

Table 3.4: Number of jets of different flavour in the training set before preprocessing. There is significantly less c-jets than other flavours.

Undersampling			
Flavour	$t\bar{t}$	Z'	Total
b-jets	755k	323k	1.07M
c-jets	755k	323k	1.07M
light jets	755k	323k	1.07M
			3.2M

pdf			
Flavour	$t\bar{t}$	Z'	Total
b-jets	3.5M	1.5M	5M
c-jets	3.5M	1.5M	5M
light jets	3.5M	1.5M	5M
			15M

Table 3.5: Number of jets of different flavour in the training set with the undersampling/count method (left) and the pdf method (right).

at our disposal at the cost of copying some jets from the less common flavours. A compromise target value of 5 million jets per class is set. The training set flavour composition for both pdf and undersampling is given in Table 3.5.

The ratio of the number of jets of different flavours effectively included in the training set over the available number of jets of the same flavour is shown in Table 3.6. The maximum upsampling ratio (i.e the maximum number of time a c-jet can be copied) is checked to be under 5 to avoid too much copying which could impact the performance.

Undersampling		
Flavour	$t\bar{t}$	Z'
b-jets	0.18	0.49
c-jets	1	0.46
light jets	0.15	0.28

pdf		
Flavour	$t\bar{t}$	Z'
b-jets	0.85	2.28
c-jets	4.64	2.14
light jets	0.72	1.30

Table 3.6: Ratio of the jet number of different flavour included in the training set over the total available number for this flavour with the undersampling (left) and pdf methods (right)

The undersampling and pdf resampling methods performance are compared in Figure 3.14, along with the study on tracks selection. Trainings with undersampling method are using a feature called learning rate reducer which, as suggested by its name, reduce the learning rate of the training if a performance plateau is reached. Trainings using pdf resampling method are not using the learning rate reducer as it didn't provide any performance improvement.

The pdf resampling method always gives better performance except for the c-jet rejection in the $t\bar{t}$ evaluation sample where performance is similar. Overall, pdf resampling method is the best and is the method chosen to train upgrade DIPS.

3.3.2.2 Tracks selection

The tracks selection is a key parameter for b-tagging as it controls which information are used by the tagger network to make the discrimination between jets flavour. The selection criteria on the transverse and longitudinal IP are meant to reduce contamination on pile-up tracks but they also remove some tracks coming from heavy flavoured hadrons decays. The ability of a neural network to find correlations between a large set of information allowed for the looser tracks selection to provide better results for Run 2 DIPS tagger [1]. The number of tracks per jet with the two selections is compared in Figure 3.13. Up to 40 tracks per jet can be saved and used for flavour tagging even though the mean number of tracks per jet is around 7.

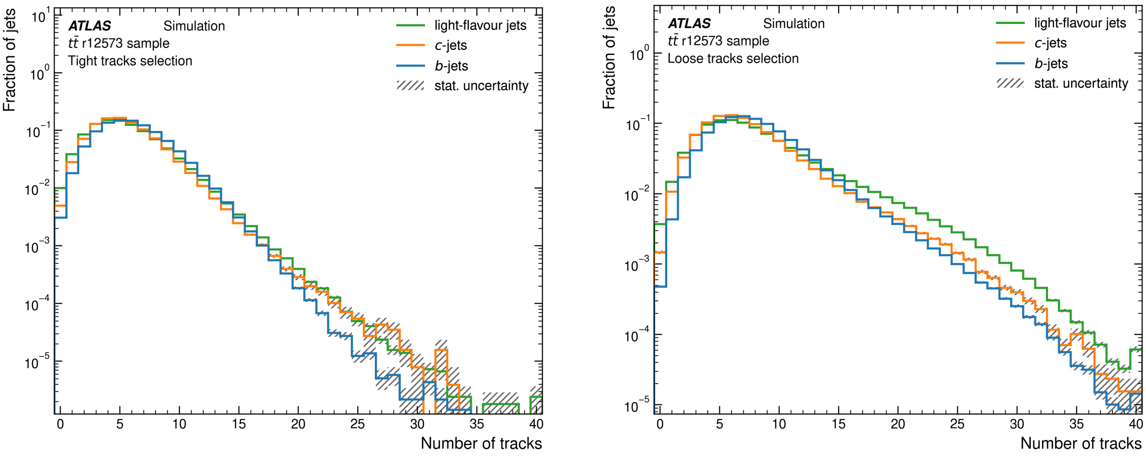

Figure 3.13: Distribution of the number of tracks per jet in the $t\bar{t}$ training sample with the Tight (left) and Loose (right) selections.

The Loose tracks selection training is clearly overperforming the Tight selection training with both resampling method as shown in Figure 3.14 with a gain in light and c-jet rejection of at least 20% at the 77% b-jet efficiency working point.

Figure 3.15 presents fraction scan plots that show the light and c-jet rejection curves parameterised by the parameter f_c from the tagging discriminant definition at a given b-tagging efficiency. The plots confirm this result with the DIPS training with pdf resampling and Loose tracks selection providing better performance than the other trainings for all values of f_c. The value of $f_c = 0.17$ is taken as it optimizes both rejections in the $t\bar{t}$ evaluation set and gives an acceptable balance in the Z' one for a b-tagging efficiency of 77%.

3.3.3 Final DIPS performance with ITk

After selecting the upgrade DIPS training with pdf resampling method and using Loose tracks selection which yields to the best results and selecting the value of the f_c parameter which provides best balance of performance between c and light jet rejection, its performance can be studied and compared to other taggers.

First of all, DIPS performance is compared to the other taggers that had been trained and optimized with the upgrade ITk configuration, namely IP3D and MV2 [2] in Figure 3.16. The performance can only be compared on $t\bar{t}$ events since other taggers have not been retrained on a Z' sample.

DIPS is outperforming IP3D as it was expected from the Run 2 results and the improvements coming from the neural network. Even though MV2 is a high level tagger, DIPS manages to provide better c-jet rejection despite having significantly lower light jet rejection.

The evaluation of performance as a function of the pseudorapidity η is an interesting metric to look at, especially in the context of ITk which provides an extension on the angular coverage (up to $|\eta| < 4$) with respect to the current inner detector ($|\eta| < 2.5$). The light-jet rejection ROC curves of upgrade DIPS in different η bins is shown in Figure 3.17. The overall performance in the $|\eta| < 2.5$ region is also displayed and compared to the Run 2 performance. However it must be stressed that this comparison only intends to illustrate that DIPS performance with ITk reaches the same order of magnitude as Run 2 and remains purely indicative : Run 2 DIPS benefited from much more optimization and larger samples to be trained with and it's logical that it remains better at this stage.

The extended η coverage from the ITk detector allows to tag jets in the forward region. However, the impact parameter resolution worsens for large $|\eta|$ values, as illustrated for instance in Figure 2.14, which in turn decreases the DIPS performance. This performance degradation in the forward region is observed for all flavour tagging algorithms.

3.4 Global flavour tagging performance with ITk

As explained in Section 3.2, the final tagging prediction doesn't belong to DIPS which is rather meant as an input for high level tagger DL1d. In this section, global flavour tagging performance of DIPS is shown along with the final predictive taggers DL1d and GN1 which also benefited for dedicated studies and optimization in the context of ITk and upgrade [3]. The pdf resampling and Loose tracks selection version of DIPS, which performance is shown in 3.3.3, is used for the training of DL1d on ITk.

Figure 3.18 shows the compared performance of DIPS, DL1d and GN1 on the upgrade $t\bar{t}$ and Z' samples. MV2 performance is also shown for the $t\bar{t}$ sample as it was the previous high-level tagger reference for upgrade configuration. DIPS is a low-level algorithm and that explains its lower performance in comparison to the other taggers. DL1d is outperforming MV2, especially for the c-jet rejection, which is consistent with Run 2 studies. However, beyond DL1d, the largest performance improvement is reached with GN1 as it was already the case with Run 2 configuration. In particular, a light and

c-jet rejection two times higher than MV2 and DL1d is achieved at the 70% b-jet tagging efficiency working point with the $t\bar{t}$ sample. As explained in 3.2.3, the auxiliary tasks of the algorithms (track classification and vertex finding) are responsible of this tremendous results.

The increase of performance at high p_T, already observed with the overall results on Z' sample which regroup jets with $p_T > 250$ GeV, is shown in Figure 3.19. A nearly 90% b-jet efficiency is achieved with GN1 for a jet p_T of 250 GeV, which is around 10% better than MV2. b-jet efficiency then decreases when the p_T gets larger as it was already the case for Run 2 taggers (Figure 3.9). The smaller size of pixel sensors in ITk with respect to current ATLAS Inner Detector are expected to provide better tracking performance and it is especially visible for large p_T jets which have a really dense environment.

To conclude on the expected ATLAS flavour tagging performance with ITk, these studies show the nice level of light and c-jet rejection in various range of conditions including high p_T and large pile-up values. They confirm that a strong level of performance is already achieved when adapting current state-of-the art taggers to the upgraded detector. The particular conditions of the HL-LHC did not change the insights from Run 2, with for instance the fact that the Loose tracks selection is providing better performance. Despite presenting lower performance than GN1, DIPS and its high level continuity DL1d results presented here are not reaching their full potential as further optimisation can still be made and allow for a performance improvement. Additional variables provided by ITk about the hits in the different layers and region of the detector could for instance be added in the training.

The HL-LHC physics program will only start taking data in 2029 and there is no guarantee that the taggers presented here will be used at this time. The recent progress with graph neural networks shows that unexpected breakthroughs can happen when new methods are prospected.

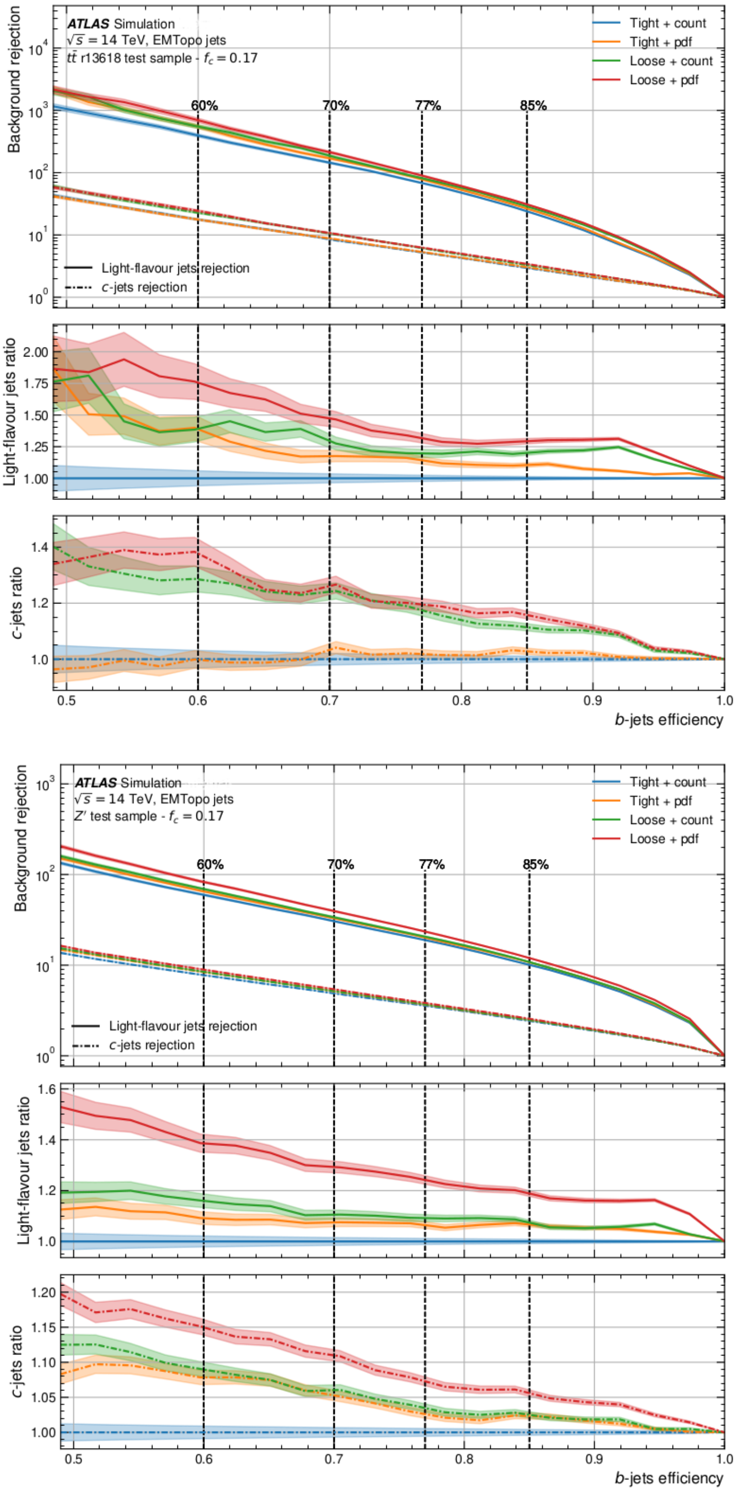

Figure 3.14: The light-flavour jet and c-jet rejection factors as a function of ε_b for the upgrade DIPS trainings with either Tight or Loose tracks selection and pdf or undersampling resampling methods. The trainings are evaluated on $t\bar{t}$ (top) and Z' (bottom) evaluation sets.

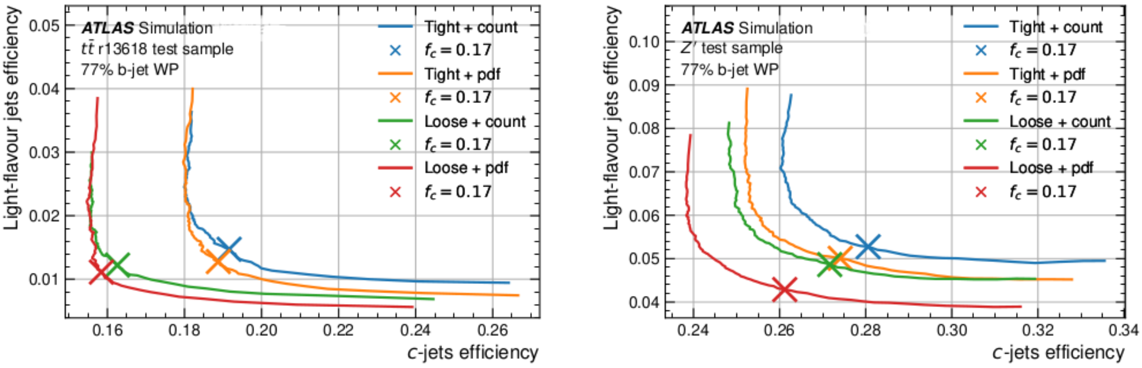

Figure 3.15: Fraction scan plots are parametric curves showing the light and c-jet efficiency for different values of f_c at a fixed b-tagging effiency of 77%. Four trainings with different combinations of resampling methods and tracks selection are compared.

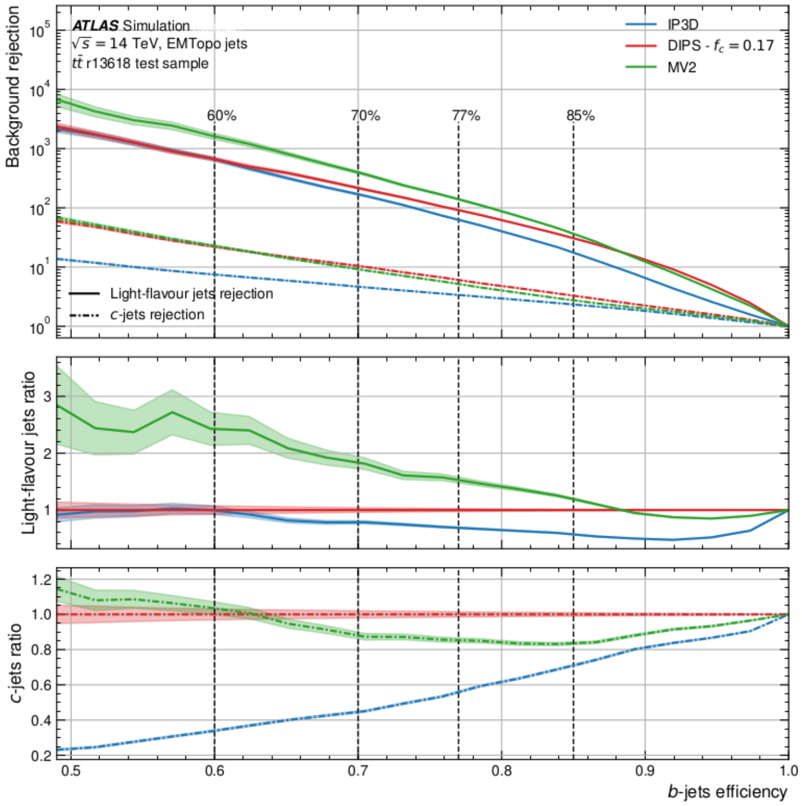

Figure 3.16: The light-flavour jet and c-jet rejection factors as a function of ε_b for the IP3D, MV2 and DIPS taggers on ITk $t\bar{t}$ samples.

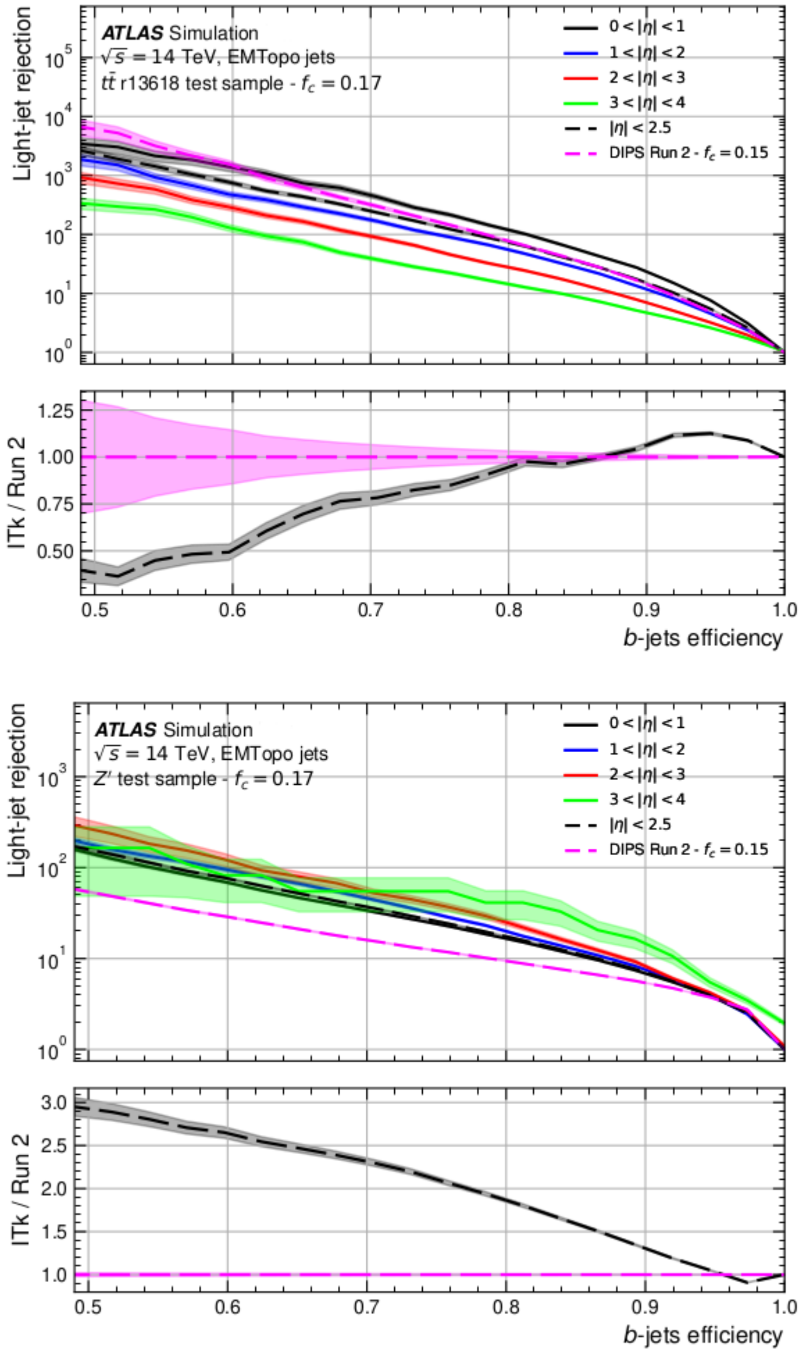

Figure 3.17: Light-jet rejection as a function of ε_b of the upgrade DIPS for different η ranges. The tagger is evaluated on $t\bar{t}$ (top) and Z' (bottom) events. The performance of the Run 2 DIPS (black dashed line) is also shown for comparison.

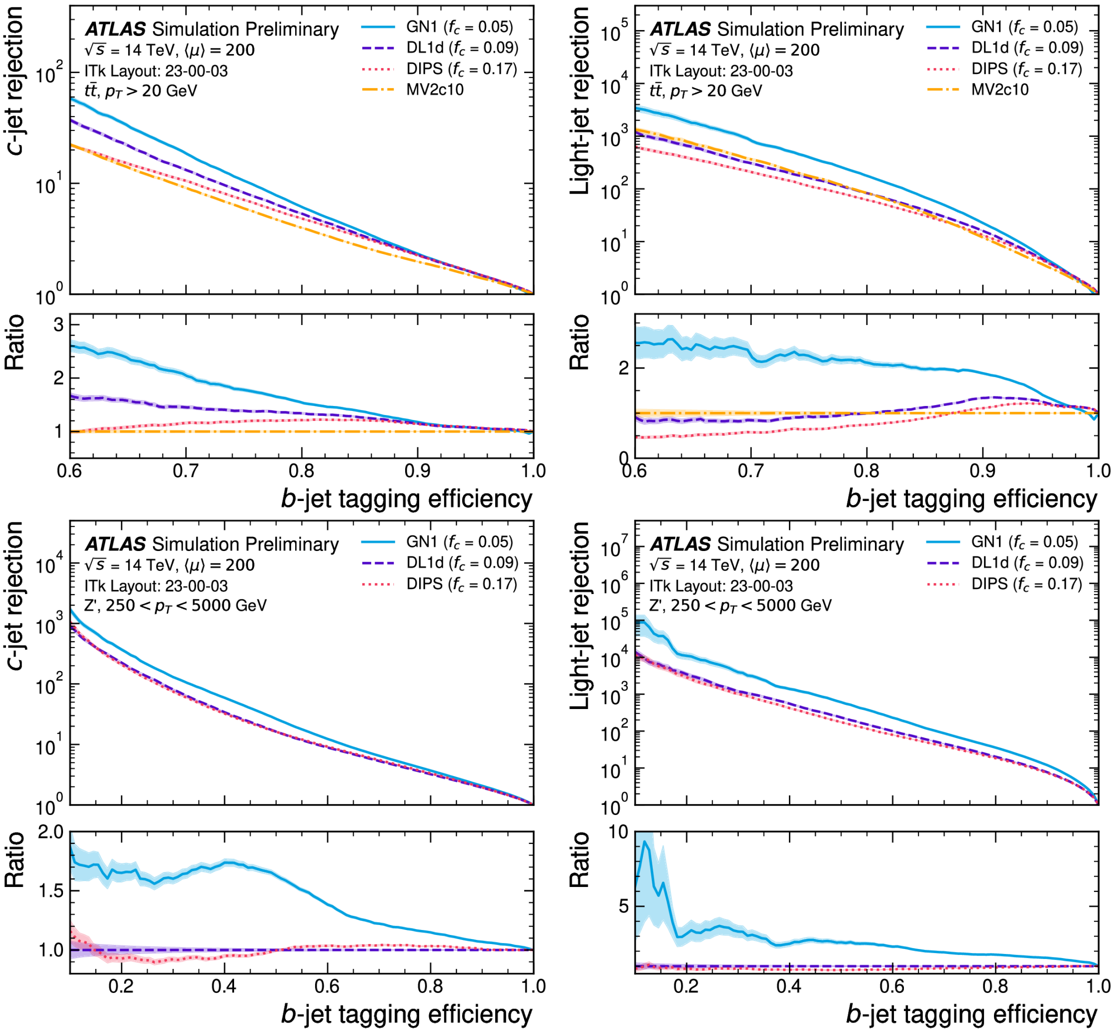

Figure 3.18: The c-jet (left) and light flavour jet (right) rejections as a function of ε_b for the different taggers on the upgrade configuration. The trainings are evaluated on the $t\bar{t}$ (top) and Z' (bottom) samples [3].

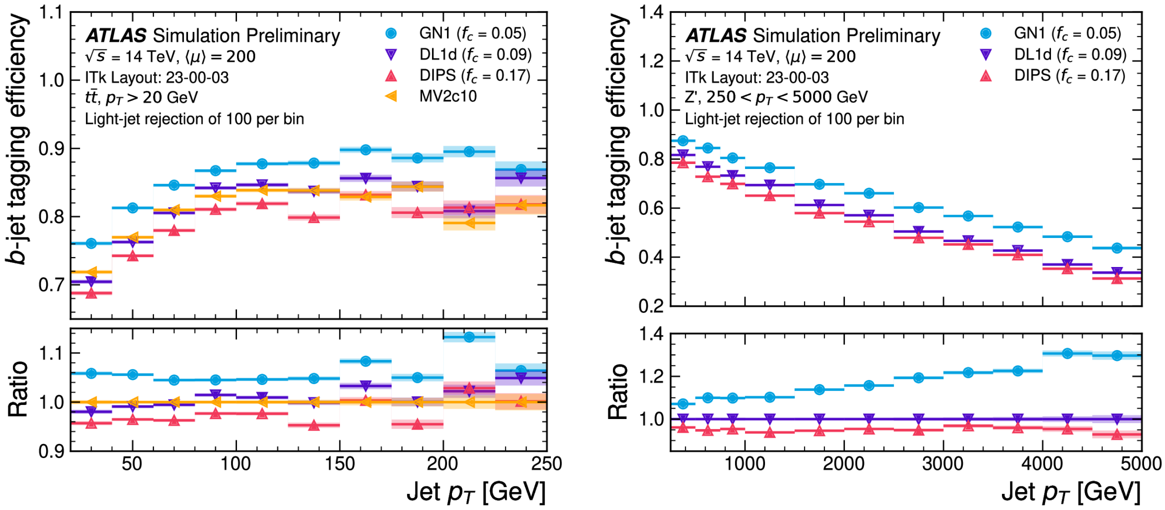

Figure 3.19: b-jet tagging efficiency ε_b for jets in the $t\bar{t}$ (left) and Z' (right) sample as a function of jet p_T with a fixed light-flavour jet rejection of 100 in each bin.

4 Search for two additional scalar particles in the $X \to S(\to b\bar{b})H(\to \gamma\gamma)$ channel

Table of contents

Introduction

As we have seen in Chapter 1, the existence of additional scalar bosons is predicted by some theoretical models designed to overcome the Standard Model shortcomings. This chapter presents the analysis performed by the ATLAS experiment to look for two new bosons in the $X \to SH \to b\bar{b}\gamma\gamma$ channel and recently published in this paper [9].

Analysis overview The search for the particles X and S is performed in the $b\bar{b}\gamma\gamma$ channel and uses the same dataset as the non-resonant di-Higgs analysis with the same final state $HH \to b\bar{b}\gamma\gamma$ [74, 42].

Since the masses of X and S are unknown, a wide range of masses m_X and m_S are considered in the analysis, with the constrain that $m_X > m_S + m_H$ so that the $X \to SH$ decay is kinematically allowed.
The di-photon triggers with low p_T threshold allow to probe lower mass compared to analyses with different final states : from 170 to 1000 GeV for X and from 15 to 500 GeV for S. The range of the probed m_X and m_S masses compared to other works is illustrated in Figure 4.1. This paper is in particular the first to probe low masses for m_X and m_S, below 200 GeV and 50 GeV respectively. The range of the search region is limited at high mass by the low background statistics which does not allow to perform a fit. At low mass, the merging of the jets from the S boson decay imposes a lower limit at around 15 GeV for m_S from which comes the minimum value for m_X because of the kinematic constrain.

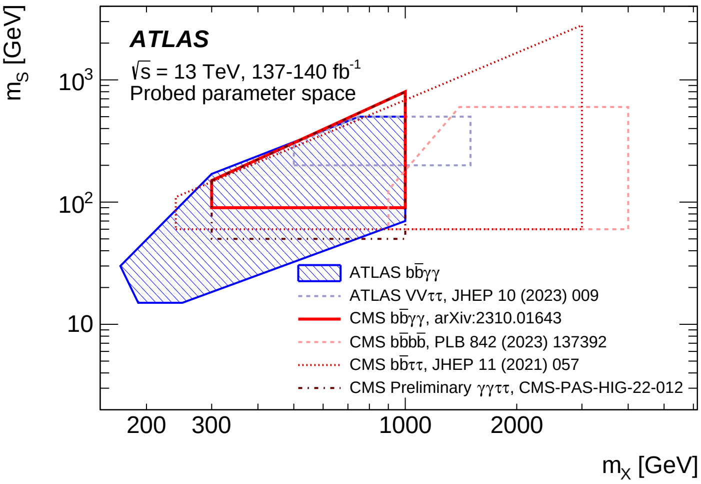

Figure 4.1: Parameter space probed by the present $X \to SH$ analysis (hatched blue area) compared to other CMS and ATLAS analysis in the $b\bar{b}\gamma\gamma$ [6], $b\bar{b}b\bar{b}$ [7], $b\bar{b}\tau^+\tau^-$ [8] and $VV\tau^+\tau^-$ [78] final states [9].

In the $b\bar{b}\gamma\gamma$ final state, the backgrounds can be divided in two categories. Resonant background consists of all processes that have their two photons invariant mass distribution $m_{\gamma\gamma}$ peak at the Higgs mass $m_H \approx 125$ GeV. This is the case for example for single-Higgs and di-Higgs processes like ZH or ttH and HH respectively. Non resonant background on the other hand consists of various processes with two photons and jets in the final state. This category, labelled as "$\gamma\gamma +$ jets ", includes $\gamma +$ jets and multijet events where one or both of the photon candidate are misidentified as jets as well as heavy flavour produced along with two photons : $t\bar{t}\gamma\gamma$ and $Z(\to q\bar{q})\gamma\gamma$. The number of $\gamma\gamma +$ jets events is decreasing with $m_{\gamma\gamma}$.
To cope with these two background categories and to specifically target the $H \to \gamma\gamma$ decay, a *signal region* (SR) is defined with events around the Higgs mass peak whereas events outside of this signal region form control region *sidebands* (SB).

The analysis strategy to separate signal from background events in the signal region relies on parameterised neural networks (PNNs). It will be detailed in Section 4.2. The main objects used in the analysis will be presented beforehand in Section 4.1. Particular stress will be put on theoretical and experimental systematic uncertainties in Section 4.3 as it was the main subject of my work. The statistical analysis which consists in fitting the PNN distribution and the following results are finally presented in Section 4.4.

4.1 Analysis inputs

4.1.1 Data and Monte Carlo samples

Data The data used in this analysis was collected at the ATLAS detector during the LHC Run 2 between 2015 and 2018. The dataset consists of proton-proton collisions recorded at a $\sqrt{s} = 13$ TeV centre of mass energy and has an integrated luminosity of 140 fb^{-1} [141].

The analysis makes use of two different diphoton triggers. They both require two reconstructed photon candidates with minimum transverse energies of 35 GeV for the leading one (i.e the one with the largest E_T) and 25 GeV for the subleading one. For the 2015-2016 data taking period, the trigger requires the photons candidates to have at least the Loose photon identification criterion. These L1 level trigger specifically focus the $H \to \gamma\gamma$ decay by requiring two separate energy deposits of more than 15 GeV. In the remaining of the data taking period, the trigger used needs the Medium identification criterion because of the increasing pile-up.

MC samples Monte Carlo simulated samples are used to model both signal and Standard Model background events.

For signal, a total of 161 samples with different m_X and m_S values are produced to provide a satisfying coverage of the masses space. Questions relative to the granularity of the signal probed will be discussed in more details in Subsection 4.2.3. The samples are produced using the Pythia MC generator at the leading order in QCD. The narrow width approximation is used to model the X and S decays. Theoretical motivations for this assumption are discussed in Chapter 1. Finally, the signal sample production uses the AF2 ATLAS fast simulation.

The list of signal and background samples along with their MC generators and their main parameters is shown in Table 4.1. The resonant background samples include minor single-Higgs processes such as ggF and VBF Higgs production, WH, $b\bar{b}H$, tHq or tWH along with the main ones discussed in the introduction.

4.1.2 Object definition

This section regroups the definition of the physical objects used in the analysis.

Photons are reconstructed from topological clusters in the EM calorimeter as described

Process	**Generator**	**PDF set**	**Showering**	**Tune**
$X \to SH$	Pythia 8.2	NNPDF2.3$_{LO}$	Pythia 8.2	A14
Non resonant backgrounds				
$\gamma\gamma$ + jets	SHERPA 2.2.4	NNPDF3.0$_{NNLO}$	–	–
$t\bar{t}\gamma\gamma$	MadGraph MC@NLO	NNPDF2.3$_{LO}$	Pythia 8.2	A14
$Z(\to q\bar{q})\gamma\gamma$	SHERPA 2.2.11	NNPDF3.0$_{NNLO}$	–	–
Single Higgs backgrounds				
ggF H	NNLOPS	PDF4LHC15	Pythia 8.2	AZNLO
VBF H	PowhegBox v2	PDF4LHC15	Pythia 8.2	AZNLO
WH	PowhegBox v2	PDF4LHC15	Pythia 8.2	AZNLO
$qq \to ZH$	PowhegBox v2	PDF4LHC15	Pythia 8.2	AZNLO
$gg \to ZH$	PowhegBox v2	PDF4LHC15	Pythia 8.2	AZNLO
$t\bar{t}H$	PowhegBox v2	NNPDF3.0$_{NLO}$	Pythia 8.2	A14
$b\bar{b}H$	PowhegBox v2	NNPDF3.0$_{NLO}$	Pythia 8.2	A14
tHq	MadGraph MC@NLO	NNPDF3.0$_{NLO}$	Pythia 8.2	A14
tHW	MadGraph MC@NLO	NNPDF3.0$_{NLO}$	Pythia 8.2	A14
Di-Higgs backgrounds				
ggF HH	PowhegBox v2+FT	PDFLHC	Pythia 8.2	A14
VBF HH	MadGraph MC@NLO	NNPDF3.0$_{NLO}$	Pythia 8.2	A14

Table 4.1: Summary of the main signal and background samples including the generator used in the simulation, the PDF set, the showering model, and the set of tuned parameters.

in Subsection 2.3.2. The Tight identification criteria is used and objects in the region at the junction between the barrel and the endcap region (with $1.37 < |\eta| < 1.52$) are excluded. Photon must verify the Loose isolation criteria which requires them to have $E_T^{iso}/E_T < 0.065$ and p_T^{iso} / E_T < 0.05 where the transverse energy and impulsion are computed in a cone of size $\Delta R = 0.2$ around the object.

Electrons and muons are not present in the analysis final state but are indirectly a part of the event selection since events including them are excluded (see Subsection 4.1.3). Electrons are reconstructed with EM calorimeter and tracks information in the $|\eta| < 2.37$ region excluding the barrel-endcap junction. Muons use matching information between the MS and the ID and have a higher acceptance zone up to $|\eta| < 2.7$. Both leptons must have a transverse momentum $p_T > 10$ GeV and the Medium identification criteria is used in both cases. Finally, requirements on their transverse impact parameters d_0 and z_0 must also be fulfilled so that the particles are correctly matched to the primary vertex.

The reconstruction procedure for jets objects is described in Subsection 2.3.3. PFlow jets that combine both tracks in the ID and calorimeters cells topoclusters information are used and they are reconstructed using the anti-k_T algorithm with a radius parameter of $\Delta R = 0.4$. Jets must also have a rapidity $|y| < 4.4$ and a transverse momentum $p_T > 25$ GeV. Like for leptons, a requirement on the compatibility of the jet with the primary vertex is applied : jets within $|\eta| < 2.4$ and with $p_T < 60$ GeV must satisfy the Tight JVT criteria.

The flavour of the jets is assessed using the DL1r flavour tagging algorithm described in Subsection 3.2.2. The 77% efficiency working point is used which gives a misidentification rate of 1/130 for light-flavour jets and 1/4.9 for charm jets.
Finally, an overlap removal procedure is applied to avoid same signatures in the detector leading to different reconstructed objects. Here, priority is given to photons followed by jets and then leptons.

4.1.3 Event selection

The dataset used in the analysis is the same as the one of the $HH \to b\bar{b}\gamma\gamma$ analysis [74]. The requirements consist in a regular preselection of events in the $b\bar{b}\gamma\gamma$ final state with a few additional criteria to target photons coming from a Higgs boson decay. On top of the trigger criteria described in Subsection 4.1.1, events are selected if they have :

- At least two isolated photons satisfying the ATLAS tight identification criteria. They must verify two additional properties : their invariant mass $m_{\gamma\gamma}$ must be between 105 and 160 GeV and the leading (subleading) photon must have a transverse impulsion $p_T > 0.35$ (0.25) $m_{\gamma\gamma}$.
- No identified electrons or muons. This criteria is known as the lepton veto and intends to reduce the ttH background as more than half of the top quark pair decays contain leptons.
- A number of central jets (i.e with a pseudorapidity $|\eta| < 2.5$) between 2 and 5 included.
- Exactly one or two b-tagged jet at the 77% working point. The exact number of selected b-tagged jet is the subject of the next section.

Event passing the initial preselection are divided into the signal region around the Higgs mass peak and the control region sidebands that are used to constrain the $\gamma\gamma +$ jets events normalisation. The SR is composed of events with an invariant photon mass $m_{\gamma\gamma}$ between 120 and 130 GeV. This criteria is the same for both 1 and 2 b-tagged regions.
The Monte Carlo samples are used to find the expected number of events of the different signal and background processes in the SR and CR in the dataset after preselection. Tables 4.2 and 4.3 show the yields for the resolved and merged region respectively.

These tables show that the main resonant backgrounds are ttH, ZH and HH for the 2 b-tagged selection and ttH, ZH, HH and ggH for the 1 b-jet one. Despite this, the non resonant $\gamma\gamma +$ jets background remain the dominant process even in the signal region because of its huge global production rate.
The data in the signal regions are still blinded at this point to avoid bias in the analysis procedure. However, this is not the case in the sidebands and the comparison between Monte Carlo and data in this region make appear a large discrepancy. This is because some events inside the non-resonant diphoton background are not properly modelled

	Sideband	Signal region
ttH	0.206 ± 0.002	8.107 ± 0.014
ZH	0.073 ± 0.002	3.617 ± 0.013
ggH	0.109 ± 0.009	5.345 ± 0.065
HH ggF+VBF	0.027 ± 0.001	1.664 ± 0.004
$tHjb$	0.022 ± 0.004	0.947 ± 0.029
$VBFH$	0.014 ± 0.002	0.671 ± 0.012
bbH	0.017 ± 0.004	0.603 ± 0.023
WH	0.005 ± 0.001	0.203 ± 0.004
tWH	0.003 ± 0.001	0.128 ± 0.005
$\gamma\gamma$+jets	1134.23 ± 4.11	284.088 ± 2.056
$Z(\to qq)\gamma\gamma$	16.362 ± 0.271	3.983 ± 0.136
$t\bar{t}\gamma\gamma$	22.939 ± 0.097	5.751 ± 0.049
Total SM	1174.006 ± 4.12	315.108 ± 2.063
Data	1479	-
$m_{X,S} = (250, 110)$	0.468 ± 0.026	9.474 ± 0.118

Table 4.2: Expected number of events for a luminosity of 140 fb^{-1} with the 2 b-tagged selection in the sidebands and in the SR. Signal cross-sections of 1 fb are used. The uncertainties correspond to the statistical variations.

by Monte Carlo samples such as the multijet events with jets mistagged as photons. To cope with this, data events will be used to correct the normalisation by introducing a normalizing factor.

4.2 Analysis strategy

This section details the methods designed to distinguish signal from background events using multivariate analysis techniques in Subsection 4.2.2. Other important points specific to the $X \to SH$ signal like the merged and resolved regions definition and the signal interpolation are discussed in Subsection 4.2.1 and 4.2.3 respectively.

4.2.1 Resolved and merged regions

A challenging situation arises for signals with $m_S \ll m_X$. In that case, the S boson is boosted and the b-jets originating from its decay will be collimated along its momentum direction really close to each other.

Figure 4.2 show the distribution of the angular distance between the two b-jets for two different signal samples at truth level. For the point with the largest m_X / m_S ratio, the

	Sideband	Signal region
ttH	0.31 ± 0.003	11.377 ± 0.017
ZH	0.169 ± 0.003	7.356 ± 0.018
ggH	1.206 ± 0.032	47.351 ± 0.199
HH ggF+VBF	0.031 ± 0.001	1.796 ± 0.004
$tHjb$	0.054 ± 0.008	2.629 ± 0.05
$VBFH$	0.182 ± 0.006	8.155 ± 0.041
bbH	0.101 ± 0.008	2.875 ± 0.046
WH	0.145 ± 0.003	5.827 ± 0.021
tWH	0.013 ± 0.001	0.559 ± 0.009
$\gamma\gamma$+jets	13030.1 ± 14.334	3279.61 ± 7.189
$Z(\to qq)\gamma\gamma$	42.694 ± 0.716	11.035 ± 0.357
$t\bar{t}\gamma\gamma$	39.778 ± 0.127	10.04 ± 0.064
Total SM	13114.781 ± 14.352	3388.612 ± 7.202
Data	13450	-
$m_{X,S} = (190, 15)$	0.48 ± 0.012	10.235 ± 0.055

Table 4.3: Expected number of events for a luminosity of 140 fb^{-1} with the 1 b-tagged selection in the sidebands and in the SR. Signal cross-sections of 1 fb are used. The uncertainties correspond to the statistical variations.

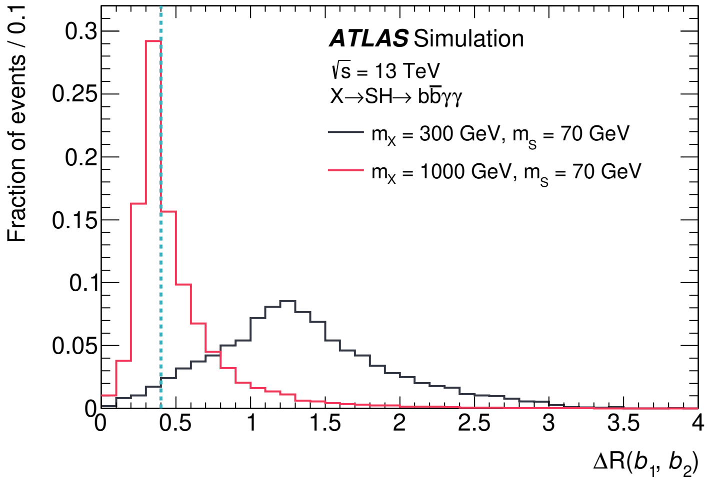

Figure 4.2: Angular distance ΔR between the two jets from the S boson decay at generator level for two signal points. The vertical dashed blue line at 0.4 corresponds to the radius parameter for the reconstructed jet [9].

peak of the distribution gets below the standard angular opening of jets in ATLAS. In that case, the two jets can be reconstructed as only one jet as illustrated in Figure 4.3.

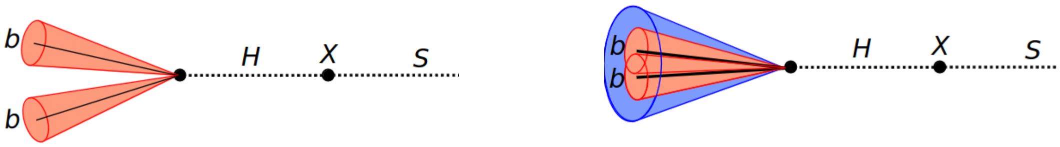

Figure 4.3: Sketch illustrating the collimated b-jets resulting in their reconstruction in a single jet when $m_S \ll m_X$ (right) as opposed to the separated b-jets (left).

.

The strategy chosen to tackle this issue is to define two search regions with either exactly one or two b-tagged jets to specifically target each type of signal. They are called *merged* and *resolved region* respectively. Events with more than two b-tagged jets are not considered to ensure orthogonality with other channels looking for same signal with a large number of b-jets in the final state like $b\bar{b}b\bar{b}$.
To define in which region will belong each probed signal, the ratio between the number of signal events selected with the 2 b-jets selection over the number of events selected with both ones is used. As illustrated in Figure 4.4, this ratio gets below 50% when the ratio of the masses m_S / m_X is $\lesssim$ 0.09. For points close to this limit, the two methods are compared to select the one leading to the best expected limit.

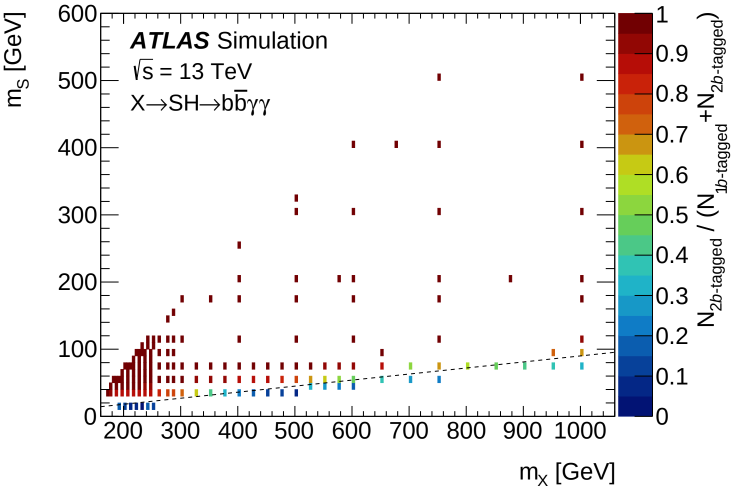

Figure 4.4: Fraction of signal events in the 2 b-tagged selection as a function of the m_X and m_S masses. The dashed line corresponds to the partition between the two selections, corresponding empirically to m_S / m_X = 0.09 [9].

4.2.2 Parameterised neural networks

To separate signal from background events inside the signal region, a multivariate analysis is used in the form of parameterised neural networks (PNNs) [142]. PNNs are deep sets neural networks that take as input a vector of parameters written $\bar{\theta}$ in addition to the traditional vector of event features (written $\bar{x}$). The output of the PNN will then be a function of the parameters $\bar{\theta}$. For a each of these parameter, a statistical fit is performed on the PNN distribution to detect any excess of events which could indicate the presence of signal.
One of the interest of PNNs is that it allows us to train only one network and have an output on all mass points instead of having to train a dedicated network for each of the points, therefore allowing us to search in a large mass space. An equally interesting feature is that a smooth interpolation of the PNN for parameters that haven't been included in the training is possible, as this will be developed in the next section.

In this analysis, two distinct PNNs are trained, one for the resolved region and one for the merged region. In the 2 b-tagged jets region, the parameters of the PNN are the masses of the particle we look for $\bar{\theta} = (m_S, m_X)$ whereas in the 1 b-tagged jet one it's only the X mass $\bar{\theta} = (m_X)$. This is because the invariant mass of the single b-tagged jet is not properly calibrated, meaning that no information on m_S can be obtained from it.
The decay products of the S and X particles are supposed to have an invariant mass equal to the mass of the initial particle. That is why the $m_{b\bar{b}}$ and $m_{b\bar{b}\gamma\gamma}$ variables corresponding to m_S and m_X respectively are used as the input features of the PNNs. More precisely, in the resolved region the event input features of the PNN are $\bar{x} = (m_{b\bar{b}}, m^*_{b\bar{b}\gamma\gamma})$ where $m^*_{b\bar{b}\gamma\gamma} = m_{b\bar{b}\gamma\gamma} - (m_{\gamma\gamma} - 125\text{ GeV})$. The modified invariant mass $m^*_{b\bar{b}\gamma\gamma}$ is used instead of $m_{b\bar{b}\gamma\gamma}$ order to remove correlations between the PNN score and $m_{\gamma\gamma}$. In the 1 b-jet region, the inputs are $\bar{x} = (p_T^b, m^*_{b\gamma\gamma})$ where similarly $m^*_{b\gamma\gamma} = m_{b\gamma\gamma} - (m_{\gamma\gamma} - 125\text{ GeV})$. As discussed before, the transverse momentum of the single jet is used instead of its invariant mass for which calibration is not assured. The network appears to achieve the best performance with only these variables as event features. Including additional features has been tested but was proved to confuse the network rather than helping it.

The training samples consist in events from signal mass points and main sources of background. The simulated MC samples described in Subsection 4.1.1 are used. For background, the resolved region PNN training makes use of the $\gamma\gamma$ + jets, $t\bar{t}H$, ZH and ggF H samples. In the merged region, the VBF single H and di-Higgs samples (HH) are also included since they are more important with this selection. For signal, 69 points are used for the training among the mass grid. Boosted signal samples with $15 \leq m_X \leq 70$ GeV are used in the merged region while the rest of them are used in the resolved region PNN training. Both PNNs are trained using the Keras [143] library with TensorFlow [144] backend. For each event, the parameter $\bar{\theta}$ is set to the corresponding m_X and m_S masses for signal and to random values for background events since it is not relevant for them.

As seen in Table 4.2 and 4.3, the number of events in the signal region are quite unbalanced with a majority of $\gamma\gamma$ + jets events. This class unbalance could interfere with the training and make the PNN classify everything as background. To limit this, a unit weight is applied to all MC events and a bias on the number of signal and background events is applied to the last layer of the PNN.
The loss function used in the training is the binary cross entropy and the optimisation method is stochastic and gradient based with the Adam algorithm. The architecture of the network has been optimized with KerasTuner to select the parameters that maximised the Area-Under-Curve (AUC) of the evaluation set. As a result, the 2 b-tagged region network has four hidden layers with respectively 85, 49, 45 and 81 nodes whereas the 1 b-tagged region PNN has three hidden layers with 101, 29 and 101 nodes. A dropout rate between 2% and 20% is applied in these layers and the output layers of both PNNs have a single node. Finally, the activation function used is the rectified linear unit function in the hidden layers and the sigmoid function in the output layers.

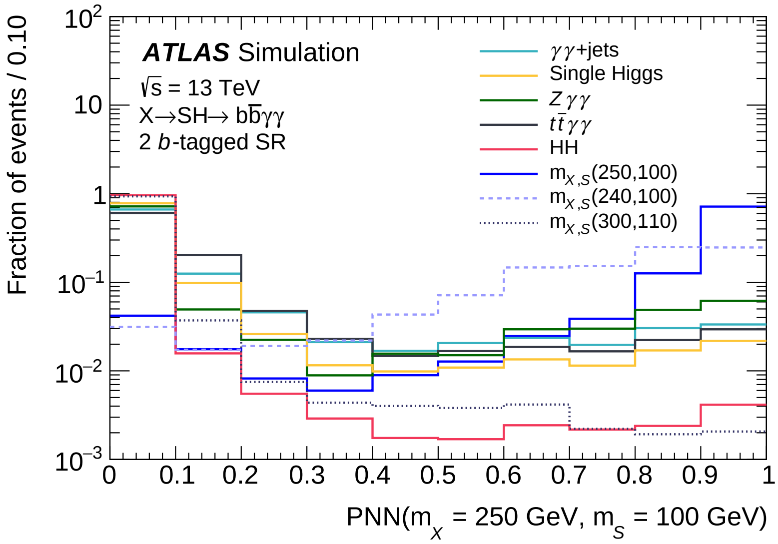

Figure 4.5: (m_X, m_S) = (250, 100) GeV PNN score distributions in the 2 b-tagged signal region for simulated background events and a subset of signal events with various (m_X, m_S) values. All distributions are normalised to unity and display a constant bin size.

Example of PNN distributions of background and signal events can be seen in Figure 4.5. As expected, background distributions are peaking near 0 while the targeted signal peaks towards 1. The PNN is also able to distinguish the signal it targets from other $X \to SH$ signals with different values for m_X and m_S. The closer a signal is to the PNN parameters, the better the network will rate it as demonstrated with the (m_X, m_S) = (240, 100) GeV distribution which gets much closer to 1 than the one for (m_X, m_S) = (300, 110) GeV, a point farther away from the PNN parameters (250, 100) GeV.
The validity of the PNN is checked afterwards by comparing its output shape with data

and MC in the sideband regions. This part will be covered in Subsection 4.4.1.

Other methods have been considered for the analysis such as a 2D fit on the $m_{b\bar{b}\gamma\gamma}$ and $m_{b\bar{b}}$ distributions or the traditional method used in the $HH \to b\bar{b}\gamma\gamma$ analysis [74] which consists in fitting the $m_{\gamma\gamma}$ distribution.

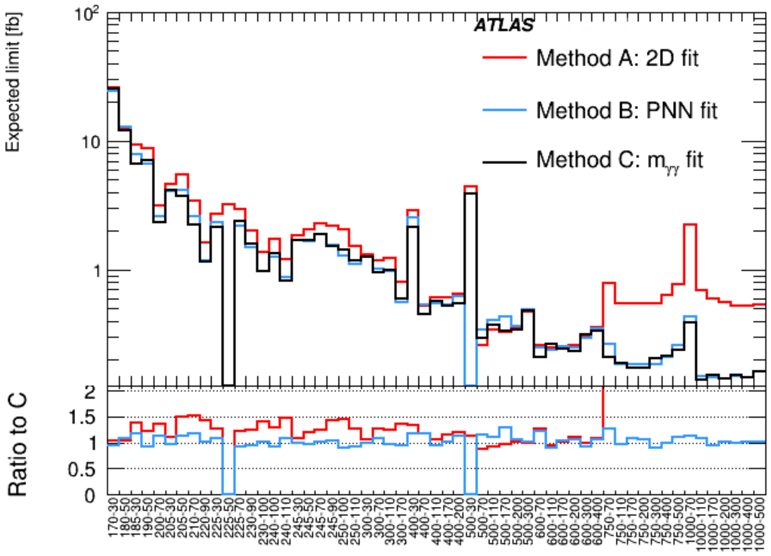

Figure 4.6: Expected upper limits of the $X \to SH \to b\bar{b}\gamma\gamma$ signal as a function of the different (m_X, m_S) mass points with the three tested methods. The bottom panel is the ratio plot to the $m_{\gamma\gamma}$ fit method.

The upper limits obtained with the three methods are compared in Figure 4.6. The 2D fit method provides higher upper limits by around 50% and is outperformed at high mass because of the lower statistics. The results are relatively similar between the $m_{\gamma\gamma}$ fit and the PNN fit methods. The latter one is eventually chosen because of its versatility as it allows to precisely target a given (m_X, m_S) signal. Another reason is that thanks to the very principle of the PNN, it is easy to probe interpolated signals between simulated signals samples. This is the subject of the next section.

4.2.3 Signal interpolation

The goal of the analysis is to set continuous limits on the $X \to SH$ production in the (m_X, m_S) plane. To do so, the PNN shape of signal and background events can be interpolated in between the simulated points to allow for a thinner grid coverage.

The distance between two successive mass point, generally known as the granularity, must be defined by doing *injection tests*. To check that no X and S signal is missed, arbitrary (m_X, m_S) signals are injected into the PNN and the sensibility of neighbouring points PNNs is checked. It is indeed one of the interest of the PNN strategy that a PNN of parameter $\bar{\theta} = (m_X, m_S)$ is sensible to neighbouring masses parameters. The chosen criteria is that an injected signal with a cross section equals to twice the expected limit must lead to a 3 σ sensibility in the neighbouring points to consider the granularity thin enough.

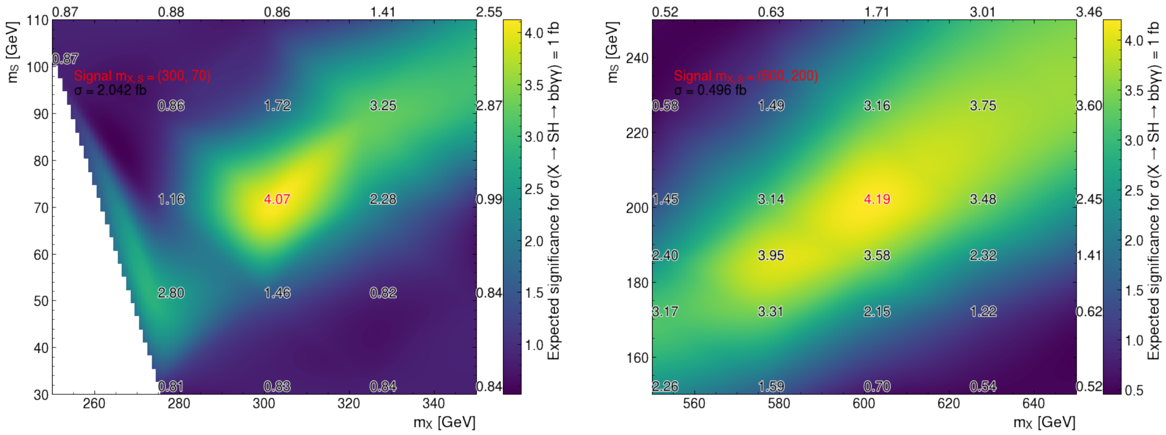

Figure 4.7: Expected significance from an injected signal with (m_X, m_S) = (300, 70) GeV (left) and (m_X, m_S) = (600, 200) GeV (right). The left (right) plot shows the significance obtained from fitting the PNN(m_X, m_S) distribution of the point with the same m_X and m_S values as the injected signal (in red) and from nearby points within 25 (50) GeV of the true signal.

Examples of injection tests are shown in Figure 4.7. Both plots show that the granularity criteria is verified with a distance between points of either 25 GeV at low mass or 50 GeV at high mass. The granularity is linked to the signal $m_{b\bar{b}}$ and $m^*_{b\bar{b}\gamma\gamma}$ distributions resolution which increases with m_X and m_S, hence explaining the larger gap needed between the points at high mass.

The interpolation of non simulated signal samples is made in two steps. The first part is the interpolation the PNN distribution shape. To do so, the only things needed are the event features which are the $m_{b\bar{b}}$ and $m^*_{b\bar{b}\gamma\gamma}$ distributions. A reference simulated signal samples is used to compute four-vectors of the particles X, H and S. The four vectors of the targeted interpolated point can then be obtained using Lorentz transformation. The resolution effects that impact kinematic distributions $m_{b\bar{b}}$ and $m^*_{b\bar{b}\gamma\gamma}$ are calculated by interpolating the ones from nearby simulated signal samples. The fit of the distribution is considered to be a Bukin probability distribution [145] which has 5 free parameters. These parameters are depending on m_X and m_S and can be interpolated with Delaunay triangulation [146] to provide the ones of the targeted interpolated point (m_X^{int}, m_S^{int}). The second step consists in estimating the signal selection efficiency at (m_X^{int}, m_S^{int}). The interpolated yields are computed by using once again Delaunay triangulation between yields of simulated signal samples in the (m_X, m_S) plane.

This method does not works perfectly well in the entire probed zone. The goodness of the interpolation can be evaluated by comparing the expected limits obtained with simulated signals and with the interpolation method.

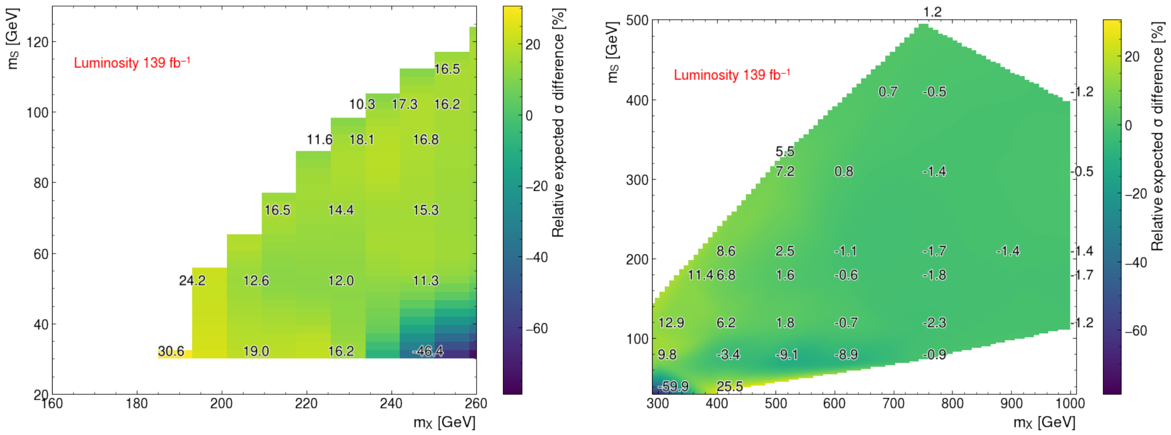

Figure 4.8: Difference between expected limits obtained when using MC or interpolated PNN score distributions in the (left) low mass and (right) high mass regions. Only statistical uncertainties are considered.

Figure 4.8 shows that the differences are rather small (less than 10%) in the high mass region i.e with $300 \leq m_X \leq 1000$ GeV whereas they are much more important at low mass i.e for $170 \leq m_X \leq 300$ GeV. This is because of the lower jet resolution at low mass which contaminates the $m_{b\bar{b}}$ distribution and makes the interpolation more difficult. At large m_X and low m_S, the interpolation also fails with difference in expected limits reaching 10%. For these reasons, the interpolation is only used in the region defined by $m_X \geq 300$ GeV and $m_S \geq 70$ GeV. In other parts of the mass space, more signal MC samples are produced to meet with the granularity needs discussed in the beginning.
The different status of the probed mass points (merged or resolved region, simulated or interpolated) is summed up in Figure 4.9.

4.3 Systematic uncertainties

Like any other measurements in experimental physics, this analysis must take into account the systematic uncertainties. They can be regrouped in two broad categories : experimental uncertainties which are about the effect of the detector on the measurements of physical quantities, and theoretical uncertainties which come from the undetermination of the analysis theory input such as a production cross-section.
The idea is to study the effect of these uncertainties all the way from the analysis inputs to the results. In our case, their impact will either take the form of an uncertainty on the normalisation of the PNN distribution (also known as *scale* uncertainty) or on the shape of this distribution. In the end, the systematic uncertainties will be taken as nuisance

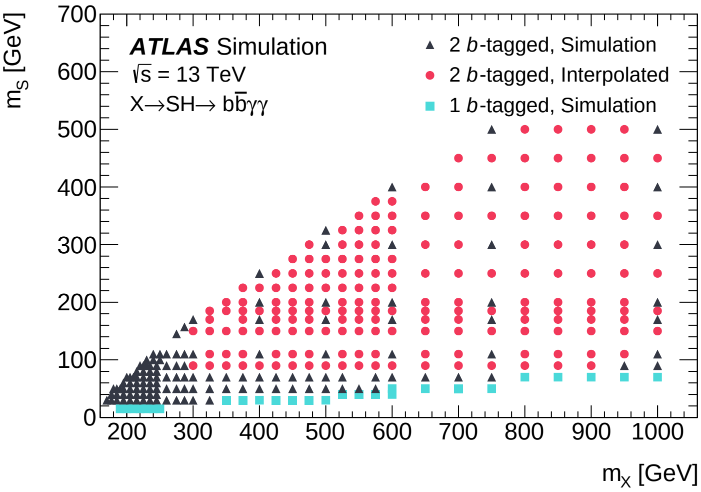

Figure 4.9: (m_X, m_S) signals probed by the analysis [9].

parameters (NP) in the fit as developed in Section 4.4.

The theoretical uncertainties will be discussed first in Subsection 4.3.1 while the experimental ones will be detailed in 4.3.3. A particular stress will be put on the $\gamma\gamma$ modelling uncertainty in Subsection 4.3.2.

4.3.1 Single Higgs theoretical systematic uncertainties

Theoretical uncertainties embrace different types of uncertainties which depend on the background or signal process considered.

They can be regrouped in three categories :

- QCD scale uncertainties which describe the theoretical uncertainties on the QCD factorisation and renormalisation scale to take into account for the higher order corrections during the event generation.
- The uncertainties on the Parton Distribution Function (PDF) and the strong interaction strength α_s and how they are taken into account by the MC generators.
- The parton shower uncertainties, which estimate the uncertainty on the shower modelisation by the MC generator. They are obtained by comparing the nominal samples to alternative ones using a different shower generator.

Most of these uncertainties only affect the event normalisation, with a few exceptions. For the single Higgs WH, ggF H and VBF H production modes, a global 100% scale uncertainty is taken. This is because in these processes, b-jets production does not happen at leading order but rather with initial and final state radiations which are difficult to model. The conservative 100% uncertainty is motivated by studies on heavy-flavour production with top quark pairs [147, 148] and W boson [149].

The major single Higgs background ttH and ZH which have b-quarks produced at leading order have the shape effect of these uncertainties taken into account. QCD scales uncertainties are estimated by varying the factorisation and renormalisation scales values up and down and taking the envelope of the variation. PDF and α_s uncertainties are computed by using the PDF4LHC recommendations and the Parton shower ones are obtained by comparing the nominal Pythia 8.2 sample to the Herwig alternative shower generator. The effect on the PNN distribution can lead to a 5% difference with the nominal distribution in some bins for PDF and 10% for the parton shower uncertainties. The QCD and PDF uncertainties are also evaluated with both yields and shape changes for $Z(q\bar{q})\gamma\gamma$ samples.

For smaller resonant backgrounds, two global inclusive normalisation uncertainties encompassing the QCD scale and the PDF $+\alpha_S$ uncertainties are taken. Their values are regrouped in Table 4.4.

	QCD Scale	PDF+α_S
ggH	100 %	
VBF	100 %	
WH	100 %	
gg→ZH	$^{+25.1\%}_{-18.9\%}$	2.4 %
bbH	$^{+20.2\%}_{-23.9\%}$	
tHbj	$^{+\%2.4\%}_{-1.8\%}$	2.2 %
tHW	$^{+\%4.9\%}_{-6.7\%}$	6.3 %
ggHH	(+m_{top} unc.) $^{+6\%}_{-23\%}$	3 %
VBFHH	$^{0.03+\%}_{-0.04\%}$	2.1%

Table 4.4: Inclusive theoretical uncertainty (in %) on the cross-sections for the minor single-Higgs and di-Higgs backgrounds.

Signal PDF uncertainties are evaluated with the same method as the ttH and ZH samples. The corresponding variation in the PNN bins is between 2% and 10% which gives a total 11% scale uncertainty. As signal samples generation was done with Pythia which simulates the whole event, the parton shower modelling cannot be compared to an alternative sample and is evaluated with an inclusive 10% normalisation uncertainty based on a similar study with HH samples [74].

Lastly, the theoretical uncertainties on the branching ratios of Higgs decays to $b\bar{b}$ (+1.7% / -1.73%) and $\gamma\gamma$ (+2.9% / -2.84%) are applied on all relevant processes.

Table 4.5 recaps the different types of theoretical systematic uncertainties and which effect is taken into account.

Process	QCD	PDF	Parton Shower	BR($H \to \gamma\gamma$)	BR($H \to b\bar{b}$)
ttH	Shape+Norm	Shape+Norm	Shape+Norm	Norm	-
ZH	Shape+Norm	Shape+Norm	Shape+Norm	Norm	-
ggF H	Norm	Norm	-	Norm	-
$tHjb$	Norm	Norm	-	Norm	-
gg ZH	Norm	Norm	-	Norm	-
VBF H	Norm	Norm	-	Norm	-
bbH	Norm	Norm	-	Norm	-
tHW	Norm	Norm	-	Norm	-
$ggHH$	Norm	Norm	Shape+Norm	Norm	Norm
VBF HH	Norm	Norm	-	Norm	Norm
$\gamma\gamma$ + jets	Shape	Shape	Shape	-	-
$Z(\to q\bar{q})\gamma\gamma$	Shape+Norm	Shape+Norm	-	-	-
Signals	Not computable	Shape+Norm	Norm	-	-

Table 4.5: Different sources of theoretical systematic uncertainties and how they are applied, either only on the normalisation or both on the normalisation and the PNN distribution shape.

4.3.2 $\gamma\gamma$ + jets theoretical uncertainties

Uncertainties on the non-resonant di-photon background hold a particular importance since it is the largest background in terms of number of events. As seen in Table 4.2 and 4.3, the yields in sidebands differ between simulation and data. To account for this, a scale factor is applied to correct the yields in the signal region. The factor is obtained by a data background-only fit in the sidebands which actually corresponds to the ratio between the number of $\gamma\gamma$ + jets events obtained by data and by simulation. It is computed to be 1.26 ± 0.03 in the 2 b-tagged jet region and 1.03 ± 0.01 in the 1 b-tagged one.
Since the normalisation is imposed by the control region, only the impact on the shape of the PNN distribution is considered for the uncertainties related to the $\gamma\gamma$ + jets sample. A first uncertainty is assessed to account for the extrapolation of this scale factor which is supposed to be the same in the sidebands and in the SR. It is assimilated as the uncertainty on the ratio between yields in the SR and the SB with the MC $\gamma\gamma$ Sherpa sample. It depends on the other theoretical uncertainties on QCD, PDF and α_s which are added in quadrature to give a scale uncertainty of 1.9% and 6.6% in the 1 and 2 b-tagged region respectively.
The QCD scale, PDF and α_s uncertainties on the shape are evaluated in the same way as the other processes discussed in the previous section. A global "$\gamma\gamma$-modelling" uncertainty is considered to take into account the fact that the MC generator does not perfectly model the $\gamma\gamma$ + jets background. It is evaluated by comparing the nominal Sherpa sample to an alternative one generated by MadGraph. This comparison thereby encompasses the parton shower uncertainty between different event generators.

Figure 4.10 shows that the $m_{b\bar{b}}$ and $m_{b\bar{b}\gamma\gamma}$ distributions of the two samples have a 10-20% difference in each bin which can be as large as 100% at very large masses.

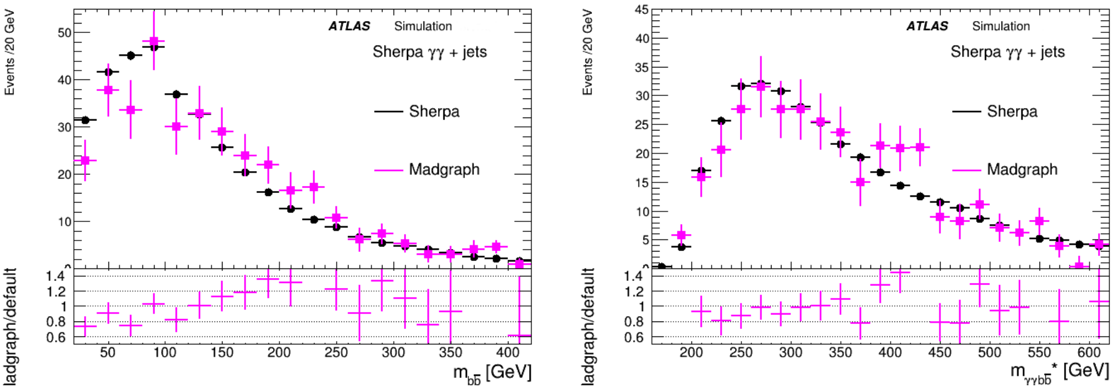

(a) (b)

Figure 4.10: $m_{b\bar{b}}$ (a) and $m_{b\bar{b}\gamma\gamma}$ (b) distributions of $\gamma\gamma$ + jets events generated with Sherpa (black) and Madgraph (pink) in the 2 b-tagged region SR. Both distributions are normalised to the same area and the ratio is shown in the bottom panels.

This explains why the $\gamma\gamma$-modelling is the largest uncertainty of the analysis since these kinematic distributions are used by the PNN discriminant.
The impact on the limit of the theoretical and experimental uncertainties, and in particular of $\gamma\gamma$ modelling, will be shown in Section 4.4.3.

4.3.3 Experimental systematic uncertainties

Experimental systematic uncertainties take into account all the detector effects on the measure of physical signals that lead to the measurement.
They are computed using dedicated MC samples where parameters are shifted by a $\pm 1\sigma$ variation from the corresponding uncertainty The uncertainties considered can be regrouped based on the objects that they affect :

- A 0.83% global uncertainty on the integrated luminosity is applied to the normalisation of all processes [141].
- Event-based uncertainties include the systematics on photon trigger and the pile-up reweighting.
- Uncertainties on photons encompass the variations of their identification and isolation and on the energy scale and resolution.
- Jet systematic uncertainties take into account energy scale and resolution variations as well as primary vertex uncertainties.
- Flavour tagging uncertainties gives the indetermination on the scale factor calibrating the rejection and the b-jet efficiency at a given working point.

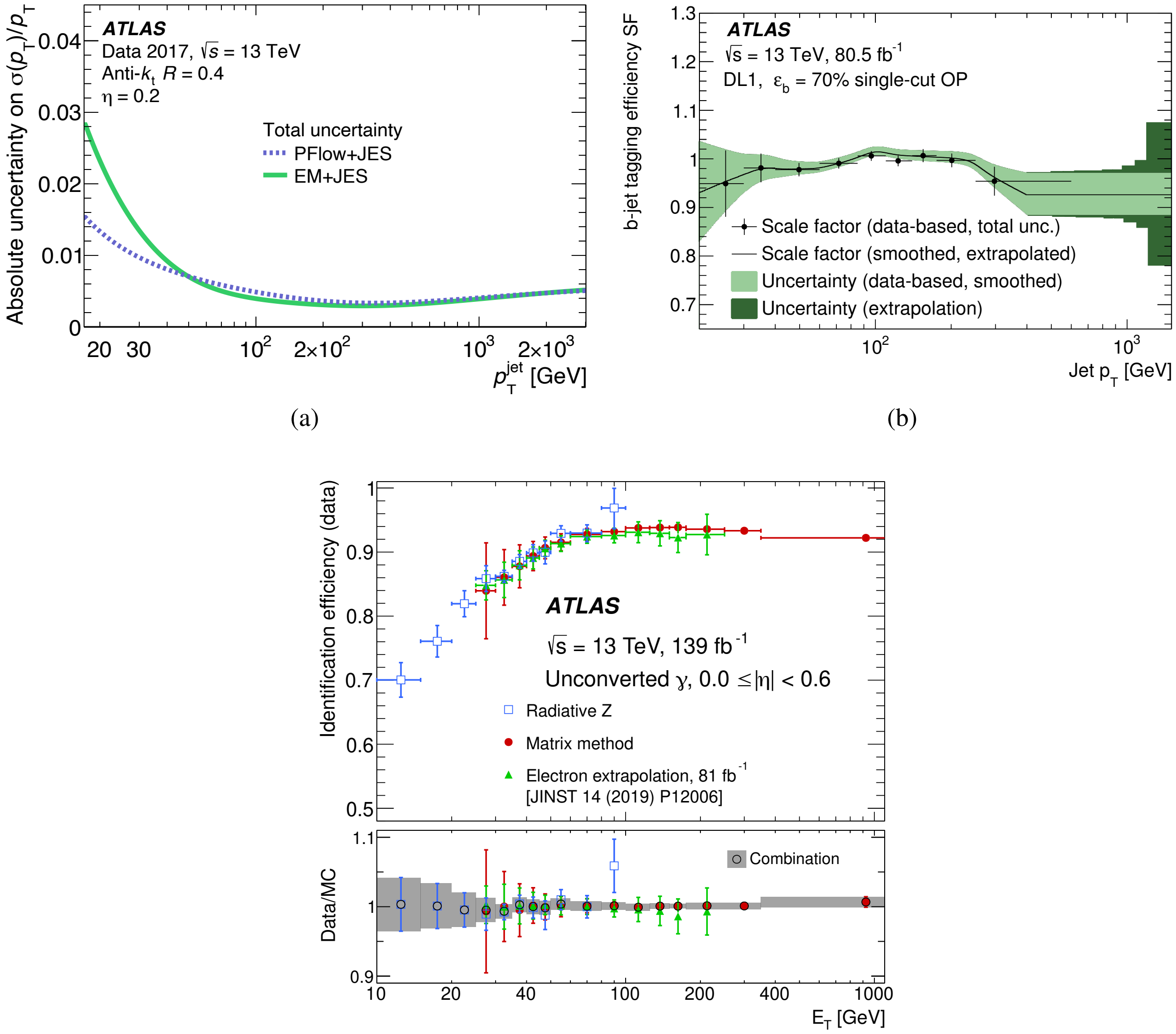

(a)

(b)

(c)

Figure 4.11: (a) Jet energy resolution [115], (b) flavour tagging uncertainties (the green band) depending on the jet p_T [138] and (c) unconverted photon identification uncertainties (the grey band) as a function of photon E_T [110]. Note that for flavour tagging this is not the tagger nor working point used in the analysis but the trend is similar nonetheless.

Various schemes are applied to reduce the number of nuisance parameters which are still 48 in the end. The eigenvector decomposition method is used for instance for flavour tagging [150] and jet energy scale and resolution [115]. The result is a reduced number of orthogonal nuisance parameters associated to eigenvalues. For instance, the full JER scheme is used for jet energy resolution (JER) uncertainties It comes from a smearing process obtained from the JER calibration described in Subsection 2.3.3 and reduces the number of NP to 11.

These uncertainties are dependant on the energy of the measured particles. Figure 4.11 illustrate the relation between flavour tagging, jet energy resolution and photon identification uncertainties and the particle p_T or E_T. This means for instance that the jets b-tagging and JER uncertainties decrease with p_T in the energy range of the analysis.

The experimental systematic uncertainties have an impact on both the normalisation and the shape of the PNN distribution. The only exception is for the $\gamma\gamma$ + jets samples where the normalisation is imposed by the control region, therefore only shape variations are taken into account similarly to theoretical uncertainties.

They are evaluated on the signal, $\gamma\gamma$ + jets, ttH, ZH (both gluon-gluon fusion and Higgsstrahlung production modes), ggH, $tHjb$, $Z(\to q\bar{q})\gamma\gamma$ and ggF and VBF HH samples. Experimental uncertainties are not taken into account for other smaller background because their yields are too low to have an impact on the analysis result.

		2 b-tagged SR yield uncertainty (%)							
	Source	ttH	ZH	ggHH	ggH	ggZH	$tHjb$	VBFHH	$Z(\to q\bar{q})\gamma\gamma$
Event-based	Photon Trigger	1.01	1.02	1.00	1.04	0.98	1.03	1.02	1.60
	Pile-up reweighting	0.88	0.76	0.56	0.43	0.60	0.99	0.60	3.86
Photon	Photon Energy Res.	0.42	0.42	0.34	0.42	0.43	0.63	0.43	2.90
	Photon Energy Scale	0.17	0.18	0.12	0.07	0.11	0.18	0.24	14.56
	Photon ID	1.59	1.61	1.44	1.64	1.49	1.60	1.59	2.59
	Photon Isolation	1.55	1.57	1.45	1.60	1.46	1.59	1.59	2.27
Jet	Jet Energy Scale	1.36	0.94	0.55	1.81	0.74	0.76	0.72	5.41
	Jet Energy Resolution	7.33	4.60	2.91	7.50	3.36	4.88	3.08	5.41
Flavour-tagging	b-jet efficiency	2.07	2.99	2.51	3.05	2.55	2.30	2.83	3.36
	c-jet efficiency	0.40	0.71	0.06	1.68	0.60	0.92	0.07	13.12
	light-jet efficiency	0.79	0.38	0.40	2.72	0.51	0.90	0.42	1.91

		1 b-tagged SR yield uncertainty (%)							
	Source	ttH	ZH	ggHH	ggH	ggZH	$tHjb$	VBFHH	$Z(\to q\bar{q})\gamma\gamma$
Event-based	Photon Trigger	1.01	1.02	1.00	1.00	1.01	1.06	1.01	1.75
	Pile-up reweighting	0.75	0.44	0.49	0.34	0.36	0.91	0.51	1.29
Photon	Photon Energy Res.	0.45	0.46	0.36	0.46	0.36	0.39	0.41	1.35
	Photon Energy Scale	0.21	0.19	0.16	0.19	0.18	0.32	0.11	2.32
	Photon ID	1.60	1.65	1.47	1.65	1.52	1.64	1.60	2.77
	Photon Isolation	1.57	1.61	1.47	1.60	1.50	1.61	1.57	2.66
Jet	Jet Energy Scale	1.30	1.04	0.51	2.04	0.58	0.61	0.49	0.89
	Jet Energy Resolution	5.23	4.91	2.88	8.17	3.01	3.06	2.64	5.99
Flavour-tagging	b-jet efficiency	0.68	0.48	1.31	0.42	0.67	0.41	0.86	0.57
	c-jet efficiency	0.32	1.59	0.05	2.19	1.45	0.15	0.07	4.03
	light-jet efficiency	0.74	1.15	0.44	3.60	1.28	0.55	0.46	2.88

Table 4.6: Background samples yield uncertainty in the SR (in %) in the (top) 2 b-tagged and (bottom) 1 b-tagged jet region.

Yields and shape changes Table 4.6 presents the yields change for backgrounds samples in the 1 and 2 b-tagged jet signal regions. A few modifications have been made in these tables in order to ease the reading : the up and down variations have been symmetrised and the variations NP from different schemes are added in quadrature even if they are still considered separately in the statistical framework. The dominating systematic uncertainties are related to flavour tagging and jet energy resolution. They have an impact on the normalisation between 2 and 7%.

For signal samples, the variations are depending on the considered mass point. Figure 4.12 shows the quadratically summed yields changes for the simulated signal samples main systematics : photons and event-based (top), jet energy resolution (middle) and flavour tagging (bottom). Photon and event-based variations are around 3% and are relatively independent from the mass whereas for flavour tagging, the yield change can vary by a factor five from 1 to 5%. Similarly, jet energy resolution variations range from 1 to 13%. This is because jets are more boosted and have a larger transverse impulsion when $m_S \ll m_X$ or for large values of m_X which decreases the uncertainties as seen in Figure 4.11. On the other hand, the signal photons all come from the Higgs boson decay and therefore have all the same energy distribution which explains the flat uncertainty.

Shape uncertainties are taken into account in addition to normalisation for experimental systematic uncertainties. A subset of nominal and up and down variations distribution for signal, $\gamma\gamma+$ jets and ZH samples are displayed in Figure 4.13 and 4.14. They show the impact of two of the main nuisance parameters, one related to flavour tagging and the other one to the jet energy resolution.

A last type of uncertainty that must be taken into account is the signal interpolation for the relevant mass points. The envelope of the parameters of the signal's Bukin shape is used to provide an uncertainty on the shape and the normalisation of the interpolated signal PNN distribution.

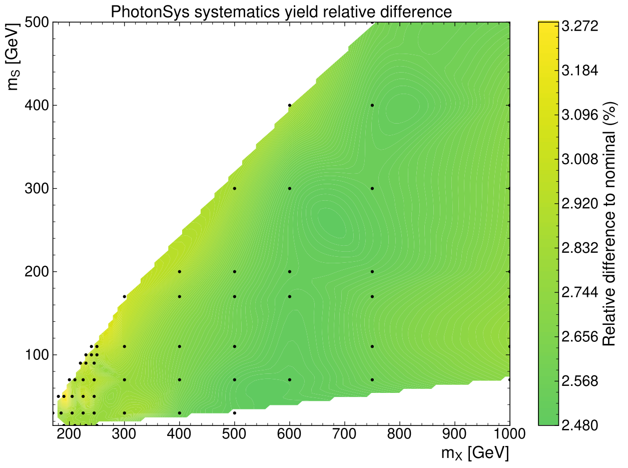

(a) Photon and event-based variations

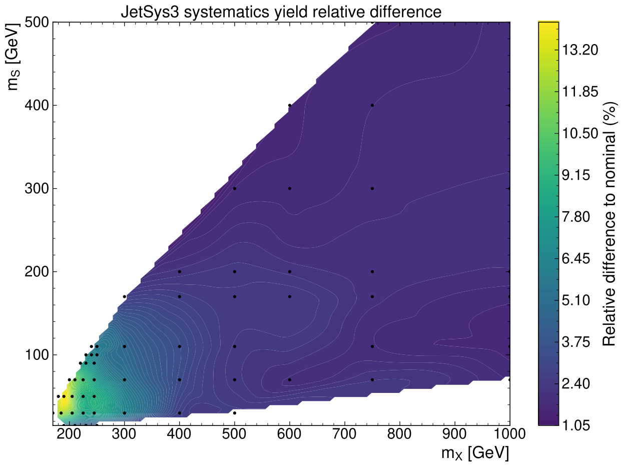

(b) Jet energy resolution variations

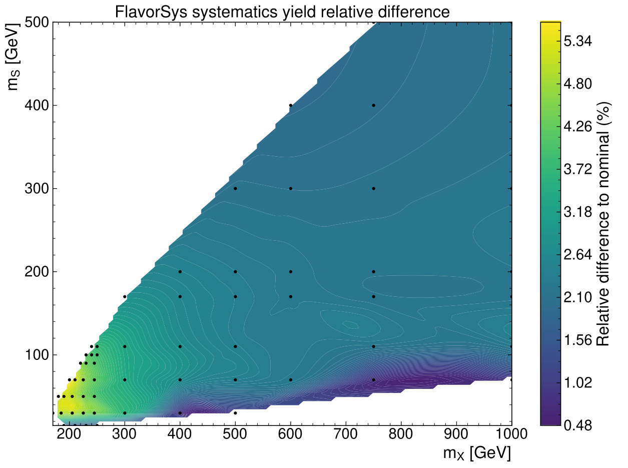

(c) Flavour tagging variations

Figure 4.12: Signal yields variations of major systematic uncertainties in the (m_X, m_S) mass plane.

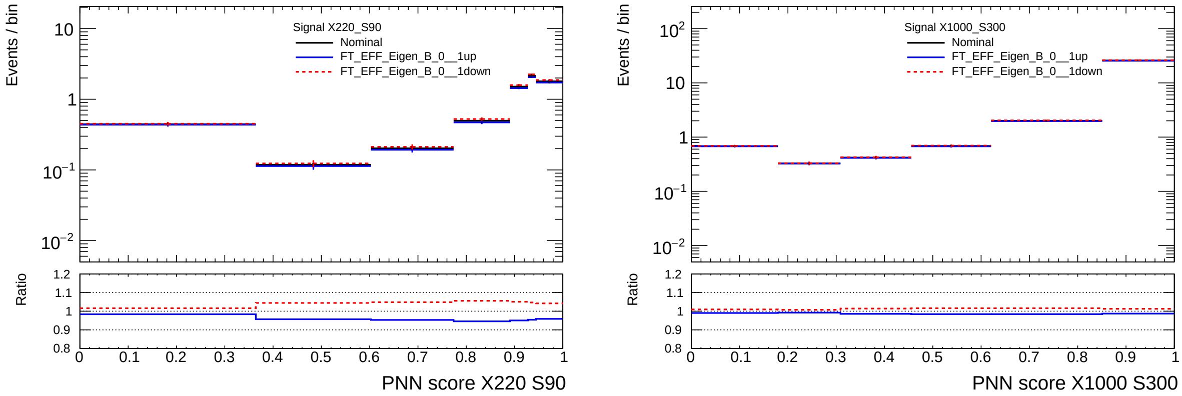

(a) SH signal, (m_X, m_S) = (220, 90) GeV (b) SH signal, (m_X, m_S) = (1000, 300) GeV

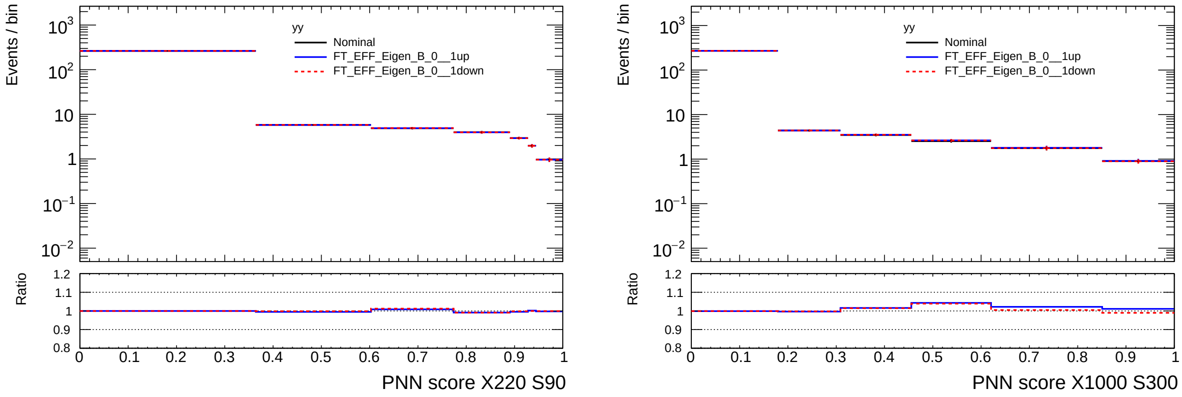

(c) $\gamma\gamma$, (m_X, m_S) = (220, 90) GeV (d) $\gamma\gamma$, (m_X, m_S) = (1000, 300) GeV

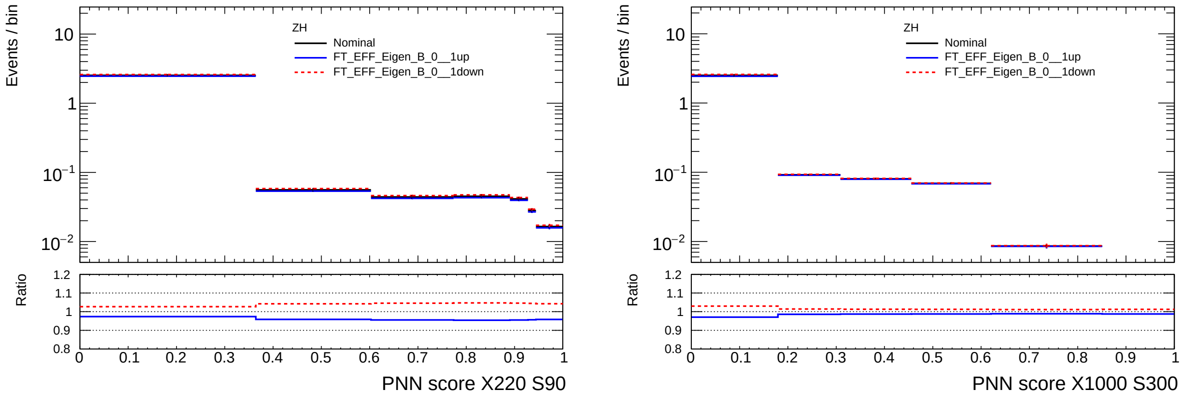

(e) ZH, (m_X, m_S) = (220, 90) GeV (f) ZH, (m_X, m_S) = (1000, 300) GeV

Figure 4.13: PNN score distribution of signal, $\gamma\gamma$ and ZH samples and impact of the NP associated to the first b-tagging uncertainty eigenvalue for (m_X, m_S) = (220, 90) GeV (left) and (m_X, m_S) = (1000, 300) GeV (right).

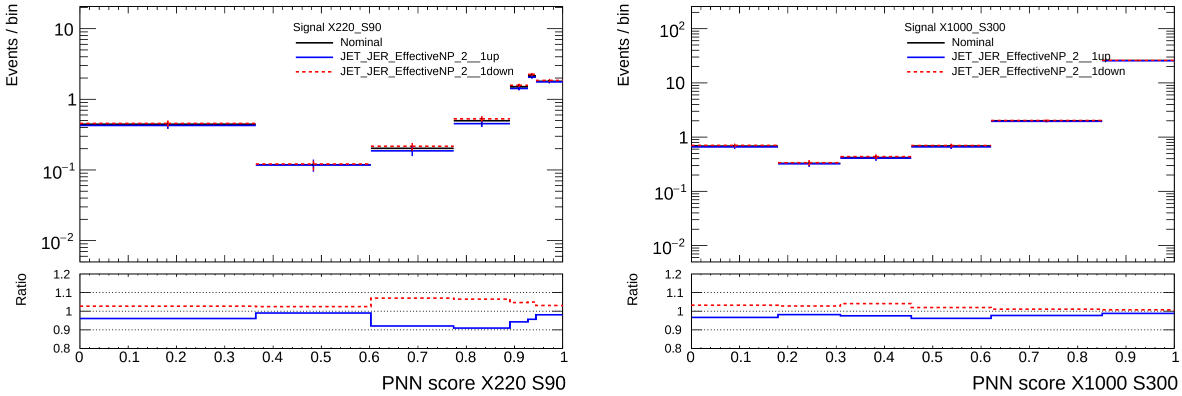

(a) SH signal, (m_X, m_S) = (220, 90) GeV (b) SH signal, (m_X, m_S) = (1000, 300) GeV

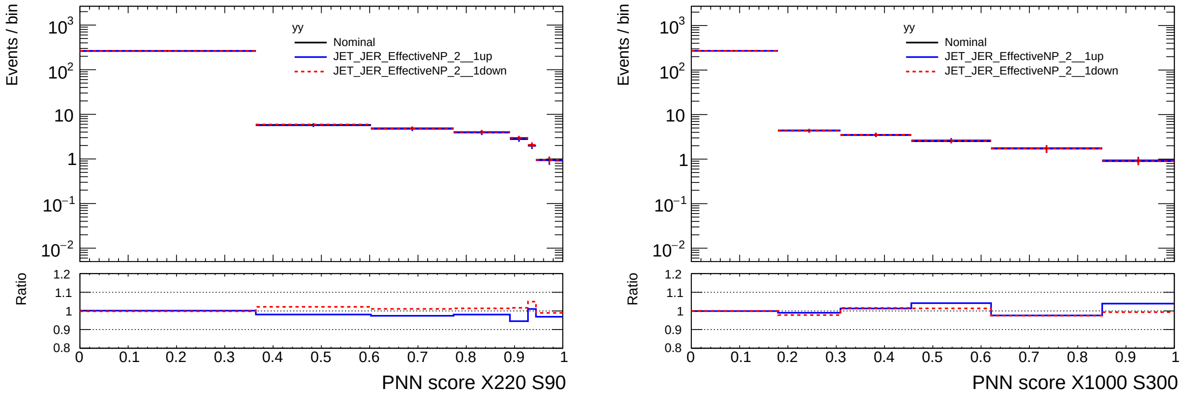

(c) $\gamma\gamma$, (m_X, m_S) = (220, 90) GeV (d) $\gamma\gamma$, (m_X, m_S) = (1000, 300) GeV

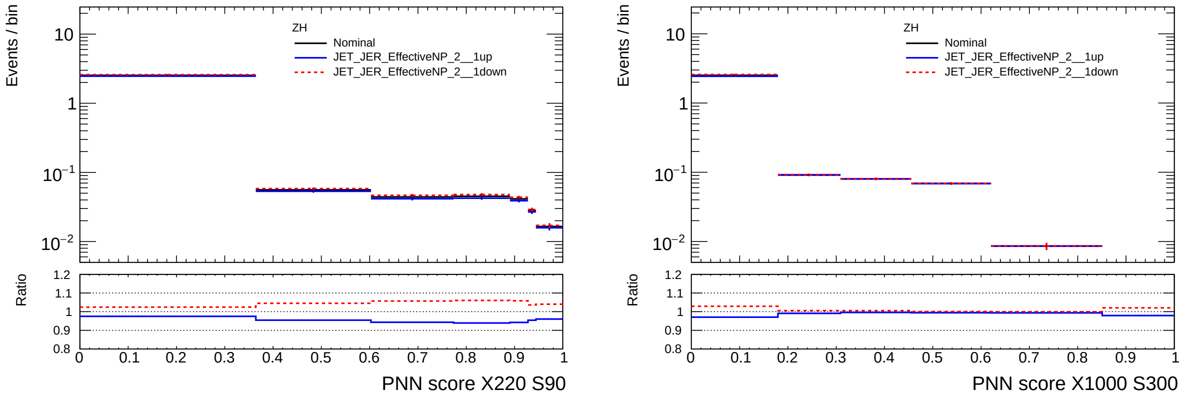

(e) ZH, (m_X, m_S) = (220, 90) GeV (f) ZH, (m_X, m_S) = (1000, 300) GeV

Figure 4.14: PNN score distribution of signal, $\gamma\gamma$ and ZH samples and impact of the NP associated to the second JER uncertainty eigenvalue for (m_X, m_S) = (220, 90) GeV (left) and (m_X, m_S) = (1000, 300) GeV (right).

4.4 Results

4.4.1 Control region data/MC agreement

The discrepancy between data and simulation normalisation in the sidebands (Tables 4.2 and 4.3) shows that the modelling of the background, and in particular the continuum diphoton one, by the simulation must be considered with caution. It is therefore crucial to check that the PNN distributions are consistent between data and MC samples once scaled to make sure that the PNN is correctly processing the data.
The agreement between simulation and data is made in the control region sidebands. $m_{b\bar{b}}$, p_T^b, $m^*_{b\bar{b}\gamma\gamma}$, and $m^*_{b\gamma\gamma}$ distributions are checked first to see the agreement between these kinematic variables which are the inputs of the PNNs. Figure 4.15 shows the latter two. They are followed by PNN distributions for different mass points and two of them are illustrated in Figure 4.16. Good agreement is observed between data and simulation in both the 2 b-tagged and 1 b-tagged region. The differences between them fall within the simulation uncertainties which are dominated by the $\gamma\gamma$ modelling.

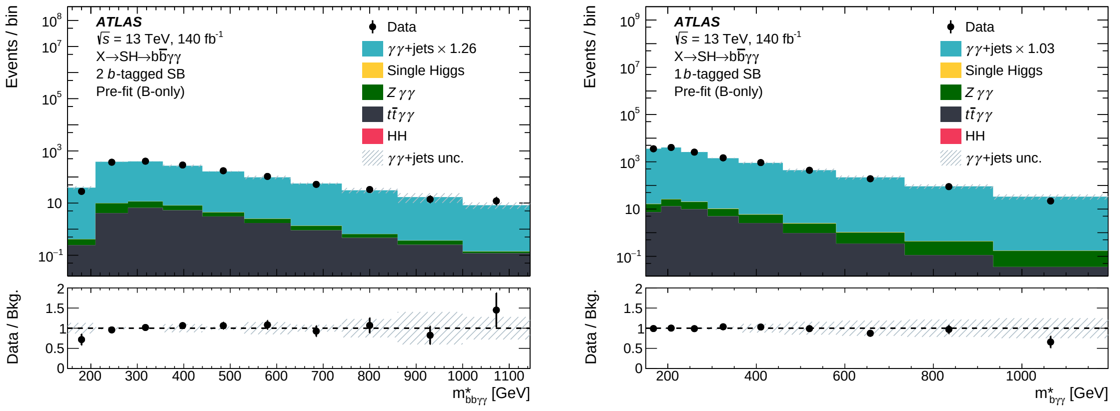

(a) (b)

Figure 4.15: Distributions of $m^*_{b\bar{b}\gamma\gamma}$ (left) and $m^*_{b\gamma\gamma}$ (right) in the sidebands of the 2 and 1 b-tagged region respectively for simulation and data. The $\gamma\gamma$ + jets background is rescaled to its post-fit normalisation in a background-only fit. The $\gamma\gamma$ + jets category represents the sum of $\gamma\gamma$ + jets, γ + jets and dijet backgrounds. The error band corresponds to the dominant uncertainty, which arises from the $\gamma\gamma$ modelling [9].

4.4.2 Statistical model

The results of the analysis are computed through a maximum likelihood fit on the binned PNN distribution.
In each bin i, the number of events in the data $n_{\mathrm{SR},i}$ is compared to the expected number

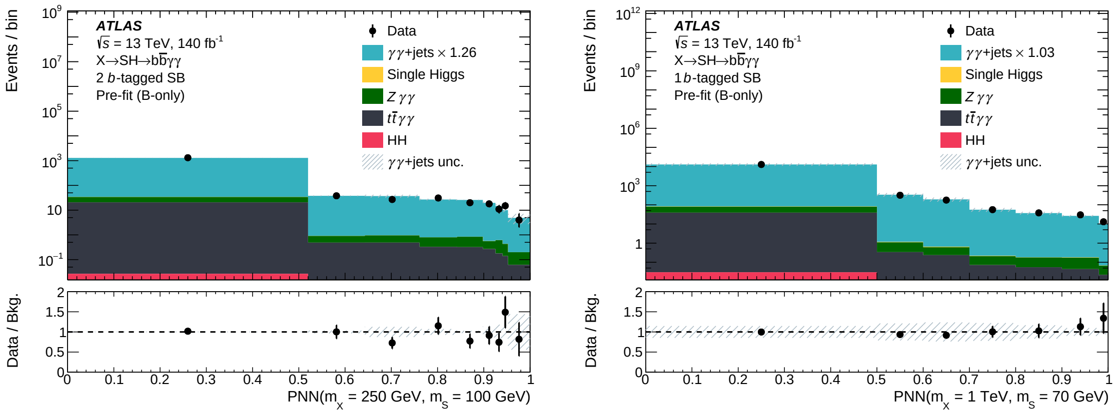

(a) (b)

Figure 4.16: Sidebands PNN distributions for two example of (m_S, m_X) points for simulation and data in the merged (left) and resolved region (right). The $\gamma\gamma +$ jets background is rescaled to its post-fit normalisation with a background-only fit. The $\gamma\gamma +$ jets category represents the sum of $\gamma\gamma +$ jets, $\gamma +$ jets and dijet backgrounds. The error band corresponds to the dominant uncertainty, which arises from the $\gamma\gamma$ modelling [9].

of events through a Poisson law. The expected number of events of each process p $N^p_{\mathrm{SR}} f^p_i$ depends on the shape of the PNN distribution in the bin f^p_i. The fit also goes through the number of events in the sidebands to fit the $\gamma\gamma +$ jets normalisation and takes into account the uncertainties in the form of nuisance parameters $\boldsymbol{\theta}$ which are constrained by the function $G(\boldsymbol{\theta})$. Putting all this together, the likelihood is :

$$\begin{aligned} L = &\mathrm{Pois}\left(n_{\mathrm{SB}} \middle| \mu_{\gamma\gamma} N^{\gamma\gamma}_{\mathrm{SB}}(\boldsymbol{\theta}) + \sum_p N^p_{\mathrm{SB}}(\boldsymbol{\theta}) \right) \\ &\cdot \prod_i \mathrm{Pois}\left(n_{\mathrm{SR},i} \middle| \mu_{\gamma\gamma} N^{\gamma\gamma}_{\mathrm{SR}}(\boldsymbol{\theta}) f^{\gamma\gamma}_i(\boldsymbol{\theta}) + \sum_p N^p_{\mathrm{SR}}(\boldsymbol{\theta}) f^p_i(\boldsymbol{\theta}) \right) \cdot G(\boldsymbol{\theta}) \end{aligned} \tag{4.1}$$

The binning used in the fit is made so that there is always more than 1 expected background event in the last bin which is the most sensitive to signal. This is to ensure that the asymptotic approximation used later for the limit computation is valid. For the mass points in the resolved region, the bins sizes is further optimized so that, starting from the most signal-like bin, each bin have one more expected background event than the previous one.

The free parameter of the fit is the signal strength μ_{sig}. The best-fit value $\hat{\mu}$ maximizes the likelihood L. The following test statistics can be defined to compare the background-only to a signal of strength $\widehat{\mu}$ hypothesis [151] :

$$q_0 = -2\ln \frac{L(\mu = 0, \hat{\hat{\boldsymbol{\theta}}}(\mu = 0))}{L(\hat{\mu}, \hat{\boldsymbol{\theta}})} \tag{4.2}$$

The significance which is $Z = \sqrt{q_0}$ under the asymptotic approximation can then be computed. It characterizes the likeliness of an excess in data to come from a true signal of strength $\hat{\mu}$.

If no signal is observed, upper limits are set on the signal cross section multiplied by the branching ratio to the $b\bar{b}\gamma\gamma$ final state. The $\mathrm{CL_S}$ method using the asymptotic approximation is used [152] :

$$\mathrm{CL_S} = \frac{p_{s+b}}{1 - p_b} \tag{4.3}$$

where p_i is the p-value for scenario i, either signal + background or background only. A scenario is said to be excluded at the 95% confidence level (CL) if $\mathrm{CL_S} < 0.05$. The cross section upper limits are then defined as the highest cross section a signal can have before being excluded. A scan on the signal strength is performed on every probed mass point to compute the corresponding maximum upper limit.

4.4.3 Blinded results and systematic uncertainties impact

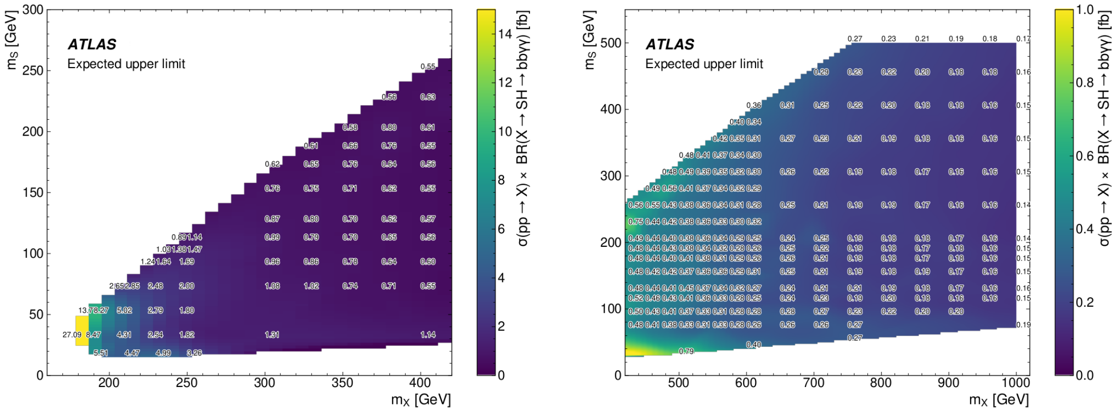

(a)

(b)

Figure 4.17: Blinded expected limits on the signal cross-section times $b\bar{b}\gamma\gamma$ branching ratio for the different (m_X, m_S) signals in the (a) low m_X or (b) high m_X region.

To evaluate the sensitivity of the analysis, fits are performed when data is still blinded in the signal region with an Asimov dataset equal to the expected background. These

fits are performed in the SR only and directly use the rescaling factor computed in Subsection 4.3.2 to normalize the non-resonant photon background distribution.
As shown in Figure 4.17, the blinded expected limits range from 27 fb at m_X = 170 GeV to 0.14 fb at m_X = 1000 GeV. At low m_X, the sensibility of the analysis is affected by a lower signal selection efficiency due to a larger proportion of b-jets falling below the jet p_T reconstruction threshold. On the other hand, the sensibility of the analysis is increasing with higher m_X values because the background decreases whereas the signal selection efficiency remains constant.

The impact of the systematic uncertainties on the analysis final results can be evaluated by comparing the blinded upper limits from Figure 4.17 with limits obtained when they are not taken into account as nuisance parameters in the fit.

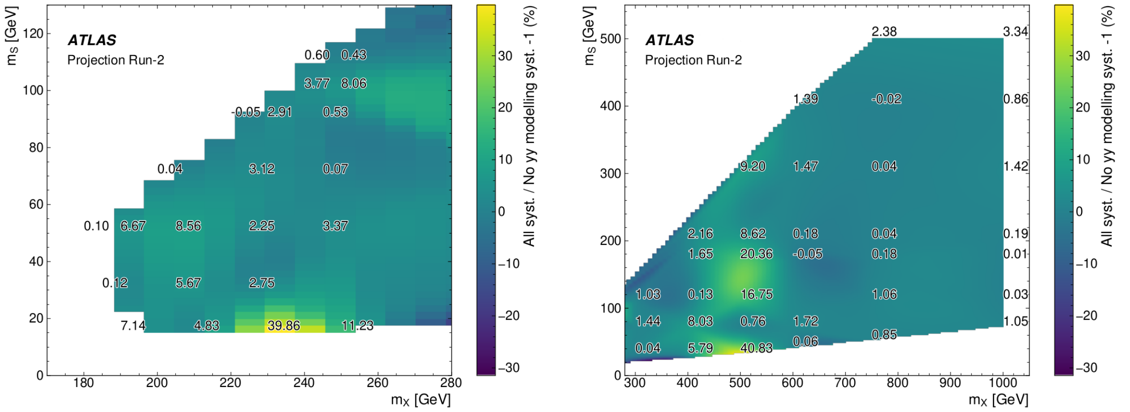

(a) (b)

Figure 4.18: Relative difference (in %) between blinded expected limits with and without taking into account $\gamma\gamma$ modelling uncertainty in Monte-Carlo points for (a) low and (b) high m_X values.

The $\gamma\gamma$ modelling impact evaluated using this method is displayed in Figure 4.18. It is the largest source of uncertainty of the analysis. This is because it is evaluated by comparing an alternative MadGraph MC sample with the nominal Sherpa one. Due to the MadGraph sample having far less events, statistical fluctuations may arise in the comparison from one point to another. This can lead to a very large impact on the upper limits which can reach 20% for (m_X, m_S) = (500, 170) GeV in the 2 b-tagged jet region and 40 % for (m_X, m_S) = (500, 30) and (230, 15) GeV in the 1 b-tagged jet region. In the rest of the mass space, the impact is below 8%.

Similarly, the theoretical systematic uncertainties impact, which includes $\gamma\gamma$ modelling, is shown in Figure 4.19. The plot can be superimposed very well with the one with the $\gamma\gamma$ modelling impact, showing that it is the dominating uncertainty. Other theoretical uncertainties account for a limit increase of around 3-4%. To see which theoretical

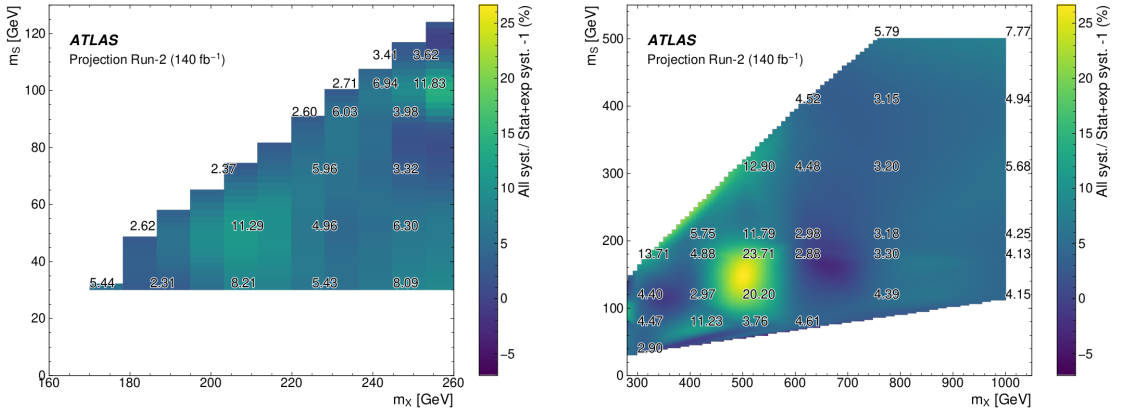

(a)

(b)

Figure 4.19: Relative difference (in %) between blinded expected limits with and without taking into account theory systematic uncertainties in 2 b-tagged Monte Carlo points for (a) low and (b) high mass.

uncertainties are important beside the $\gamma\gamma$ modelling, a similar limit comparison is done on a subset of points from the mass space. Single Higgs theory uncertainties have a limited impact which is below 0.4%. Uncertainties affecting signal have a larger repercussion at around 5%

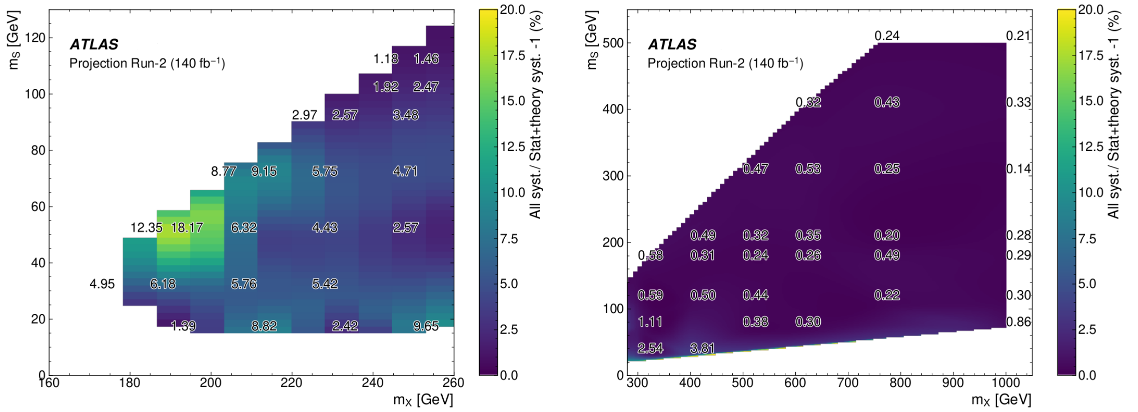

(a)

(b)

Figure 4.20: Relative difference (in %) between blinded expected limits with and without taking into account experimental systematic uncertainties in 2 b-tagged Monte-Carlo points in the (a) low and (b) high m_X region.

Lastly, the impact of experimental systematic uncertainties in the resolved region is evaluated in Figure 4.20. In the low m_X region, the impact on the limit can reach up to 18% because of the jet energy resolution and flavour tagging uncertainties are large in this area as discussed in Section 4.3.3. For large values of m_X, however, the impact is really small and remains below 1%.

Another way to evaluate the uncertainties impact is to check their effect on the fit directly. This can be done with *ranking plots* which ranks the post-fit impact on the signal strength of every nuisance parameter θ. They are calculated by fixing the parameter to its $\pm 1\sigma$ values, fixing all other parameters to their nominal values, re-fitting the signal strength, and evaluating its change with respect to the nominal fit. The pulling of the nuisance parameters is defined as the shifted and scaled post-fit values of the nuisance parameters. Combined pulls and ranking plots still evaluated on blinded data of two points, one in each of the 1 and 2 b-tagged jet region, are shown in Figure 4.21. The plots confirm the insights from the limit tests, as the largest uncertainty is the $\gamma\gamma$-modelling. Signal theoretical parton shower modelling uncertainties are also important. Largest experimental uncertainties come from jet energy resolution ("JER JER EffectiveNP") or flavour tagging ("FT EFF Eigen B/C").

4.4.4 Unblinded results

Results of the background-only fit of the PNN distribution on two examples probed mass points, one in each of the 1 and 2 b-tagged jet region, are showed in Figure 4.22.

The discovery tests are performed to find the local observed significance for every (m_X, m_S) couple probed. The resulting two dimensional map is given in Figure 4.23. The results in the white band at m_S = 125 GeV are not presented here and in the following results plots, as S would correspond to the SM Higgs boson in this case. This research is already performed in the resonant $HH \to b\bar{b}\gamma\gamma$ analysis [74].

The data agrees is most cases with the Standard Model background only hypothesis. However some small discrepancies arise and the largest deviation appears for (m_X, m_S) = (575, 200) GeV where the observed local significance is 3.55σ. The post-fit PNN distribution is shown in Figure 4.24 where the data shows a potential excess with respect to background in the most signal-like bins of the PNN distribution close to 1.

This local excess must be confronted to the *look-elsewhere effect* which takes into account the fact that a large number of discovery tests are done, which increases the probability of an excess due to statistical fluctuations. To do so, a study is performed to compute the global significance following the procedure described in [153]. The global significance broadly corresponds to the probability of a test statistics $q_0(\theta)$ to be higher than the excess than we observe ($q_0^{obs} = 3.55\sigma$) in any point that we probe under the background only hypothesis. Under the asymptotic approximation, it can be evaluated by computing the Euler characteristic of the set of points that verify $q_0(\theta) > q_0^{obs}$ on a set of simulated background-only toys dataset. With this method, the global significance is computed to be 2.0σ, making this local excess not statically significant.

Upper limits can then be set on the signal production rate in the $b\bar{b}\gamma\gamma$ final state following the procedure described in Subsection 4.4.2. The limits are shown in the (m_X, m_S) plane in Figure 4.25. Given the good agreement between data and the background only hypothesis, the observed limits are close to the expected ones. They range from 39

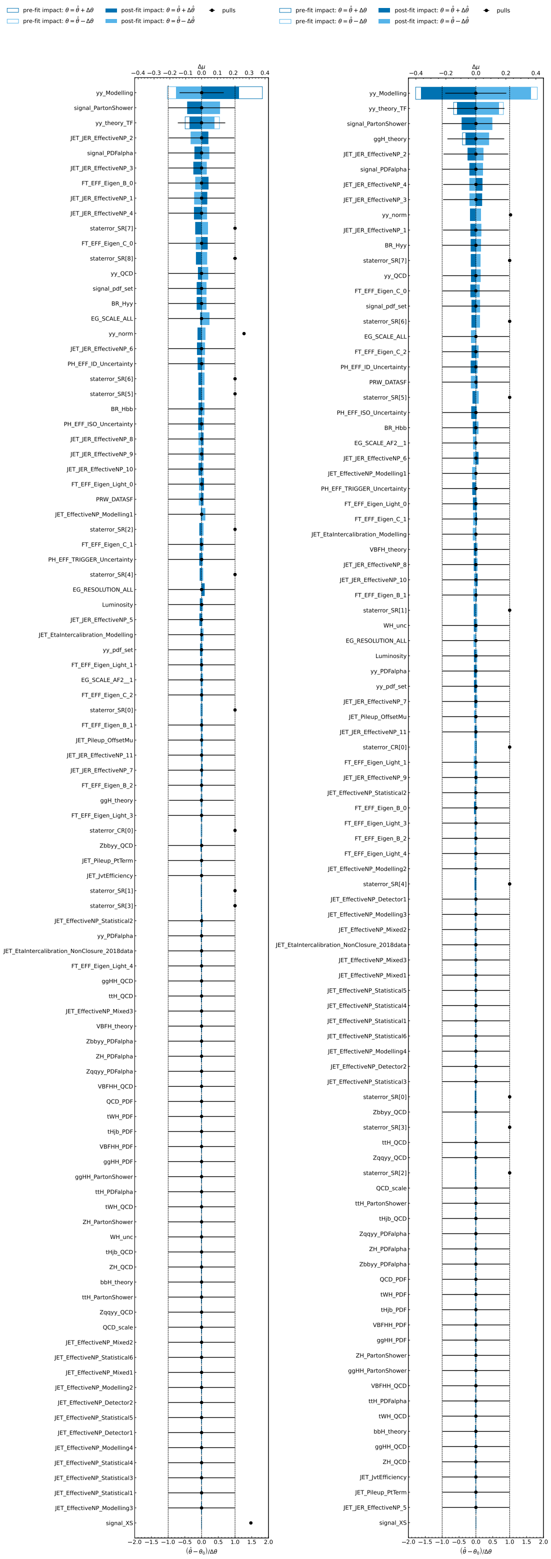

(a) (b)

Figure 4.21: Nuisance parameters and their pulls ranked by their impact on the fitted signal strength $\Delta\mu$ for (a) (m_X, m_S) = (250, 100) GeV and (b) (m_X, m_S) = (230, 15) GeV

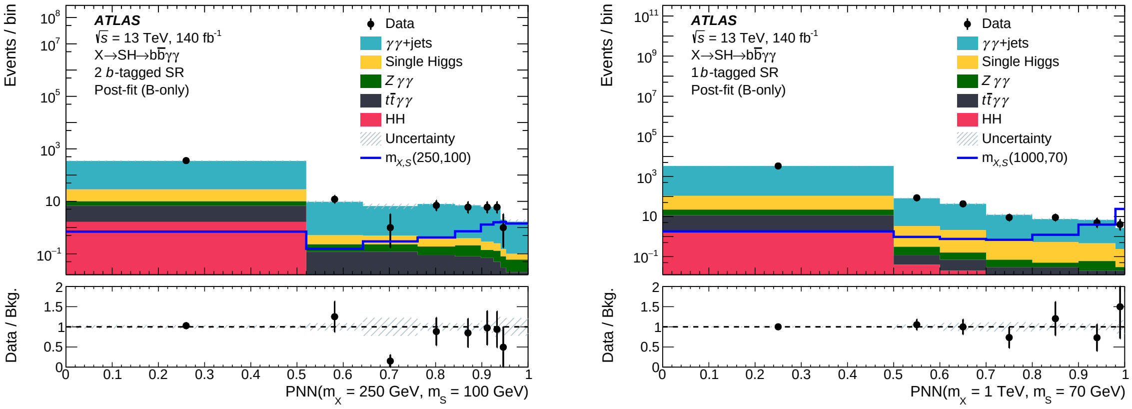

(a) (b)

Figure 4.22: Post-fit distributions of the PNN discriminant output in the (a) 2 *b*-tagged signal region for (m_X, m_S) = (250, 100) GeV and (b) 1 *b*-tagged signal region for (m_X, m_S) = (1000, 70) GeV, after a background-only fit to data. The probed signals are illustrated for comparison with a 1 fb cross section. The error band corresponds to the total systematic uncertainty after fit.

(25 expected) fb at m_X = 170 GeV and m_S = 30 GeV to 0.09 (0.14) fb at m_X = 1000 GeV and m_S between 250 and 300 GeV. Similarly to the expected limits, the observed upper limits are larger in the high mass region where signal is easier to distinguish from a smaller background. On the other hand, at low mass, the signal efficiency gets hindered by the jet reconstruction which reduces the sensitivity of our search.

A particular point of interest is the excess noticed by the CMS experiment study [6] at (m_X, m_S) = (650, 90) GeV where a local significance for signal discovery of 3.8σ is computed. This reduces to an excess below 2.8σ when taking into account the *look-elsewhere effect*. Our analysis would be sensible to such an excess as it was checked that a signal injection with a production cross section equal to the best fit value determined by CMS would lead to a signal significance of 2.7σ. However, no excess with respect to the background only hypothesis is observed for this point as the *p*-value is larger than 0.5. The upper limit set at the 95% CL is 0.2 fb compared to the 0.64 fb observed by CMS.

The search for two additional scalar particles *X* and *S* in the $X \to SH \to b\bar{b}\gamma\gamma$ channel presented in this chapter has allowed to set upper limits on a wide range of masses. The space with m_X and m_S below 250 and 50 GeV respectively is notably probed for the first time. This has been made possible thanks to the interpolation method which allowed the PNN discriminant to target signals it has not been trained with. The results show a local excess for the (m_X, m_S) = (575, 200) GeV at the 3.55σ significance level which reduces to 2.0σ when taking into account the *look-elsewhere effect*. The research also helped to clarify on the excess reported for the same process by the CMS collaboration at (m_X, m_S) = (650, 90) GeV. We report no deviation with the background only hypothesis for this

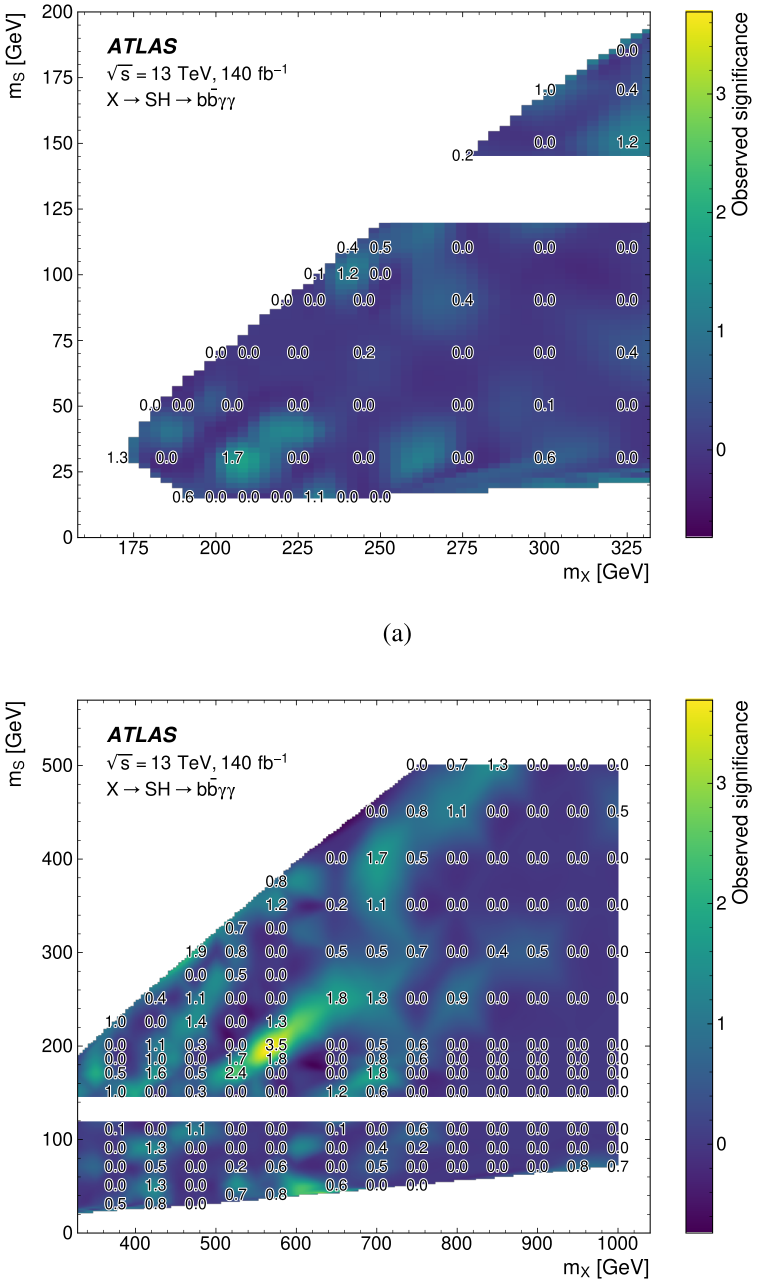

(a)

(b)

Figure 4.23: Local observed significance for signal discovery for all probed (m_X, m_S) values in the (a) low m_X and (b) high m_X regions.

point.

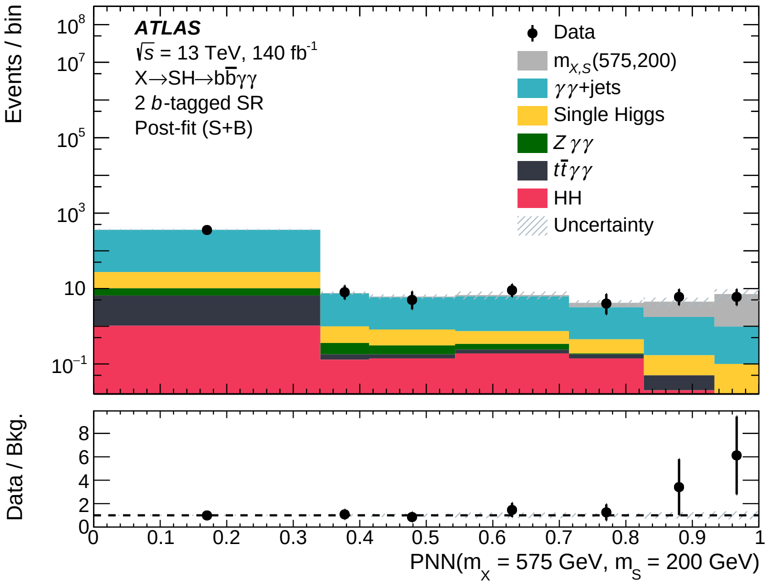

Figure 4.24: $(m_X, m_S) = (575, 200)$ GeV PNN distribution after a signal-plus-background fit in the 2 b-tagged signal region. It is the mass point for which the most significant deviation between data and SM-only prediction is observed. The signal distribution in grey corresponds to the best fit value signal strength. The error band corresponds to the total systematic uncertainty after fit.

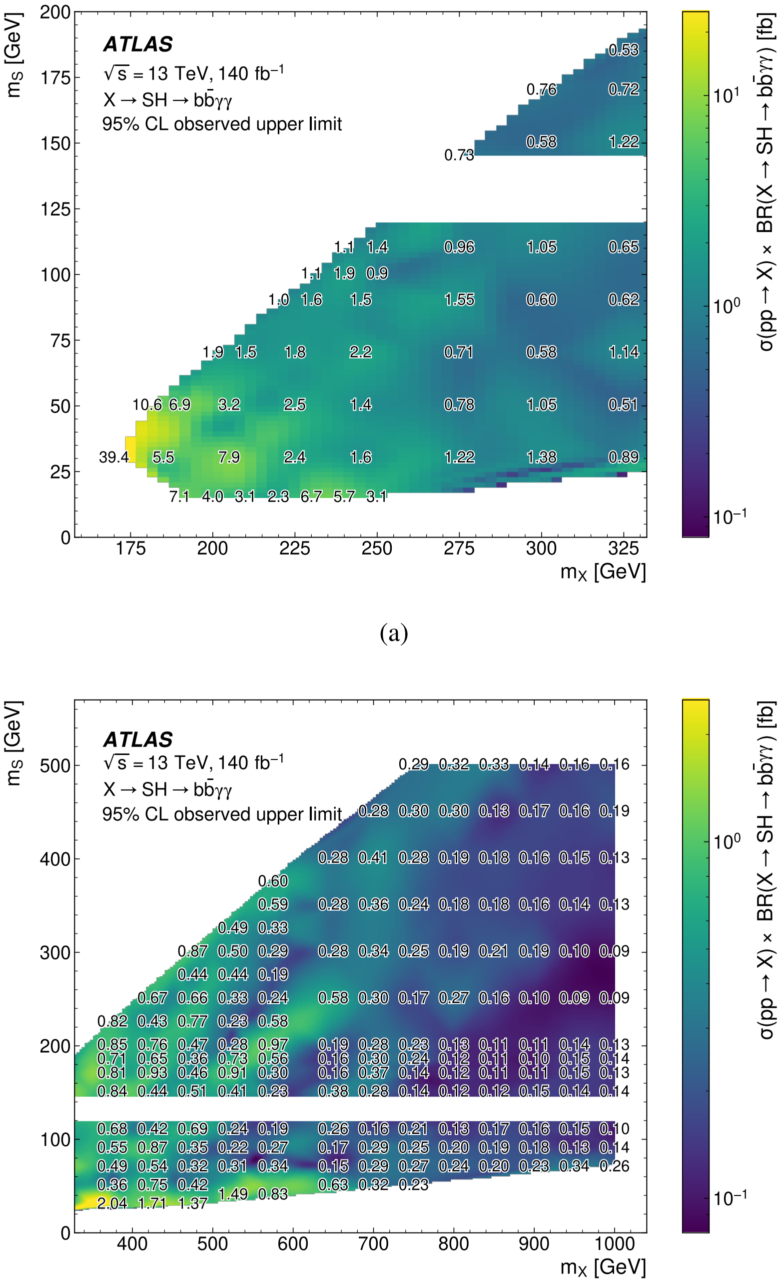

(a)

(b)

Figure 4.25: Observed 95% CL upper limits set on the $X \to SH \to b\bar{b}\gamma\gamma$ cross section in the (m_X, m_S) plane in the (a) low m_X and (b) high m_X regions

Conclusion

This thesis work falls within two pillars of modern particle physics : detector performance and searches for Beyond the Standard Model physics.
In the first place, the adaptation of a flavour tagging algorithm for the High-Luminosity LHC configuration is presented. Science breakthroughs are often triggered by better and more precise experimental techniques. For particle colliders, one the most critical parameter is the quantity of data collected since the processes of interest are extremely scarce. The HL-LHC major upgrade therefore aims to increase the accelerator luminosity and is built to achieve a total collected dataset 10 times larger than what is expected at the end of Run 3. However, the instantaneous luminosity increases comes at the cost of a harsher environment with more pile-up, tracks and radiations. The work presented here shows the training of DIPS, an impact parameter based flavour-tagging algorithm in the HL-LHC configuration.
Different configurations are tested to select the DIPS training with the best performance. The resulting model is further used in the high-level tagger DL1d which is also retrained for upgrade. Parallel studies show that the graph neural network based tagger GN1 is displaying better performance than DIPS and DL1d. Future work for flavour tagging at HL-LHC will therefore focus on optimisation studies of a similar graph neural network based algorithm with larger training statistics.
However there are a few messages to gain from the DIPS training presented in this work. Trainings done with the Loose tracks selection display better performance than the ones with the Tight tracks selection, confirming the result from Run 2. This is also the case with GN1, which shows that neural networks perform better when they are trained with a large pool of tracks and as less imposed cuts as possible. DIPS presents acceptable performance with respect to Run 2 despite the fact that this work's reach is preliminary and performed with lower statistics samples.

Looking for new physics can take many forms. In the second part of this thesis, a research for Beyond Standard Model scalar particles X and S in the $b\bar{b}\gamma\gamma$ final state is shown. These particles could be part of an extended Higgs sector and the research is model independent in order to be as broad as possible.
The analysis uses parametric neural networks (PNNs), an innovative method which provides a continuous sensitivity and allows to target a wide range of masses. The low mass region with $m_X < 250$ GeV and $m_S < 50$ GeV in particular is probed for this first time thanks to the $b\bar{b}\gamma\gamma$ final state low p_T threshold di-photon triggers. The observed results are compatible with the Standard Model, but a local excess with a 3.55σ significance is observed at (m_X, m_S) = (575, 200) GeV. The excess reduces to a

2.0σ global significance when the *look-elsewhere effect* is taken into account. Another important result is the study of the excess reported by the CMS experiment in the same decay channel at (m_X, m_S) = (650, 90) GeV, which is not confirmed by our analysis.
Systematic uncertainties in particular are studied and have their impact assessed. The largest one is associated to the modelling of the $\gamma\gamma +$ jets continuum background in the PNN. Experimental uncertainties related to flavour tagging and jet energy resolution are the ones with the largest influence on the results. The total effect of the uncertainties can lead to a 40% impact on the signal upper limit in some mass points.
This analysis will be completed in the future with Run 3 data at a slightly higher centre of mass energy. The statistics increase with Run 3 and eventually HL-LHC along with a reworked analysis strategy optimised for the latest Runs tools and performance will allow to set stricter constraints on the signal production cross section. The development carried out is also interesting for other analysis and especially the search for the $HH \to b\bar{b}\gamma\gamma$ process. Research for di-Higgs is a top priority for HL-LHC and the previous analysis strategy in the $b\bar{b}\gamma\gamma$ channel mostly relied on the invariant mass $m_{\gamma\gamma}$ fit. Studies with the PNN presented in this thesis show that alternative methods are possible.

Bibliography

[1] ATLAS Collaboration. Deep Sets based Neural Networks for Impact Parameter Flavour Tagging in ATLAS (2020). URL: http://cds.cern.ch/record/2718948 (cit. on pp. 10, 11, 93, 94, 98, 104, 107).

[2] ATLAS Collaboration. Expected tracking and related performance with the updated ATLAS Inner Tracker layout at the High-Luminosity LHC (2021). URL: https://cds.cern.ch/record/2776651 (cit. on pp. 12, 86–89, 93, 99, 100, 108).

[3] ATLAS Collaboration. Neural Network Jet Flavour Tagging with the Upgraded ATLAS Inner Tracker Detector at the High-Luminosity LHC (2022). URL: https://cds.cern.ch/record/2839913 (cit. on pp. 13, 99, 104, 108, 113).

[4] I. F. Ginzburg, M. Krawczyk, and P. Osland. "Two Higgs doublet models with CP violation". *International Workshop on Linear Colliders (LCWS 2002)*. Nov. 2002, pp. 703–706. arXiv: hep-ph/0211371 (cit. on pp. 14, 59).

[5] U. Ellwanger, C. Hugonie, and A. M. Teixeira. The Next-to-Minimal Supersymmetric Standard Model. *Phys. Rept.* 496 (2010), pp. 1–77. DOI: 10.1016/j.physrep.2010.07.001. arXiv: 0910.1785 [hep-ph] (cit. on pp. 14, 58).

[6] CMS Collaboration. Search for a new resonance decaying into two spin-0 bosons in a final state with two photons and two bottom quarks in proton-proton collisions at $\sqrt{s} = 13$ TeV. *JHEP* 05 (2024), p. 316. DOI: 10.1007/JHEP05(2024)316. arXiv: 2310.01643 [hep-ex] (cit. on pp. 14, 59, 62–64, 116, 145).

[7] CMS Collaboration. Search for a massive scalar resonance decaying to a light scalar and a Higgs boson in the four b quarks final state with boosted topology. *Phys. Lett. B* 842 (2023), p. 137392. DOI: 10.1016/j.physletb.2022.137392. arXiv: 2204.12413 [hep-ex] (cit. on pp. 14, 62, 64, 116).

[8] CMS Collaboration. Search for a heavy Higgs boson decaying into two lighter Higgs bosons in the $\tau\tau$bb final state at 13 TeV. *JHEP* 11 (2021), p. 057. DOI: 10.1007/JHEP11(2021)057. arXiv: 2106.10361 [hep-ex] (cit. on pp. 14, 62, 64, 116).

[9] ATLAS Collaboration. Search for a resonance decaying into a scalar particle and a Higgs boson in the final state with two bottom quarks and two photons in proton-proton collisions at a center of mass energy of 13 TeV with the ATLAS detector (Apr. 2024). arXiv: 2404.12915 [hep-ex] (cit. on pp. 17, 60, 115, 116, 121, 122, 128, 138, 139).

[10] D.Griffiths. *Introduction to Elementary Pagerticles*. John Wiley & Sons, 1987 (cit. on p. 33).

[11] M. Gell-Mann. The Eightfold Way: A Theory of strong interaction symmetry (1961). DOI: `10.2172/4008239` (cit. on p. 33).

[12] M. Gell-Mann. A Schematic Model of Baryons and Mesons. *Phys. Lett.* 8 (1964), pp. 214–215. DOI: `10.1016/S0031-9163(64)92001-3` (cit. on p. 33).

[13] G. Zweig. An SU(3) model for strong interaction symmetry and its breaking. Version 1-2 (1964). URL: `https://cds.cern.ch/record/352337/files/CERN-TH-401.pdf` (cit. on p. 33).

[14] S.L. Glashow. Partial Symmetries of Weak Interactions. *Nucl. Phys.* 22 (1961), pp. 579–588. DOI: `10.1016/0029-5582(61)90469-2` (cit. on pp. 34, 40).

[15] S. Weinberg. A Model of Leptons. *Phys. Rev. Lett.* 19 (1967), pp. 1264–1266. DOI: `10.1103/PhysRevLett.19.1264` (cit. on pp. 34, 40).

[16] A. Salam and J.C. Ward. Electromagnetic and weak interactions. *Phys. Lett.* 13 (1964), pp. 168–171. DOI: `10.1016/0031-9163(64)90711-5` (cit. on pp. 34, 40).

[17] T. Lancaster and S. Blundell. *Quantum Field Theory for the Gifted Amateur*. Oxford University Press, 2014 (cit. on p. 34).

[18] Wikipedia. *Standard Model*. URL: `https://en.wikipedia.org/wiki/File:Standard_Model_of_Elementary_Particles.svg` (cit. on p. 35).

[19] M. Thomson. *Modern Particle Physics*. University Printing House, Cambridge, 2013 (cit. on p. 39).

[20] P. Higgs. Broken Symmetries and the Masses of Gauge Bosons. *Phys. Rev. Lett.* 13 (1964). Ed. by J. C. Taylor, pp. 508–509. DOI: `10.1103/PhysRevLett.13.508` (cit. on p. 42).

[21] F. Englert and R. Brout. Broken Symmetry and the Mass of Gauge Vector Mesons. *Phys. Rev. Lett.* 13 (1964). Ed. by J. C. Taylor, pp. 321–323. DOI: `10.1103/PhysRevLett.13.321` (cit. on p. 42).

[22] S. Weinberg. From BCS to the LHC : Steven Weinberg reflects on spontaneous symmetry breaking. *CERN Courrier* (2008). URL: `https://cerncourier.com/a/from-bcs-to-the-lhc/` (cit. on p. 43).

[23] ATLAS Collaboration. Observation of a new particle in the search for the Standard Model Higgs boson with the ATLAS detector at the LHC. *Phys. Lett. B* 716 (2012), pp. 1–29. DOI: `10.1016/j.physletb.2012.08.020`. arXiv: `1207.7214 [hep-ex]` (cit. on pp. 44, 48).

[24] CMS Collaboration. Observation of a New Boson at a Mass of 125 GeV with the CMS Experiment at the LHC. *Phys. Lett. B* 716 (2012), pp. 30–61. DOI: `10.1016/j.physletb.2012.08.021`. arXiv: `1207.7235 [hep-ex]` (cit. on pp. 44, 48).

[25] CMS collaboration. A portrait of the Higgs boson by the CMS experiment ten years after the discovery. *Nature* 607.7917 (2022). [Erratum: Nature 623, (2023)], pp. 60–68. DOI: `10.1038/s41586-022-04892-x`. arXiv: `2207.00043 [hep-ex]` (cit. on pp. 45, 49, 54).

[26] ATLAS Collaboration. Characterising the Higgs boson with ATLAS data from Run 2 of the LHC (Apr. 2024). arXiv: `2404.05498 [hep-ex]` (cit. on p. 45).

[27] R. L. Workman et al. Review of Particle Physics. *PTEP* 2022 (2022), p. 083C01. DOI: `10.1093/ptep/ptac097` (cit. on p. 45).

[28] ATLAS Collaboration. Evidence of off-shell Higgs boson production from ZZ leptonic decay channels and constraints on its total width with the ATLAS detector. *Phys. Lett. B* 846 (2023), p. 138223. DOI: `10.1016/j.physletb.2023.138223`. arXiv: `2304.01532 [hep-ex]` (cit. on p. 45).

[29] CMS Collaboration. Measurement of the Higgs boson width and evidence of its off-shell contributions to ZZ production. *Nature Phys.* 18.11 (2022), pp. 1329–1334. DOI: `10.1038/s41567-022-01682-0`. arXiv: `2202.06923 [hep-ex]` (cit. on p. 45).

[30] CMS Collaboration. Constraints on the spin-parity and anomalous HVV couplings of the Higgs boson in proton collisions at 7 and 8 TeV. *Phys. Rev. D* 92.1 (2015), p. 012004. DOI: `10.1103/PhysRevD.92.012004`. arXiv: `1411.3441 [hep-ex]` (cit. on p. 45).

[31] ATLAS Collaboration. Study of the spin and parity of the Higgs boson in diboson decays with the ATLAS detector. *Eur. Phys. J. C* 75.10 (2015). [Erratum: Eur.Phys.J.C 76, 152 (2016)], p. 476. DOI: `10.1140/epjc/s10052-015-3685-1`. arXiv: `1506.05669 [hep-ex]` (cit. on p. 45).

[32] M. Carena, C. Grojean, M. Kado, et al. Status of Higgs boson physics, in Review of Particle Physics. *Chin. Phys.* C40 (2016), p. 100001. URL: `http://pdg.lbl.gov/2016/reviews/rpp2016-rev-higgs-boson.pdf.` (cit. on p. 45).

[33] D. de Florian et al. Handbook of LHC Higgs Cross Sections: 4. Deciphering the Nature of the Higgs Sector. 2/2017 (Oct. 2016). DOI: `10.23731/CYRM-2017-002`. arXiv: `1610.07922 [hep-ph]` (cit. on pp. 45, 47, 58).

[34] ATLAS Collaboration. Combined Measurement of the Higgs Boson Mass from the $H \to \gamma\gamma$ and $H \to ZZ^* \to 4\ell$ Decay Channels with the ATLAS Detector Using $\sqrt{s} = 7$, 8, and 13 TeV pp Collision Data. *Phys. Rev. Lett.* 131.25 (2023), p. 251802. DOI: `10.1103/PhysRevLett.131.251802`. arXiv: `2308.04775 [hep-ex]` (cit. on p. 48).

[35] ATLAS Collaboration. Observation of $H \to b\bar{b}$ decays and VH production with the ATLAS detector. *Phys. Lett. B* 786 (2018), pp. 59–86. DOI: `10.1016/j.physletb.2018.09.013`. arXiv: `1808.08238 [hep-ex]` (cit. on p. 49).

[36] CMS Collaboration. Observation of Higgs Boson Decay to Bottom Quarks. *Phys. Rev. Lett.* 121 (12 2018), p. 121801. URL: `https://link.aps.org/doi/10.1103/PhysRevLett.121.121801` (cit. on p. 49).

[37] ATLAS Collaboration. Observation and measurement of Higgs boson decays to WW^* with the ATLAS detector. *Phys. Rev. D* 92.1 (2015), p. 012006. DOI: `10.1103/PhysRevD.92.012006`. arXiv: `1412.2641 [hep-ex]` (cit. on p. 49).

[38] ATLAS Collaboration. Cross-section measurements of the Higgs boson decaying into a pair of τ-leptons in proton-proton collisions at $\sqrt{s} = 13$ TeV with the ATLAS detector. *Phys. Rev. D* 99 (2019), p. 072001. DOI: `10.1103/PhysRevD.99.072001`. arXiv: `1811.08856 [hep-ex]` (cit. on p. 49).

[39] CMS Collaboration. Observation of the Higgs boson decay to a pair of τ leptons with the CMS detector. *Phys. Lett. B* 779 (2018), pp. 283–316. DOI: `10.1016/j.physletb.2018.02.004`. arXiv: `1708.00373 [hep-ex]` (cit. on p. 49).

[40] ATLAS Collaboration. A detailed map of Higgs boson interactions by the ATLAS experiment ten years after the discovery. *Nature* 607.7917 (2022). [Erratum: Nature 612, E24 (2022)], pp. 52–59. DOI: `10.1038/s41586-022-04893-w`. arXiv: `2207.00092 [hep-ex]` (cit. on p. 50).

[41] J. R. Andersen et al. Handbook of LHC Higgs Cross Sections: 3. Higgs Properties (July 2013). Ed. by S Heinemeyer, C Mariotti, G Passarino, et al. DOI: `10.5170/CERN-2013-004`. arXiv: `1307.1347 [hep-ph]` (cit. on p. 50).

[42] Studies of new Higgs boson interactions through nonresonant HH production in the $b\bar{b}\gamma\gamma$ final state in pp collisions at $\sqrt{s} = 13$ TeV with the ATLAS detector. *JHEP* 01 (2024), p. 066. DOI: `10.1007/JHEP01(2024)066`. arXiv: `2310.12301 [hep-ex]` (cit. on pp. 51–53, 115).

[43] J. Baglio, F. Campanario, S. Glaus, et al. $gg \to HH$: Combined uncertainties. *Phys. Rev. D* 103.5 (2021), p. 056002. DOI: `10.1103/PhysRevD.103.056002`. arXiv: `2008.11626 [hep-ph]` (cit. on p. 51).

[44] J. Veatch. Searches for Resonant Scalar Boson Pair Production Using Run 2 LHC Proton-Proton Collision Data. *Symmetry* 14.2 (2022), p. 260. DOI: `10.3390/sym14020260` (cit. on p. 53).

[45] ATLAS Collaboration. Search for nonresonant pair production of Higgs bosons in the $b\bar{b}b\bar{b}$ final state in pp collisions at $\sqrt{s} = 13$ TeV with the ATLAS detector. *Phys. Rev. D* 108.5 (2023), p. 052003. DOI: `10.1103/PhysRevD.108.052003`. arXiv: `2301.03212 [hep-ex]` (cit. on p. 53).

[46] ATLAS Collaboration. Search for resonant and non-resonant Higgs boson pair production in the $b\bar{b}\tau^+\tau^-$ decay channel using 13 TeV pp collision data from the ATLAS detector. *JHEP* 07 (2023), p. 040. DOI: `10.1007/JHEP07(2023)040`. arXiv: `2209.10910 [hep-ex]` (cit. on p. 53).

[47] ATLAS Collaboration. Search for Higgs boson pair production in the $WW^{(*)}WW^{(*)}$ decay channel using ATLAS data recorded at $\sqrt{s} = 13$ TeV. *JHEP* 05 (2019), p. 124. DOI: `10.1007/JHEP05(2019)124`. arXiv: `1811.11028 [hep-ex]` (cit. on p. 53).

[48] ATLAS Collaboration. Search for Higgs boson pair production in the $b\bar{b}WW^*$ decay mode at $\sqrt{s} = 13$ TeV with the ATLAS detector. *JHEP* 04 (2019), p. 092. DOI: `10.1007/JHEP04(2019)092`. arXiv: `1811.04671 [hep-ex]` (cit. on p. 53).

[49] ATLAS Collaboration. Search for Higgs boson pair production in the $\gamma\gamma WW^*$ channel using pp collision data recorded at $\sqrt{s} = 13$ TeV with the ATLAS detector. *Eur. Phys. J. C* 78.12 (2018), p. 1007. DOI: `10.1140/epjc/s10052-018-6457-x`. arXiv: `1807.08567 [hep-ex]` (cit. on p. 53).

[50] ATLAS Collaboration. Search for non-resonant Higgs boson pair production in final states with leptons, taus, and photons in pp collisions at $\sqrt{s} = 13$ TeV with the ATLAS detector (May 2024). arXiv: `2405.20040 [hep-ex]` (cit. on p. 53).

[51] ATLAS Collaboration. Search for non-resonant Higgs boson pair production in the $2b + 2\ell + E_{\mathrm{T}}^{\mathrm{miss}}$ final state in pp collisions at $\sqrt{s} = 13$ TeV with the ATLAS detector. *JHEP* 02 (2024), p. 037. DOI: `10.1007/JHEP02(2024)037`. arXiv: `2310.11286 [hep-ex]` (cit. on p. 53).

[52] ATLAS Collaboration. Constraints on the Higgs boson self-coupling from single- and double-Higgs production with the ATLAS detector using pp collisions at $\sqrt{s} = 13$ TeV. *Phys. Lett. B* 843 (2023), p. 137745. DOI: `10.1016/j.physletb.2023.137745`. arXiv: `2211.01216 [hep-ex]` (cit. on pp. 53–55).

[53] ATLAS Collaboration. Combination of searches for Higgs boson pair production in pp Collisions at $\sqrt{s} = 13$ TeV with the ATLAS Detector. *Phys. Rev. Lett.* 133.10 (2024), p. 101801. DOI: `10.1103/PhysRevLett.133.101801`. arXiv: `2406.09971 [hep-ex]` (cit. on pp. 53, 54).

[54] Y. Fukuda et al. Evidence for oscillation of atmospheric neutrinos. *Phys. Rev. Lett.* 81 (1998), pp. 1562–1567. DOI: `10.1103/PhysRevLett.81.1562`. arXiv: `hep-ex/9807003` (cit. on p. 55).

[55] J.H. Oort. The force exerted by the stellar system in the direction perpendicular to the galactic plane and some related problems. *Bull. Astron. Inst. Netherlands* 6 (1932), pp. 249–287. URL: `https://cds.cern.ch/record/436532` (cit. on p. 56).

[56] V. C. Rubin. Dark Matter in Spiral Galaxies. *Scientific American* 248.6 (1983), pp. 96–109. URL: `http://www.jstor.org/stable/24968923` (cit. on p. 56).

[57] A. D. Sakharov. Violation of CP Invariance, C asymmetry, and baryon asymmetry of the universe. *Pisma Zh. Eksp. Teor. Fiz.* 5 (1967), pp. 32–35. DOI: `10.1070/PU1991v034n05ABEH002497` (cit. on p. 56).

[58] B. Abi et al. Measurement of the Positive Muon Anomalous Magnetic Moment to 0.46 ppm. *Phys. Rev. Lett.* 126.14 (2021), p. 141801. DOI: `10.1103/PhysRevLett.126.141801`. arXiv: `2104.03281 [hep-ex]` (cit. on p. 56).

[59] T. Aoyama et al. The anomalous magnetic moment of the muon in the Standard Model. *Phys. Rept.* 887 (2020), pp. 1–166. DOI: `10.1016/j.physrep.2020.07.006`. arXiv: `2006.04822 [hep-ph]` (cit. on p. 56).

[60] Sz. Borsanyi et al. Leading hadronic contribution to the muon magnetic moment from lattice QCD. *Nature* 593.7857 (2021), pp. 51–55. DOI: `10.1038/s41586-021-03418-1`. arXiv: `2002.12347 [hep-lat]` (cit. on p. 56).

[61] T. Aaltonen et al. High-precision measurement of the W boson mass with the CDF II detector. *Science* 376.6589 (2022), pp. 170–176. DOI: `10.1126/science.abk1781` (cit. on p. 57).

[62] ATLAS Collaboration. Measurement of the W-boson mass and width with the ATLAS detector using proton-proton collisions at $\sqrt{s} = 7$ TeV (Mar. 2024). arXiv: `2403.15085 [hep-ex]` (cit. on p. 57).

[63] CMS Collaboration. Measurement of the W boson mass in proton-proton collisions at $\sqrt{s} = 13$ TeV (2024). URL: `https://cds.cern.ch/record/2910372` (cit. on p. 57).

[64] Y. S. Amhis et al. Averages of b-hadron, c-hadron, and τ-lepton properties as of 2021. *Phys. Rev. D* 107.5 (2023), p. 052008. DOI: `10.1103/PhysRevD.107.052008`. arXiv: `2206.07501 [hep-ex]` (cit. on p. 57).

[65] C. Csaki. The Minimal supersymmetric standard model (MSSM). *Mod. Phys. Lett. A* 11 (1996), p. 599. DOI: `10.1142/S021773239600062X`. arXiv: `hep-ph/9606414` (cit. on p. 58).

[66] E. Bagnaschi et al. MSSM Higgs Boson Searches at the LHC: Benchmark Scenarios for Run 2 and Beyond. *Eur. Phys. J. C* 79.7 (2019), p. 617. DOI: `10.1140/epjc/s10052-019-7114-8`. arXiv: `1808.07542 [hep-ph]` (cit. on p. 58).

[67] A. de Gouvea, A. Friedland, and H. Murayama. Next-to-minimal supersymmetric standard model with the gauge mediation of supersymmetry breaking. *Phys. Rev. D* 57 (1998), pp. 5676–5696. DOI: `10.1103/PhysRevD.57.5676`. arXiv: `hep-ph/9711264` (cit. on p. 58).

[68] G. C. Branco, P. M. Ferreira, L. Lavoura, et al. Theory and phenomenology of two-Higgs-doublet models. *Phys. Rept.* 516 (2012), pp. 1–102. DOI: `10.1016/j.physrep.2012.02.002`. arXiv: `1106.0034 [hep-ph]` (cit. on p. 59).

[69] M. Mühlleitner, M. O. P. Sampaio, R. Santos, et al. The N2HDM under Theoretical and Experimental Scrutiny. *JHEP* 03 (2017), p. 094. DOI: `10.1007/JHEP03(2017)094`. arXiv: `1612.01309 [hep-ph]` (cit. on p. 59).

[70] S. Baum and N. R. Shah. Two Higgs Doublets and a Complex Singlet: Disentangling the Decay Topologies and Associated Phenomenology. *JHEP* 12 (2018), p. 044. DOI: `10.1007/JHEP12(2018)044`. arXiv: `1808.02667 [hep-ph]` (cit. on p. 59).

[71] T. Robens, T. Stefaniak, and J. Wittbrodt. Two-real-scalar-singlet extension of the SM: LHC phenomenology and benchmark scenarios. *Eur. Phys. J. C* 80.2 (2020), p. 151. DOI: `10.1140/epjc/s10052-020-7655-x`. arXiv: `1908.08554 [hep-ph]` (cit. on p. 59).

[72] L. Randall and R. Sundrum. A Large mass hierarchy from a small extra dimension. *Phys. Rev. Lett.* 83 (1999), pp. 3370–3373. DOI: `10.1103/PhysRevLett.83.3370`. arXiv: `hep-ph/9905221` (cit. on p. 59).

[73] ATLAS Collaboration. HEFT interpretations of Higgs boson pair searches in $b\bar{b}\gamma\gamma$ and $b\bar{b}\tau\tau$ final states and of their combination in ATLAS (2022). URL: `https://cds.cern.ch/record/2806411/` (cit. on p. 59).

[74] ATLAS Collaboration. Search for Higgs boson pair production in the two bottom quarks plus two photons final state in pp collisions at $\sqrt{s} = 13$ TeV with the ATLAS detector. *Phys. Rev. D* 106.5 (2022), p. 052001. DOI: `10.1103/PhysRevD.106.052001`. arXiv: `2112.11876 [hep-ex]` (cit. on pp. 60, 115, 119, 125, 129, 143).

[75] ATLAS Collaboration. Combination of Searches for Resonant Higgs Boson Pair Production Using pp collisions at $\sqrt{s} = 13$ TeV with the ATLAS Detector. *Phys. Rev. Lett.* 132.23 (2024), p. 231801. DOI: `10.1103/PhysRevLett.132.231801`. arXiv: `2311.15956 [hep-ex]` (cit. on pp. 60, 61).

[76] CMS Collaboration. Searches for Higgs Boson Production through Decays of Heavy Resonances (Mar. 2024). arXiv: `2403.16926 [hep-ex]` (cit. on pp. 61, 64).

[77] S. Dittmaier et al. Handbook of LHC Higgs Cross Sections: 2. Differential Distributions (Jan. 2012). DOI: `10.5170/CERN-2012-002`. arXiv: `1201.3084 [hep-ph]` (cit. on p. 62).

[78] ATLAS Collaboration. Search for a new heavy scalar particle decaying into a Higgs boson and a new scalar singlet in final states with one or two light leptons and a pair of τ-leptons with the ATLAS detector. *JHEP* 10 (2023), p. 009. DOI: `10.1007/JHEP10(2023)009`. arXiv: `2307.11120 [hep-ex]` (cit. on pp. 62, 116).

[79] U. Ellwanger and C. Hugonie. Benchmark planes for Higgs-to-Higgs decays in the NMSSM. *Eur. Phys. J. C* 82.5 (2022), p. 406. DOI: `10.1140/epjc/s10052-022-10364-3`. arXiv: `2203.05049 [hep-ph]` (cit. on pp. 62, 64).

[80] *LHC Higgs Working Group Beyond the Standard Model Higgs – NMSSM*. URL: `https://twiki.cern.ch/twiki/bin/view/LHCPhysics/LHCHWGNMSSM` (cit. on p. 62).

[81] LHC Machine. *JINST* 3 (2008). Ed. by L. Evans and P. Bryant, S08001. DOI: `10.1088/1748-0221/3/08/S08001` (cit. on pp. 66, 67).

[82] *The HL-LHC project*. URL: `https://hilumilhc.web.cern.ch/content/hl-lhc-project` (cit. on p. 67).

[83] CERN Courrier. The tale of a billion-trillion protons. URL: `https://cerncourier.com/a/the-tale-of-a-billion-trillion-protons/` (cit. on p. 67).

[84] E. Lopienska. The CERN accelerator complex, layout in 2022. Complexe des accelerateurs du CERN en janvier 2022. URL: `https://cds.cern.ch/record/2800984` (cit. on p. 68).

[85] *Public ATLAS Luminosity Results for Run-3 of the LHC*. URL: `https://twiki.cern.ch/twiki/bin/view/AtlasPublic/LuminosityPublicResultsRun3` (cit. on p. 70).

[86] ATLAS Collaboration. The ATLAS Experiment at the CERN Large Hadron Collider. *JINST* 3 (2008), S08003. DOI: `10.1088/1748-0221/3/08/S08003` (cit. on pp. 71–73, 75, 76).

[87] ATLAS Collaboration. *ATLAS inner detector: Technical Design Report, 1*. Technical design report. ATLAS. Geneva: CERN, 1997. URL: `https://cds.cern.ch/record/331063` (cit. on p. 71).

[88] ATLAS Collaboration. *ATLAS inner detector: Technical Design Report, 2*. Technical design report. ATLAS. Geneva: CERN, 1997. URL: `https://cds.cern.ch/record/331064` (cit. on p. 71).

[89] ATLAS Collaboration. Alignment of the ATLAS Inner Detector in Run-2. *Eur. Phys. J. C* 80.12 (2020), p. 1194. DOI: `10.1140/epjc/s10052-020-08700-6`. arXiv: `2007.07624 [hep-ex]` (cit. on p. 72).

[90] ATLAS Collaboration. *ATLAS pixel detector: Technical Design Report*. Technical design report. ATLAS. Geneva: CERN, 1998. URL: `https://cds.cern.ch/record/381263` (cit. on p. 72).

[91] ATLAS Collaboration. *ATLAS Insertable B-Layer Technical Design Report*. Tech. rep. 2010. URL: `https://cds.cern.ch/record/1291633` (cit. on p. 73).

[92] ATLAS Collaboration. Performance of the ATLAS Transition Radiation Tracker in Run 1 of the LHC: tracker properties. *JINST* 12.05 (2017), P05002. DOI: `10.1088/1748-0221/12/05/P05002`. arXiv: `1702.06473 [hep-ex]` (cit. on p. 73).

[93] ATLAS Collaboration. The ATLAS experiment at the CERN Large Hadron Collider: a description of the detector configuration for Run 3. *JINST* 19.05 (2024), P05063. DOI: `10.1088/1748-0221/19/05/P05063`. arXiv: `2305.16623 [physics.ins-det]` (cit. on p. 74).

[94] ATLAS Collaboration. *ATLAS liquid-argon calorimeter: Technical Design Report*. Technical design report. ATLAS. CERN, 1996. URL: https://cds.cern.ch/record/331061 (cit. on p. 74).

[95] ATLAS Collaboration. *ATLAS tile calorimeter: Technical Design Report*. CERN, 1996. URL: https://cds.cern.ch/record/331062 (cit. on p. 75).

[96] ATLAS Collaboration. *ATLAS muon spectrometer: Technical Design Report*. Geneva: CERN, 1997. URL: https://cds.cern.ch/record/331068 (cit. on p. 75).

[97] ATLAS Collaboration. *ATLAS magnet system: Technical Design Report, 1*. Technical design report. ATLAS. Geneva: CERN, 1997. DOI: 10.17181/CERN.905C.VDTM. URL: https://cds.cern.ch/record/338080 (cit. on p. 76).

[98] A. Yamamoto et al. The ATLAS central solenoid. *Nucl. Instrum. Meth. A* 584 (2008), pp. 53–74. DOI: 10.1016/j.nima.2007.09.047 (cit. on p. 76).

[99] Measurement Of Magnetic Field With The Giant Atlas Solenoid. URL: https://www.golabz.eu/ils/measurement-of-magnetic-field-with-the-giant-atlas-solenoid (cit. on p. 76).

[100] ATLAS Collaboration. *ATLAS level-1 trigger: Technical Design Report*. Technical design report. ATLAS. Geneva: CERN, 1998. URL: https://cds.cern.ch/record/381429 (cit. on p. 76).

[101] ATLAS Collaboration. *ATLAS high-level trigger, data-acquisition and controls: Technical Design Report*. Technical design report. ATLAS. Geneva: CERN, 2003. URL: https://cds.cern.ch/record/616089 (cit. on p. 76).

[102] ATLAS collaboration. Operation of the ATLAS trigger system in Run 2. *JINST* 15.10 (2020), P10004. DOI: 10.1088/1748-0221/15/10/P10004. arXiv: 2007.12539 [physics.ins-det] (cit. on p. 77).

[103] T. Cornelissen, M. Elsing, S. Fleischmann, et al. *Concepts, Design and Implementation of the ATLAS New Tracking (NEWT)*. Tech. rep. Geneva: CERN, 2007. URL: https://cds.cern.ch/record/1020106 (cit. on pp. 77, 87).

[104] ATLAS Collaboration. Performance of the ATLAS Track Reconstruction Algorithms in Dense Environments in LHC Run 2. *Eur. Phys. J. C* 77.10 (2017), p. 673. DOI: 10.1140/epjc/s10052-017-5225-7. arXiv: 1704.07983 [hep-ex] (cit. on p. 77).

[105] R. Fruhwirth. Application of Kalman filtering to track and vertex fitting. *Nucl. Instrum. Meth. A* 262 (1987), pp. 444–450. DOI: 10.1016/0168-9002(87)90887-4 (cit. on p. 77).

[106] ATLAS Collaboration. A neural network clustering algorithm for the ATLAS silicon pixel detector. *JINST* 9 (2014), P09009. DOI: 10.1088/1748-0221/9/09/P09009. arXiv: 1406.7690 [hep-ex] (cit. on p. 77).

[107] ATLAS Collaboration. Reconstruction of primary vertices at the ATLAS experiment in Run 1 proton–proton collisions at the LHC. *Eur. Phys. J. C* 77.5 (2017). DOI: 10.1140/epjc/s10052-017-4887-5. arXiv: 1611.10235 [physics.ins-det] (cit. on p. 77).

[108] ATLAS Collaboration. Measurement of Higgs boson production in the diphoton decay channel in *pp* collisions at center-of-mass energies of 7 and 8 TeV with the ATLAS detector. *Phys. Rev. D* 90.11 (2014), p. 112015. DOI: 10.1103/PhysRevD.90.112015. arXiv: 1408.7084 [hep-ex] (cit. on p. 78).

[109] ATLAS Collaboration. Electron and photon performance measurements with the ATLAS detector using the 2015–2017 LHC proton-proton collision data. *JINST* 14.12 (2019), P12006. DOI: 10.1088/1748-0221/14/12/P12006. arXiv: 1908.00005 [hep-ex] (cit. on pp. 78, 79).

[110] ATLAS Collaboration. Electron and photon efficiencies in LHC Run 2 with the ATLAS experiment (Aug. 2023). arXiv: 2308.13362 [hep-ex] (cit. on pp. 78, 80, 132).

[111] ATLAS Collaboration. Electron and photon energy calibration with the ATLAS detector using LHC Run 2 data. *JINST* 19.02 (2024), P02009. DOI: 10.1088/1748-0221/19/02/P02009. arXiv: 2309.05471 [hep-ex] (cit. on p. 78).

[112] M. Cacciari, G. P. Salam, and G. Soyez. The anti-k_t jet clustering algorithm. *JHEP* 04 (2008), p. 063. DOI: 10.1088/1126-6708/2008/04/063. arXiv: 0802.1189 [hep-ph] (cit. on pp. 80, 101).

[113] ATLAS Collaboaration. Jet reconstruction and performance using particle flow with the ATLAS Detector. *Eur. Phys. J. C* 77.7 (2017), p. 466. DOI: 10.1140/epjc/s10052-017-5031-2. arXiv: 1703.10485 [hep-ex] (cit. on p. 80).

[114] ATLAS Collaboration. Performance of pile-up mitigation techniques for jets in *pp* collisions at $\sqrt{s} = 8$ TeV using the ATLAS detector. *Eur. Phys. J. C* 76.11 (2016), p. 581. DOI: 10.1140/epjc/s10052-016-4395-z. arXiv: 1510.03823 [hep-ex] (cit. on p. 80).

[115] ATLAS Collaboration. Jet energy scale and resolution measured in proton–proton collisions at $\sqrt{s} = 13$ TeV with the ATLAS detector. *Eur. Phys. J. C* 81.8 (2021), p. 689. DOI: 10.1140/epjc/s10052-021-09402-3. arXiv: 2007.02645 [hep-ex] (cit. on pp. 80, 81, 132).

[116] ATLAS Collaboration. Muon reconstruction and identification efficiency in ATLAS using the full Run 2 *pp* collision data set at $\sqrt{s} = 13$ TeV. *Eur. Phys. J. C* 81.7 (2021), p. 578. DOI: 10.1140/epjc/s10052-021-09233-2. arXiv: 2012.00578 [hep-ex] (cit. on p. 81).

[117] ATLAS Collaboration. Identification and energy calibration of hadronically decaying tau leptons with the ATLAS experiment in *pp* collisions at $\sqrt{s}$=8 TeV. *Eur. Phys. J. C* 75.7 (2015), p. 303. DOI: 10.1140/epjc/s10052-015-3500-z. arXiv: 1412.7086 [hep-ex] (cit. on p. 82).

[118] ATLAS Collaboration. Reconstruction, Energy Calibration, and Identification of Hadronically Decaying Tau Leptons in the ATLAS Experiment for Run-2 of the LHC (2015). URL: `https://cds.cern.ch/record/2064383` (cit. on p. 82).

[119] ATLAS Collaboration. The performance of missing transverse momentum reconstruction and its significance with the ATLAS detector using 140 fb^{-1} of $\sqrt{s} = 13$ TeV pp collisions (Feb. 2024). arXiv: `2402.05858 [hep-ex]` (cit. on p. 82).

[120] Sherpa team. *About : Monte Carlo Event Generators*. URL: `https://sherpa-team.gitlab.io/monte-carlo.html` (cit. on p. 84).

[121] S. Agostinelli et al. GEANT4 - a simulation toolkit. *Nucl. Instrum. Meth. A* 506 (2003), pp. 250–303. DOI: `10.1016/S0168-9002(03)01368-8` (cit. on p. 83).

[122] ATLAS Collaboration. The ATLAS Simulation Infrastructure. *Eur. Phys. J. C* 70 (2010), pp. 823–874. DOI: `10.1140/epjc/s10052-010-1429-9`. arXiv: `1005.4568 [physics.ins-det]` (cit. on p. 83).

[123] W. Lukas. *Fast Simulation for ATLAS: Atlfast-II and ISF*. Tech. rep. Geneva: CERN, 2012. DOI: `10.1088/1742-6596/396/2/022031`. URL: `https://cds.cern.ch/record/1458503` (cit. on p. 83).

[124] G. Apollinari, I. Béjar Alonso, O. Brüning, et al. *High-Luminosity Large Hadron Collider (HL-LHC): Technical Design Report V. 0.1*. CERN Yellow Reports: Monographs. Geneva: CERN, 2017. DOI: `10.23731/CYRM-2017-004`. URL: `http://cds.cern.ch/record/2284929` (cit. on p. 83).

[125] ATLAS and CMS Collaborations. *Snowmass White Paper Contribution: Physics with the Phase-2 ATLAS and CMS Detectors*. Tech. rep. Geneva: CERN, 2022. URL: `https://cds.cern.ch/record/2805993` (cit. on p. 84).

[126] ATLAS Collaboration. *Technical Design Report for the Phase-II Upgrade of the ATLAS Trigger and Data Acquisition System - Event Filter Tracking Amendment*. Tech. rep. Geneva: CERN, 2022. DOI: `10.17181/CERN.ZK85.5TDL`. URL: `https://cds.cern.ch/record/2802799` (cit. on p. 84).

[127] ATLAS Collaboration. *ATLAS Liquid Argon Calorimeter Phase-II Upgrade: Technical Design Report*. Tech. rep. Geneva: CERN, 2017. DOI: `10.17181/CERN.6QIO.YGHO`. URL: `https://cds.cern.ch/record/2285582` (cit. on p. 85).

[128] ATLAS Collaboration. *Technical Design Report for the Phase-II Upgrade of the ATLAS Tile Calorimeter*. Tech. rep. Geneva: CERN, 2017. URL: `https://cds.cern.ch/record/2285583` (cit. on p. 85).

[129] T. Kawamoto, S. Vlachos, L. Pontecorvo, et al. *New Small Wheel Technical Design Report*. Tech. rep. 2013. URL: `https://cds.cern.ch/record/1552862` (cit. on p. 85).

[130] ATLAS Collaboration. *Technical Design Report: A High-Granularity Timing Detector for the ATLAS Phase-II Upgrade*. Tech. rep. Geneva: CERN, 2020. URL: https://cds.cern.ch/record/2719855 (cit. on p. 85).

[131] ATLAS Collaboration. *Technical Design Report for the ATLAS Inner Tracker Pixel Detector*. Tech. rep. Geneva: CERN, 2017. DOI: 10.17181/CERN.FOZZ.ZP3Q. URL: https://cds.cern.ch/record/2285585 (cit. on p. 85).

[132] ATLAS Collaboration. *Technical Design Report for the ATLAS Inner Tracker Strip Detector*. Tech. rep. Geneva: CERN, 2017. URL: https://cds.cern.ch/record/2257755 (cit. on p. 85).

[133] ATLAS Collaboration. Graph Neural Network Jet Flavour Tagging with the ATLAS Detector (2022). URL: http://cds.cern.ch/record/2811135 (cit. on pp. 92, 96, 100).

[134] ATLAS collaboration. Performance of b-Jet Identification in the ATLAS Experiment. *JINST* 11.04 (2016), P04008. DOI: 10.1088/1748-0221/11/04/P04008. arXiv: 1512.01094 [hep-ex] (cit. on p. 92).

[135] ATLAS Collaboration. Identification of Jets Containing b-Hadrons with Recurrent Neural Networks at the ATLAS Experiment (2017). URL: http://cds.cern.ch/record/2255226 (cit. on p. 93).

[136] ATLAS Collaboration. Secondary vertex finding for jet flavour identification with the ATLAS detector (2017). URL: http://cds.cern.ch/record/2270366 (cit. on p. 94).

[137] ATLAS Collaboration. Topological b-hadron decay reconstruction and identification of b-jets with the JetFitter package in the ATLAS experiment at the LHC (2018). URL: http://cds.cern.ch/record/2645405 (cit. on p. 94).

[138] ATLAS Collaboration. ATLAS b-jet identification performance and efficiency measurement with $t\bar{t}$ events in pp collisions at $\sqrt{s} = 13$ TeV. *Eur. Phys. J. C* 79.11 (2019), p. 970. DOI: 10.1140/epjc/s10052-019-7450-8. arXiv: 1907.05120 [hep-ex] (cit. on pp. 95, 132).

[139] ATLAS Collaboration. ATLAS flavour-tagging algorithms for the LHC Run 2 pp collision dataset. *Eur. Phys. J. C* 83.7 (2023), p. 681. DOI: 10.1140/epjc/s10052-023-11699-1. arXiv: 2211.16345 [physics.data-an] (cit. on pp. 97, 99).

[140] J. Barr, J. Birk, M. Draguet, et al. Umami: A Python toolkit for jet flavour tagging. *Journal of Open Source Software* 9.102 (2024), p. 5833. DOI: 10.21105/joss.05833 (cit. on p. 102).

[141] ATLAS Collaboration. Luminosity determination in pp collisions at $\sqrt{s} = 13$ TeV using the ATLAS detector at the LHC. *Eur. Phys. J. C* 83.10 (2023), p. 982. DOI: 10.1140/epjc/s10052-023-11747-w. arXiv: 2212.09379 [hep-ex] (cit. on pp. 117, 131).

[142] P. Baldi, K. Cranmer, T. Faucett, et al. Parameterized neural networks for high-energy physics. *Eur. Phys. J. C* 76.5 (2016), p. 235. DOI: 10.1140/epjc/s10052-016-4099-4. arXiv: 1601.07913 [hep-ex] (cit. on p. 123).

[143] F. Chollet et al. *Keras*. 2015. URL: https://keras.io (cit. on p. 123).

[144] M. Abadi et al. *TensorFlow: Large-Scale Machine Learning on Heterogeneous Systems*. 2015. URL: https://www.tensorflow.org (cit. on p. 123).

[145] A. D. Bukin. *Fitting function for asymmetric peaks*. 2007. arXiv: 0711.4449 [physics.data-an] (cit. on p. 126).

[146] B. Delaunay. Sur la sphère vide. French. *Bull. Acad. Sci. URSS* 1934 (1934), pp. 793–800 (cit. on p. 126).

[147] ATLAS Collaboration. Measurements of inclusive and differential fiducial cross-sections of $t\bar{t}$ production with additional heavy-flavour jets in proton-proton collisions at $\sqrt{s} = 13$ TeV with the ATLAS detector. *JHEP* 04 (2019), p. 046. DOI: 10.1007/JHEP04(2019)046. arXiv: 1811.12113 [hep-ex] (cit. on p. 128).

[148] ATLAS Collaboration. Study of heavy-flavor quarks produced in association with top-quark pairs at $\sqrt{s} = 7$ TeV using the ATLAS detector. *Phys. Rev. D* 89.7 (2014), p. 072012. DOI: 10.1103/PhysRevD.89.072012. arXiv: 1304.6386 [hep-ex] (cit. on p. 128).

[149] ATLAS Collaboration. Measurement of the cross-section for W boson production in association with b-jets in pp collisions at $\sqrt{s} = 7$ TeV with the ATLAS detector. *JHEP* 06 (2013), p. 084. DOI: 10.1007/JHEP06(2013)084. arXiv: 1302.2929 [hep-ex] (cit. on p. 128).

[150] ATLAS Collaboration. Eigenvector recomposition: a new method to correlate flavor-tagging systematic uncertainties across analyses (2022). URL: https://cds.cern.ch/record/2809651 (cit. on p. 132).

[151] G. Cowan, K. Cranmer, E. Gross, et al. Asymptotic formulae for likelihood-based tests of new physics. *Eur. Phys. J. C* 71 (2011). [Erratum: Eur.Phys.J.C 73, 2501 (2013)], p. 1554. DOI: 10.1140/epjc/s10052-011-1554-0. arXiv: 1007.1727 [physics.data-an] (cit. on p. 140).

[152] A. L. Read. Presentation of search results: The CL_s technique. *J. Phys. G* 28 (2002). Ed. by M. R. Whalley and L. Lyons, pp. 2693–2704. DOI: 10.1088/0954-3899/28/10/313 (cit. on p. 140).

[153] E. Gross and O. Vitells. Trial factors for the look elsewhere effect in high energy physics. *Eur. Phys. J. C* 70 (2010), pp. 525–530. DOI: 10.1140/epjc/s10052-010-1470-8. arXiv: 1005.1891 [physics.data-an] (cit. on p. 143).